



Defence Research and
Development Canada

Recherche et développement
pour la défense Canada



Design and analysis of a Yagi-like antenna element buried in LTCC material for AEHF communication systems

Michel Clénet

Defence R&D Canada – Ottawa

TECHNICAL MEMORANDUM

DRDC Ottawa TM 2005-055

April 2005

Canada

Report Documentation Page			Form Approved OMB No. 0704-0188		
Public reporting burden for the collection of information is estimated to average 1 hour per response, including the time for reviewing instructions, searching existing data sources, gathering and maintaining the data needed, and completing and reviewing the collection of information. Send comments regarding this burden estimate or any other aspect of this collection of information, including suggestions for reducing this burden, to Washington Headquarters Services, Directorate for Information Operations and Reports, 1215 Jefferson Davis Highway, Suite 1204, Arlington VA 22202-4302. Respondents should be aware that notwithstanding any other provision of law, no person shall be subject to a penalty for failing to comply with a collection of information if it does not display a currently valid OMB control number.					
1. REPORT DATE APR 2005		2. REPORT TYPE		3. DATES COVERED -	
4. TITLE AND SUBTITLE DESIGN AND ANALYSIS OF A YAGI-LIKE ANTENNA ELEMENT BURIED IN LTCC MATERIAL FOR AEHF COMMUNICATION SYSTEMS (U)			5a. CONTRACT NUMBER		
			5b. GRANT NUMBER		
			5c. PROGRAM ELEMENT NUMBER		
6. AUTHOR(S)			5d. PROJECT NUMBER		
			5e. TASK NUMBER		
			5f. WORK UNIT NUMBER		
7. PERFORMING ORGANIZATION NAME(S) AND ADDRESS(ES) Defence R&D Canada -Ottawa,3701 Carling Ave,Ottawa Ontario,CA,K1A 0Z4			8. PERFORMING ORGANIZATION REPORT NUMBER		
9. SPONSORING/MONITORING AGENCY NAME(S) AND ADDRESS(ES)			10. SPONSOR/MONITOR'S ACRONYM(S)		
			11. SPONSOR/MONITOR'S REPORT NUMBER(S)		
12. DISTRIBUTION/AVAILABILITY STATEMENT Approved for public release; distribution unlimited					
13. SUPPLEMENTARY NOTES The original document contains color images.					
14. ABSTRACT This document presents the investigation of an end-fire antenna implemented in a laminated material named LTCC (Low Temperature Co-fired Ceramic). This study is related to the development of a phased array for the AEHF Military Satellite Communication Systems. This work includes the design, the analysis, fabrication and the measurement of antenna prototypes at 44.5 GHz. The radiating element consists of a Yagi-like antenna fed by a microstrip transmission line and buried into the dielectric material. Relatively good agreement between simulated results and measurement is obtained. The results shows that this radiating element could be used for AEHF Communication systems. The next step is to study its electromagnetic behaviour in an array configuration. As the LTCC material has not previously been characterized up to 45 GHz, a study to extract the electrical properties of the LTCC material has been carried out, and is also reported in this document.					
15. SUBJECT TERMS					
16. SECURITY CLASSIFICATION OF:			17. LIMITATION OF ABSTRACT	18. NUMBER OF PAGES 104	19a. NAME OF RESPONSIBLE PERSON
a. REPORT unclassified	b. ABSTRACT unclassified	c. THIS PAGE unclassified			

Design and analysis of a Yagi-like antenna element buried in LTCC material for AEHF communication systems

Michel Clénet

Defence R&D Canada – Ottawa

Technical Memorandum

DRDC Ottawa TM 2005-055

April 2005

© Her Majesty the Queen as represented by the Minister of National Defence, 2005

© Sa majesté la reine, représentée par le ministre de la Défense nationale, 2005

Abstract

This document presents the investigation of an end-fire antenna implemented in a laminated LTCC (Low Temperature Co-fired Ceramic) material. The antenna could be employed in a brick architecture phased array for use in an Advanced Extremely High Frequency (AEHF) Military Satellite Communication terminal. The work includes the design, analysis, fabrication and measurement of antenna prototypes at 44.5 GHz. The radiating element consists of a Yagi-like antenna fed by a microstrip transmission line and buried into the dielectric material. Relatively good agreement between simulated results and measurement were obtained. The results show that this radiating element could be used in an AEHF Communication terminal. Future work will involve the study of its electromagnetic behaviour in an array configuration. As the LTCC material has not previously been characterized up to 45 GHz, a study to extract the electrical properties of the LTCC material was also carried out and is reported in this document.

Résumé

Ce document présente l'étude d'une antenne à rayonnement longitudinal implantée dans un matériau laminé appelé LTCC (Low Temperature Co-fired Ceramic). Cette étude est reliée au développement d'un réseau à déphasage pour les systèmes de communications militaires par satellites. Ce travail inclut l'étude, l'analyse, la fabrication et la mesure de prototypes réalisés à 44.5 GHz. L'antenne élémentaire consiste en une antenne de type Yagi alimentée par une ligne microruban, et noyée dans le matériau diélectrique. Une bonne corrélation est obtenue entre les résultats provenant de simulations et les mesures. Les résultats montrent que cet élément rayonnant pourrait être utilisé pour des systèmes de communication en bande EHF. La prochaine étape est l'étude du comportement électromagnétique de cette antenne dans une configuration en réseau. Comme le matériau LTCC n'a précédemment pas été caractérisé jusqu'à 45 GHz, une étude a été menée pour extraire les propriétés électriques du matériau LTCC. Ce travail est également reporté dans ce document.

This page intentionally left blank

Executive summary

The requirement for greater bandwidth in military satellite communication systems has resulted in the development of communications systems operating in the Extremely High Frequency (EHF) band. To satisfy the Canadian Forces requirement for greater bandwidth, the Department of National Defence has approved the procurement of a communication capability at EHF under the Protected Military Satellite Communications (PMSC) Project. This capability will be developed in collaboration with the United States Department of Defense under the Advanced Extremely High Frequency (AEHF) Military Satellite Communication system. The end goal is to provide the Canadian Forces with a robust, secure, worldwide military satellite communications capability.

The project reported in this document concerns the study, design and fabrication of a radiating element operating in the upper bandwidth of the AEHF frequency spectrum suitable for use in a phased array terminal antenna. The antenna is designed to be integrated in an array having a brick architecture. With the motivation of realising low cost phased array modules and to reduce the interconnection complexity in RF front end systems, a laminated packaging technology is considered. This technology, the low temperature co-fired ceramic (LTCC), enables packaging of passive and active RF components within a low loss dielectric material in a multi-layer topology.

The LTCC technology has been used extensively for several years to fabricate RF circuits, active or passive, for systems operating mostly below 10 GHz. This technology is still under development for systems working at higher frequencies. Particularly, as only a few documents report the dispersive material characteristic for frequencies up to 40 GHz and none for higher frequencies, an aspect of this project was to design and fabricate circuits to extract the material characteristics at our operating frequency of 44.5 GHz. A large part of this document concerns the design, measurement and analysis of circuits for the extraction of material properties. The characteristics of the LTCC material extracted using resonant and non-resonant circuits are similar to the results found in the literature, and this work extends the knowledge of its dispersive characteristics up to 45 GHz.

The radiating element investigated for AEHF communication systems consists of a Yagi-like antenna fed by a microstrip transmission line. The antenna is buried into the dielectric material, which acts as a protective radome. Due to the high operating frequency (44.5 GHz) the radiating element is physically small, on the order of a few millimeters. Constraints inherent to the LTCC fabrication process must be carefully taken into account in the design stage. Some prototypes were realized on several wafers at 44.5 GHz and the measurements were analysed thoroughly. The measurements show that the predicted impedance bandwidth is achieved. They also indicate the limitation of this technology, especially as the dimensions of the various circuits approach the fabrication tolerances. Future work will involve the study of the behaviour of this radiating element in an array configuration in order to realize a compact and low-cost phased array with a brick architecture in LTCC technology.

Clénet, M. 2005; Design and analysis of a Yagi-like antenna element buried in LTCC material for AEHF communication systems; DRDC Ottawa TM 2005-055; Defence R&D Canada – Ottawa.

Sommaire

La demande d'élargissement de la bande passante pour les communications militaires par satellite a engendré l'étude de systèmes de communications opérant en bande EHF. Le ministère de la défense nationale a donc initié le développement d'une technologie canadienne unique dans le cadre d'un projet de réalisation de systèmes de communications militaires canadiennes par satellite. Ce projet canadien est une partie intégrante du projet « AEHF SatCom », un projet américain de communications militaires par satellite en bande EHF.

Ce document décrit l'étude, la conception et la fabrication d'un élément rayonnant fonctionnant dans la bande fréquentielle supérieure du spectre AEHF. L'antenne est conçue pour être intégrée à un réseau d'architecture de type brique. Dans le but de réaliser des modules de réseaux à déphasage à faible coût et de réduire la complexité d'interconnexions dans les systèmes RF, une technologie d'encapsulation par stratification est considérée. Cette technologie, appelée LTCC (Low Temperature Co-fired Ceramic), permet l'encapsulation de composants RF actifs et passifs dans un matériau diélectrique à faibles pertes au moyen d'une topologie multicouche.

La technologie LTCC est utilisée intensivement depuis plusieurs années pour la fabrication de circuits RF, passifs ou actifs, pour des systèmes fonctionnant à des fréquences inférieures à 10 GHz. Elle est toujours en développement pour des systèmes fonctionnant à des fréquences plus élevées. Plus précisément, peu de documents reportent les caractéristiques dispersives de ce matériau jusqu'à 40 GHz, et aucuns à des fréquences supérieures. Un aspect important de ce projet était donc de concevoir et fabriquer des circuits afin d'extraire les caractéristiques du matériau LTCC à la fréquence de fonctionnement de 44.5 GHz. Les caractéristiques du matériau LTCC déterminées à partir de la mesure de circuits résonants et non résonants sont similaires aux résultats disponibles dans la littérature. Ce travail prolonge la connaissance de ces caractéristiques dispersives jusqu'à 45 GHz.

L'élément rayonnant étudié pour des systèmes de communications en bande EHF consiste en une antenne de type Yagi alimentée par une ligne microruban. L'antenne est noyée dans le matériau diélectrique agissant comme radôme protecteur. A cause de la fréquence d'utilisation élevée, l'élément rayonnant est physiquement petit, de l'ordre de quelques millimètres. Les contraintes imposées par le processus de fabrication LTCC doivent être soigneusement prises en compte dans la phase de conception. Quelques prototypes ont été réalisés à 44.5 GHz sur plusieurs plaquettes et l'analyse des mesures montre que la bande passante escomptée est obtenue. Elle met également en évidence les limites de cette technologie quand les dimensions des divers circuits flirtent avec les tolérances de fabrication. La prochaine étape est l'étude de cet élément rayonnant dans une configuration en réseau afin de réaliser un réseau à déphasage d'architecture de type brique à faible coût en technologie LTCC.

Clénet, M. 2005; Design and analysis of a Yagi-like antenna element buried in LTCC material for AEHF communication systems; DRDC Ottawa TR 2005-055; R & D pour la défense Canada – Ottawa.

Table of contents

Abstract	i
Résumé	i
Executive summary	iii
Sommaire.....	iv
Table of contents	v
List of figures	vii
List of tables	x
1. Introduction	1
1.1 Goal	1
1.2 LTCC technology	1
1.2.1 Description	1
1.2.2 Constraints due to the LTCC Process.....	4
1.3 Antenna considerations	5
2. Design of the Antenna and its Feeding System.....	7
2.1 The microstrip lines.....	8
2.2 The power divider	9
2.3 The 180° delay line.....	9
2.4 The coplanar striplines	10
2.5 The radiating element.....	11
2.6 Final design of the antenna with its feeding system.....	12
2.6.1 The input impedance response	13
2.6.2 The radiation pattern characteristics.....	16
3. Design of Microwave Circuits for Extraction of Material Parameters.....	20
3.1 Design of an embedded ring resonator.....	20
3.1.1 Theoretical background.....	20
3.1.2 Design of the ring resonator	23
3.2 Extraction of the material characteristics using a transmission line loaded with an open stub.....	24
4. Design of the Calibration Lines for TRL Measurement.....	28

5.	Layout of the Circuits for Fabrication	29
6.	Measurement and Analysis.....	31
6.1	Dimensions measurements	32
6.2	Extraction of the material properties	35
6.2.1	Measurement of the ring resonator	35
6.2.2	Measurement of the transmission line loaded with an open stub ("T-junction")	39
6.2.3	Extraction of the attenuation factor using transmission line measurement.....	40
6.2.4	Conclusions	45
6.3	Input impedance of the Yagi-like antennas.....	45
7.	Summary	50
8.	References	51
	Appendices	54
	Appendix 1. LTCC technology	55
	Appendix 2. Parametric study of the Yagi-like antenna	56
	Appendix 3. Calculation of the scattering matrix coefficients of a microstrip transmission line loaded with an open stub	58
	Appendix 4. Drawings of the different circuits.....	61
	Appendix 5. Pictures of the launcher	64
	Appendix 6. List of the measurement files	65
	Appendix 7. Graphs of the S_{12} response of the two-ports circuits realized on the three different wafers.....	68
	Appendix 8. Loss characterisation using transmission line measurement.....	75
	Appendix 9. Input impedance of the Yagi-like antennas.....	77
	List of symbols/abbreviations/acronyms/initialisms	84
	Glossary	85

List of figures

Figure 1. Examples of LTCC realisations	2
Figure 2. LTCC fabrication process	3
Figure 3. LTCC design capabilities	3
Figure 4. Parameters affected by the LTCC process	4
Figure 5. Overview of the Yagi-like antenna	6
Figure 6. Yagi-like antenna with its feeding system	7
Figure 7. Characteristic impedance of a microstrip line as a function of the line width with superstrate of different thickness	8
Figure 8. a) Quarter-wavelength transformer and b) power divider	9
Figure 9. 180° delay lines realized with a) two lines having four 90° bends, and b) one line having four 90° bends and one line containing four 45° bends	10
Figure 10. Design of the balanced (a) and unbalanced (b) back-to-back microstrip-to-CPS transitions	11
Figure 11. Frequency responses of the balanced and unbalanced back-to-back microstrip- to-CPS transitions	11
Figure 12. Geometry of the Yagi-like antenna with its feeding system	13
Figure 13. Input impedance of the Yagi-like antenna on infinite substrate	14
Figure 14. Reflection coefficient of the Yagi-like antenna on infinite substrate	14
Figure 15. Input impedance of the Yagi-like antenna on an 8 mm wide substrate	15
Figure 16. Reflection coefficient of the Yagi-like antenna on an 8 mm wide substrate	15
Figure 17. Yagi-like antenna in its coordinate system	16
Figure 18. Radiation pattern in the $\phi=0^\circ$ plane (H-plane)	17
Figure 19. Radiation pattern in the $\phi=90^\circ$ plane (E-plane)	17
Figure 20. Radiation pattern in the $\phi=0^\circ$ plane (H-plane) for different frequencies	18
Figure 21. Radiation pattern in the $\phi=90^\circ$ plane (E-plane) for different frequencies	18
Figure 22. Gain and efficiency of the Yagi-like antenna	19
Figure 23. Cross-polarisation level in the broadside direction and front-to-back ratio of the Yagi-like antenna	19
Figure 24. Ring resonator	20
Figure 25. Transmission factor of the ring resonator circuit	24
Figure 26. Microstrip transmission line loaded with an open stub	24

Figure 27. S-parameters of the 3λ transmission line loaded with an $3\lambda/4$ open stub	27
Figure 28. Cavity for probe circuit access	29
Figure 29. Layout of the complete LTCC run	30
Figure 30. Picture of a) the four different Yagi-like antennas, circuit #2, and b) the launcher part of the Yagi-like antenna #1 circuit #2 (October 2003).....	31
Figure 31. Transmission factor of the ring resonator	35
Figure 32. Possible conductor configurations in a multi-layer LTCC substrate.....	36
Figure 33. Relative permittivity deduced from various measurements	38
Figure 34. Comparison of various attenuation factor measurements	39
Figure 35. Measured and simulated S-parameters of transmission lines of various lengths	42
Figure 36. Attenuation factor obtained from transmission factor measurement	43
Figure 37. Attenuation factor obtained with the absolute magnitude method.....	44
Figure 38. Attenuation factor obtained with the line comparison method	45
Figure 39. Input impedance of antenna #1 measured on all wafers with different TRL calibrations	47
Figure 40. Measured input impedance of all antennas on Wafer #1	48
Figure 41. Simulated input impedance of the Yagi-like antennas	49
Figure 42. Input impedance response of the Yagi-like antenna as a function of the distance between the director and the substrate's edge	56
Figure 43. Input impedance of the Yagi-like antenna on substrates of different dimensions ..	57
Figure 44. Representation of a microstrip transmission line loaded with an open stub	58
Figure 45. Drawing of the Yagi-like antenna	61
Figure 46. Drawing of the calibration lines and the open stub resonator	62
Figure 47. Layout of the ring resonator	63
Figure 48. Picture of the microstrip line (October 2003)	64
Figure 49. Picture of a via pad connected to the ground (October 2003).....	64
Figure 50. Transmission Factor of the Ring Resonator Circuits	70
Figure 51. S-parameters of the three wavelength microstrip line loaded with a three-quarter of wavelength open stub	73
Figure 52. Attenuation factor estimated using the absolute magnitude method, in dB/cm and dB/inch.....	75
Figure 53. Attenuation factor estimated using the line comparison method, in dB/cm and dB/inch	76
Figure 54. Input impedance of antenna #2 on all wafers measured with different TRL calibrations	79

Figure 55. Input impedance of antenna #3 measured on all wafers with different TRL calibrations	80
Figure 56. Input impedance of antenna #4 on all wafers measured with different TRL calibrations	81
Figure 57. Input impedance of all antennas measured on wafer #2 in October 2003.....	82
Figure 58. Input impedance of all antennas measured on wafer #3 in January 2004	83

List of tables

Table 1. Resonant frequencies and transmission factors of the ring resonator circuit	23
Table 2. Summary of the characteristics of a 3λ microstrip line loaded with a $3\lambda/4$ open stub	26
Table 3. Dimensions of the launchers of the ring resonator and three-lambda microstrip line loaded with an open stub circuits.....	33
Table 4. Dimensions of the Yagi-like launchers on wafer #2 (and wafer #3).....	34
Table 5. Averaged results of the ring resonator measurements performed with TRL calibrations	37
Table 6. Results from simulation of the ring resonator (ring_res_embedded_20dB file)	37
Table 7. Averaged results of the “T-junction” measurements realized with TRL calibrations	40
Table 8. LTCC manufacturers and processes	55
Table 9. LTCC Process characteristics.....	55
Table 10. Measurement of the ring resonator on wafer # 1 with TRL calibration (October 2003)	71
Table 11. Measurement of the ring resonator on wafer # 2 with TRL calibration (January 2004).....	71
Table 12. Measurement of the ring resonator on wafer # 3 with TRL calibration (January 2004).....	71
Table 13. Measurement of the “T-junction” circuit on wafer #1 (October 2003)	74
Table 14. Measurement of the “T-junction” circuit on wafer #2 (January 2004).....	74
Table 15. Measurement of the “T-junction” circuit on wafer #1 (October 2003)	74
Table 16. Characteristics of antenna #1 obtained from measurement and simulation	77
Table 17. Characteristics of antenna #2 obtained from measurement and simulation	77
Table 18. Characteristics of antenna #3 obtained from measurement and simulation	78
Table 19. Characteristics of antenna #4 obtained from measurement and simulation	78

1. Introduction

1.1 Goal

The goal of this project is to develop a radiating element suitable for use in a phased array antenna having a brick architecture [1]. End-fire radiating elements are required for this kind of architecture. The application of the antenna is for an Advanced EHF (AEHF) satellite communications terminal operating at 44.5 GHz.

Low temperature co-fired ceramic (LTCC) was selected as the packaging technology. This technology is mostly used in industry for low frequency applications, but is being investigated for packaging high-frequency components like the elements of the phased array antenna discussed in this report. This technology is summarized in the next section.

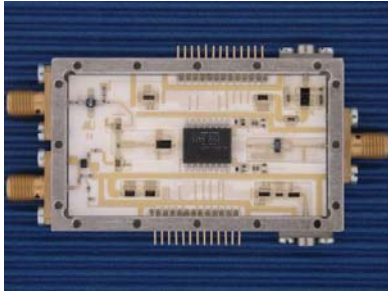
A survey of the literature on LTCC reveals that most realisations are in frequency bands lower than 30 GHz. This document will provide insight into the complexity of using LTCC packaging at higher frequencies. Indeed, at this frequency some dimensions are on the order of the fabrication tolerances of this specific process.

1.2 LTCC technology

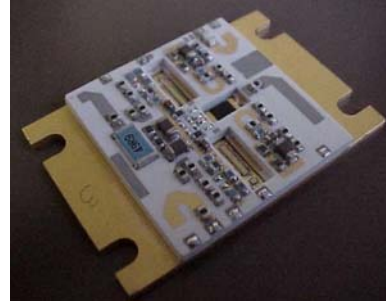
LTCC is a multi-layer material used for subsystem packaging. It offers many advantages for high-density integration of RF to millimetre-wave integrated circuits [2]. It is therefore an attractive technology for packaging phased array modules, where the size at millimetre-wave frequencies is an important issue [3]. The circuits implemented with other processes, such as GaAs MMICs (monolithic microwave integrated circuits), are assembled in a multi-layer configuration using printed lines, vias and even ball grid arrays (BGA). Figure 1 shows some examples of devices realized in LTCC technology.

1.2.1 Description

This process uses a low temperature firing temperature, usually below 1000 °C, typically 850 °C. This is a great advantage compared to other processes, because low loss conductors such as silver and gold can be used as their melting temperatures are above the LTCC firing temperature. Some LTCC materials are also low loss, even at high frequency. DuPont, for instance, offers an LTCC tape with 0.002 loss tangent at 40 GHz. Ferro also proposes a low loss material. The Ferro A6 material has a dielectric constant of 5.7 and loss tangent of 0.0012.



Point-to-multipoint transceiver for 24.5 to 26.5 GHz (Source: IMST, Germany)



LTCC RF power amplifier module for base station applications

Source: "RF and Microwave Components in LTCC", L. Devlin, G. Pearson, J. Pittock - Plextek Ltd., B. Hunt - CMAC Micro Technology, April, 2001



Source: <http://www.dilabs.com/Dipak/benefits/1dipak.htm>

Figure 1. Examples of LTCC realisations

The LTCC process is shown in Figure 2. Starting from a rolled dielectric tape, the layers are first cut and dried. The layers are then perforated where connections between transmission lines on different layers are needed. The cylindrical holes are filled with metal to ensure reliable contacts. The next step is to print the conductors on each separate layer. Then comes the collating step, followed by lamination using controlled pressure. Finally, the assembled circuit is fired at a peak temperature of 850 °C. The post-processing operation consists of integrating the various components by direct soldering, using wire bonding or BGA as shown in Figure 3.

This process must be quite precise in order to realize circuits with predictable characteristics. For instance, the lamination must be performed with a specific pressure for a precise duration. The firing step is also strictly controlled in temperature and time. This phase is very important, as the LTCC material is shrinking during this stage, and the percentage of shrinkage depends on this process. Detailed information can be obtained from the material providers [4]-[8].

The LTCC material we are considering is provided by DuPont [4]. DuPont proposes several LTCC green tapes. One of them is especially suitable for RF applications, the Dupont 943 tape. This tape has a 107 μm fired thickness. Its dielectric permittivity is 7.1 and its loss tangent is 0.002.

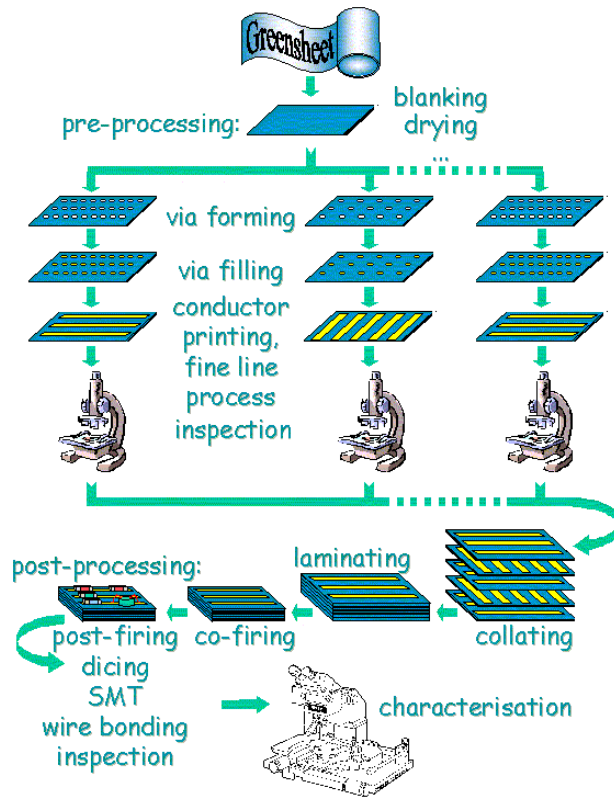


Figure 2. LTCC fabrication process

(source of the drawing: www.ltcc.de/what-is-ltcc/ltcc-process/ltcc-process.htm)

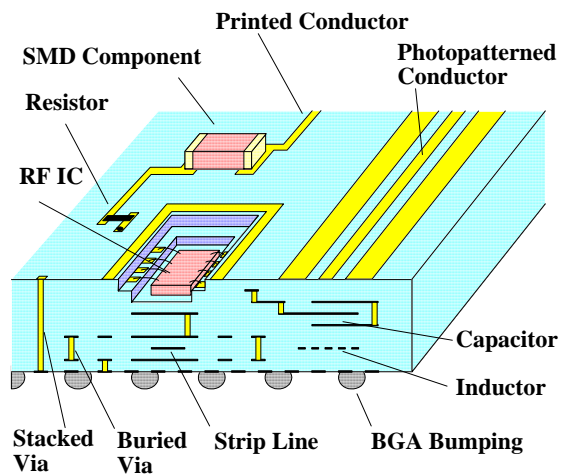


Figure 3. LTCC design capabilities

(source of the drawing: VTT Electronics)

1.2.2 Constraints due to the LTCC Process

As mentioned previously, the LTCC fabrication process must carefully follow a number of steps to achieve the desired result. Only a few companies in the world have the tools, knowledge and skills to fabricate circuits using this technology. The most important ones are listed in Appendix 1. Also, LTCC fabrication imposes constraints on the design. The constraints depend on the LTCC material itself, and also on the tools used for fabrication. The main constraints for various LTCC materials and manufacturers are also listed in Appendix 1. In this section, we will focus on the constraints imposed by the LTCC process used by the manufacturer for this project, VTT Electronics, Finland (VTT is a Finnish acronym standing for Valtion Teknillinen Tutkimuskeskus). These constraints also affect our design. Their complete design guidelines are available online [9]. Figure 4 summarizes the main parameters affected by these guidelines or constraints.

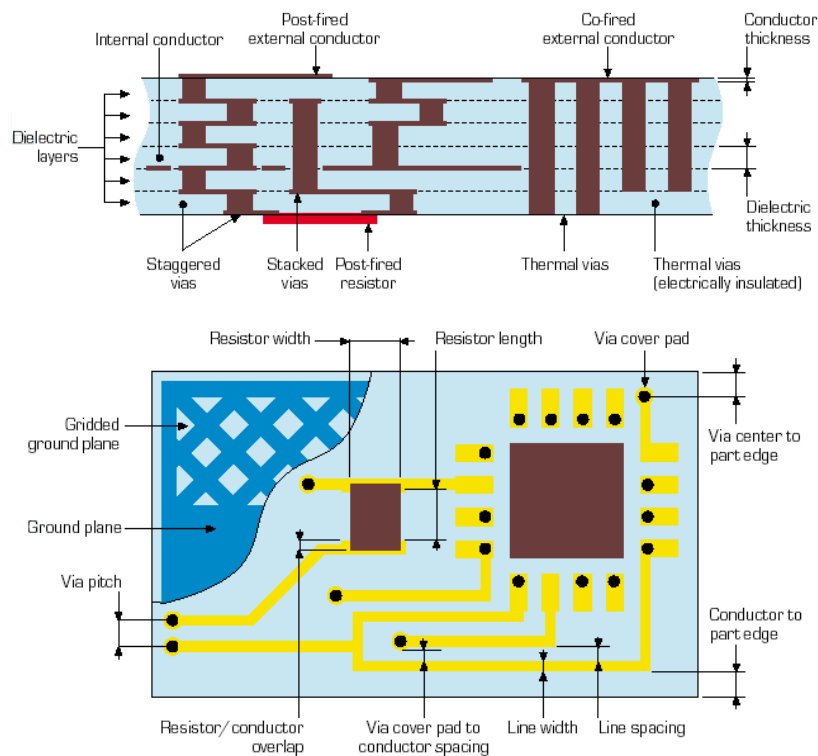


Figure 4. Parameters affected by the LTCC process
(source of the drawing: Thales Microsonics)

The first constraint is that the thickness of the LTCC sheet is fixed at 107 μm after co-firing. A minimum of five layers is required to produce a rigid substrate, and the part size can be up to 114x114 mm^2 (4.5"x4.5"). The minimum line width is 100 μm , as well as the minimum line spacing. This constraint is a critical issue as the width of a 50 Ω microstrip line embedded in the material is 99 μm . The maximum line width is 1.5 mm with unlimited length. The use

of 90°-bend lines is recommended for optimum line width control, but 45°-bend lines are allowed. The printed lines must be at least 380 µm away from the substrate edge.

Buried large metallic planes, such as ground plane, can not be realized. With large metallic planes, the dielectric sheets on both side are not in contact, and there is a risk of de-lamination of the substrate. Therefore, gridded metallic planes are used instead of solid ones. The grid pattern must cover less than 50% of the area with metallisation. As mentioned in the guideline, the preferred plane uses 250 µm lines and 550 µm spaces. Note that solid conductor areas in the gridded plane can be used locally to improve RF performance.

Cavities in the substrate can be realized, but their geometrical characteristics must also follows guidelines. First, the cavity floor must have a minimum fired thickness of 380 µm. This corresponds to a minimum of four layers. The cavity walls must be at least 3.0mm apart. Any printed line in the cavity must be at least 200 µm from the cavity walls. The printed lines outside of the cavity must be at least 250 µm away from the cavity walls. Also, any vias (metallized holes) must be at a distance of 2.5 times their diameter from the cavity wall.

Guidelines for vias also exist. Vias can go through only one layer at a time. Stacking vias can be done, but results in a bump on the surface. To avoid this, staggering of vias is recommended. Vias should then be staggered for connection between metallizations separated by several layers. The minimum via diameter is 150 µm. The minimum distance between vias on a single layer is 2.5 times the via diameter, and the minimum distance between two consecutive staggered vias is twice the via diameter. The vias must be at least three times their diameter away from the substrate edge. Constraints also exist on the catch pads, which are the metallisation at the extremities of the vias. The catch pads must be at least 50 µm larger than the via diameter.

The rules described here must be followed in the design procedure to avoid any problem during the fabrication phase.

1.3 Antenna considerations

There are basically two kinds of antenna array architectures, the brick architecture and the tile architecture. As described in [1], the tile architecture is a multi-layer assembly of the different components of the phased array. The radiating elements, usually printed antennas, are on the top layer. The amplifiers are on a layer below the radiating elements, the phase shifters on the next lower layer, and then finally other components as required. With the brick architecture, the array is divided into modules realized on separated boards. Each module contains the radiating element (end-fire type), the amplifier, the phase shifter, the filter, and other components. All modules are juxtaposed to form the complete phased array.

Each array architecture type requires different types of radiating elements. The printed antennas, like patch antennas (which have a direction of radiation normal to their geometry) are suitable for arrays with a tile architecture. The end-fire antennas, whose radiation direction is the prolongation of the antenna structure, are preferred for arrays of brick architecture. Different kinds of end-fire antennas exist, and were considered for this project. Aperture antennas, such as horn and open-ended waveguide antennas, are one example. They can also be implemented using laminated technology, like LTCC [10]. The tapered slot antennas [11] are antennas widely used in phased arrays for radar applications as they exhibit large

impedance bandwidth. Printed dipoles are also other candidates as radiating elements for brick architecture arrays. However, dipole antennas have both forward and backward radiations, which is undesirable for this application. The Yagi-Uda antenna is another antenna that can be used for this array [12]. Basically, The Yagi-Uda antenna is a linear array of dipoles. A dipole placed behind the driven dipole acts as a reflector whereas additional dipoles placed in front serve as directors. Recently, a quasi-Yagi antenna, or Yagi-like antenna, has been developed in printed technology [13], and has shown potential for array applications[14]. The reflector of the quasi-Yagi antenna, shown in Figure 5, is realized by the ground plane of the feeding circuit. The radiating element has only one director, and thus exhibits a wide beamwidth in the main planes.

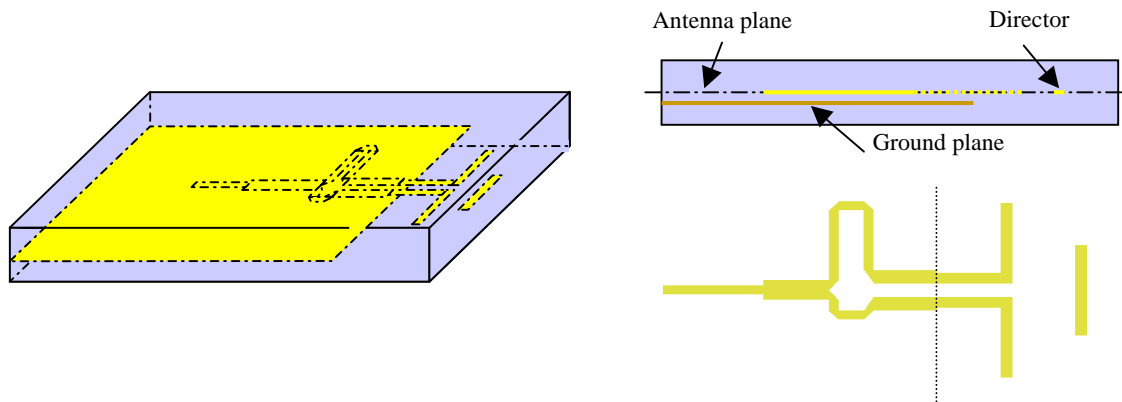


Figure 5. Overview of the Yagi-like antenna

The quasi-Yagi antenna is selected as the radiating element as it possesses the required characteristics for our application in the AEHF band. However, this antenna requires further investigation for our application. Indeed, contrary to previous published works, the antenna will be built flush into the material and not printed at the air-substrate interface. This will affect its characteristics, like the impedance bandwidth, as the near field will be mostly confined in the thick dielectric substrate.

2. Design of the Antenna and its Feeding System

The antenna design has been carried out using two different commercial software packages: a simulation tool based on the method of moments, Zeland IE3D [15], and a software package based on finite element methods, Ansoft HFSS [16]. IE3D software was first used for optimizing the different parts of the radiating element independently. HFSS was used for providing the electromagnetic characteristics of the overall structure. This two-step approach was adopted to reduce the computation time. Using Zeland IE3D, the optimization of the elements can be done faster than with Ansoft HFSS. But firstly, line dimensions (length, width) were estimated using conventional analytical expressions that can be found in [17].

The radiating element we consider is shown in Figure 6. It consists of a Yagi-like antenna fed by a microstrip line [13]. A microstrip to coplanar stripline (CPS) transition was designed to provide the necessary balanced feed. The circuit is buried in the material. The microstrip components are realized on a one-layer thick substrate over a truncated ground plane. Three layers are covering the circuit. The dipole and its director are embedded in the middle of the material, with three ceramic layers below and above.

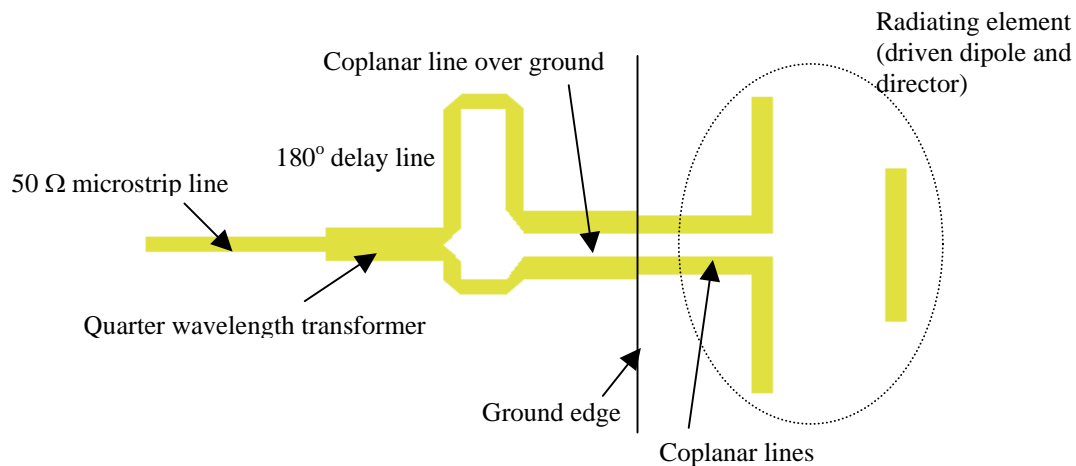


Figure 6. Yagi-like antenna with its feeding system

The microstrip line, the quarter-wavelength transformer, the 180° delay line, the CPS lines and the radiating element have been optimized independently. The coplanar strips, with or without ground plane, were designed under the constraint of a 150 μm spacing. The ground plane is completely metallized, and not gridded as required by the design guideline, to reduce the complexity of the problem and the computation time. The optimization process for each component is described in the remainder of this section.

2.1 The microstrip lines

The LTCC process dictates that the distance between the microstrip and the ground must be a multiple of the layer thickness. A spacing of one layer has been chosen, to avoid the excitation of a non-negligible amount of power into the surface wave mode [17]. When covered with a dielectric superstrate the impedance characteristic of the microstrip line changes as the near-field distribution is modified. In the present case, the microstrip line is printed on an LTCC DuPont 943 substrate, 107 μm over the ground plane. Figure 7 shows the variation of the characteristic impedance of a microstrip line with the superstrate thickness as a parameter. These curves are from analytical equations obtained with conformal transformations [18], [17]. They do not take into account frequency dispersion. Note that the impedance variation due to the superstrate thickness becomes negligible above a 2-layer thickness.

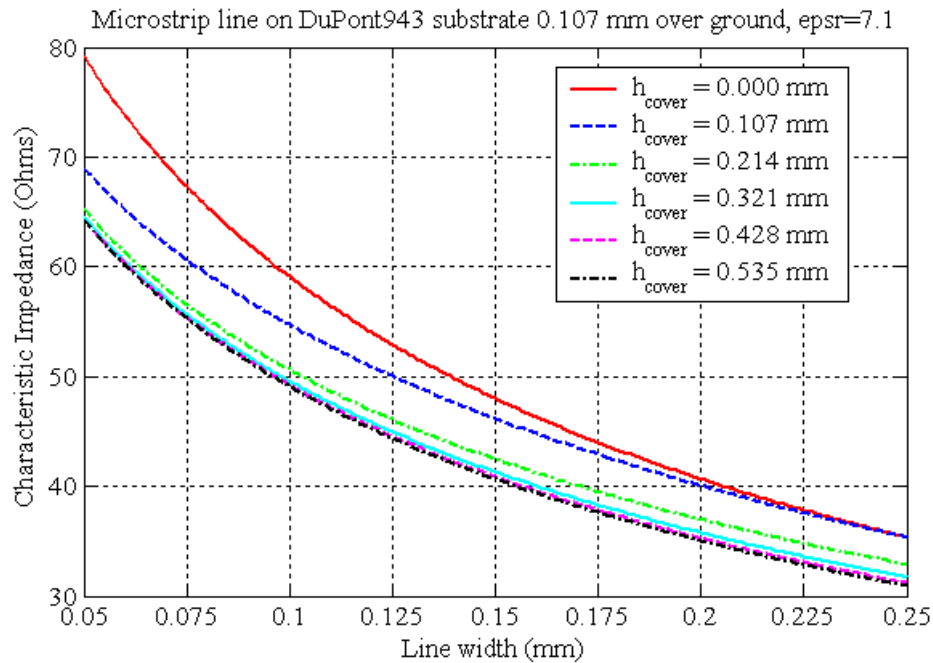


Figure 7. Characteristic impedance of a microstrip line as a function of the line width with superstrate of different thickness

As an example, the line width for a 50 Ω characteristic impedance when the microstrip line is not covered by any superstrate is 136 μm . When covered by a 321 μm superstrate, the line width drops to 98 μm , and to 96.5 μm with 428 μm superstrate. In the second case, the line width is slightly less than the minimum possible line width given by the manufacturer. More accurate values have been calculated using a full wave simulation software package, IE3D. Similar results have been found; a 50 Ω characteristic impedance is obtained with a microstrip line width of 128 μm with no cover, and of 99 μm when covered with a 321 μm superstrate.

2.2 The power divider

The power divider is one of the components of the microstrip to CPS transition needed to feed the Yagi-like antenna (Figure 6). It must equally divide the power transmitted from one $50\ \Omega$ microstrip line to two $50\ \Omega$ microstrip lines. A quarter-wavelength transformer is then used to match the impedance. The quarter-wavelength transformer usually exhibits narrow band behaviour [19], but it is sufficient for the present application. A $35.35\ \Omega$ line impedance is necessary to accomplish this operation. An optimization process using Zeland IE3D software package leads to a microstrip line 0.64 mm long and 0.2 mm wide to realize the 90° phase shift with a straight microstrip line with an impedance of $35.35\ \Omega$ (Figure 8a).

However, the microstrip line length requires tuning when connecting the three $50\ \Omega$ lines together through the impedance transformer. Note that the method for connecting the output ports (port 2 and 3 as shown in Figure 8b) with lines parallel or orthogonal to the input port line influences the matching. A final optimization leads to a quarter-wavelength transformer 0.648 mm in length and 0.215 mm wide to achieve the best matching.

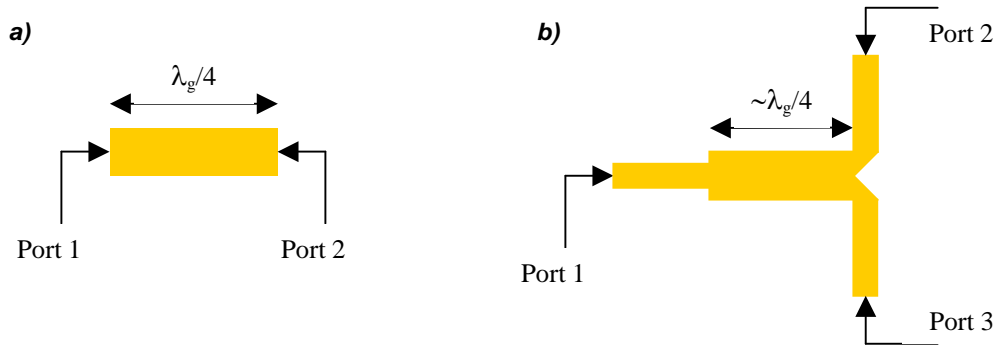


Figure 8. a) Quarter-wavelength transformer and b) power divider

2.3 The 180° delay line

A 180° phase shift has to be introduced between the two microstrip lines at the output of the power divider to realize a balanced feed for the coplanar transmission line. Note that the coplanar stripline width changes as it goes over the edge of the ground plane. The 90° bends are taken into account in the evaluation of the delay line as they affect the phase and magnitude of the propagated signal.

Two test configurations are considered. The first one, shown in Figure 9a, is used to evaluate the phase difference between two microstrip transmission lines having four 90° bends. The second configuration (Figure 9b) is used to evaluate the phase shift between a line having four 90° bends and a line containing four 45° bends. In the first configuration, the vertical line length difference is 0.598 mm . In the second configuration the difference increases to 0.6055 mm . The last design is preferred as it is more compact and the insertion loss due to the bends

of the two lines exhibits less discrepancy compared to the first design (0.17 dB difference versus 0.72 dB).

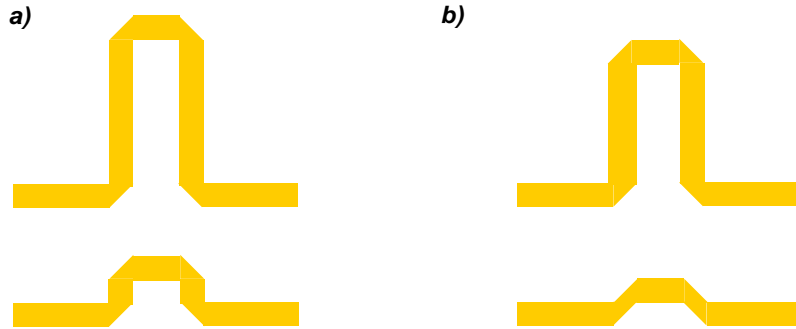


Figure 9. 180° delay lines realized with a) two lines having four 90° bends, and b) one line having four 90° bends and one line containing four 45° bends

2.4 The coplanar striplines

Design rules required for designing the CPS imposes that the separation between the two printed lines should be at least $150\ \mu\text{m}$. Under this constraint, a $50\ \Omega$ coplanar stripline would lead to a $738\ \mu\text{m}$ line width. A printed line with such a width could interfere with the other components of the antenna and its feed. Therefore, a $100\ \Omega$ impedance line is chosen for the coplanar stripline. This choice, considering a $150\ \mu\text{m}$ line spacing, leads to a $118\ \mu\text{m}$ line width. Note that a quarter guided wavelength equals $0.652\ \text{mm}$. This line length is used for the design of the antenna.

As the coplanar stripline above ground is the interface between the $100\ \Omega$ coplanar stripline and the $50\ \Omega$ microstrip lines, it must act as an impedance transformer. Then, considering a quarter-wavelength line as impedance transformer, its impedance must equal $70.7\ \Omega$ in coplanar stripline mode. Under the constraint of a $150\ \mu\text{m}$ line spacing, the optimum line width is $149\ \mu\text{m}$. A length of $0.63\ \text{mm}$ corresponds to a quarter-wavelength line.

All the components needed to realize the microstrip to coplanar stripline transition have been evaluated independently using a full-wave simulator (Zeland IE3D). The different parts have then been connected together. Following [20], balanced and unbalanced back-to-back microstrip-to-CPS transitions, shown in Figure 10, have been simulated to confirm the design. Results for both circuits are given in Figure 11. The balanced and unbalanced circuits exhibit similar responses, indicating that the 180° phase shift is correctly achieved. The insertion loss is around 1 dB. The circuits are also matched over the operating bandwidth (43.5-45.5 GHz). However, the minimum reflection coefficient is not achieved at the centre frequency. A modified version gives the desired minimum reflection coefficient at the centre frequency, as shown in Figure 11. This result is obtained by reducing the width of the coplanar stripline

from 118 μm to 116 μm and its length from 652 μm to 605 μm . The reflection coefficient is then lower than -16 dB in the operating frequency band.

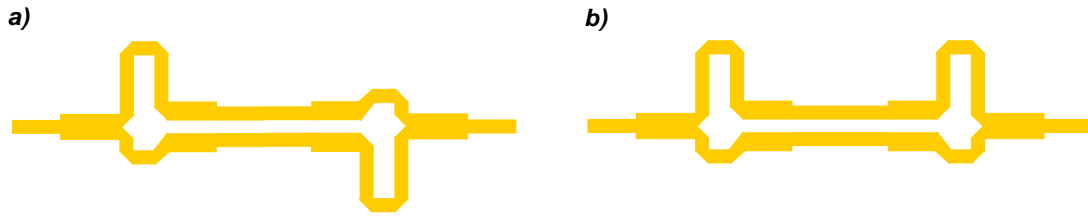


Figure 10. Design of the balanced (a) and unbalanced (b) back-to-back microstrip-to-CPS transitions

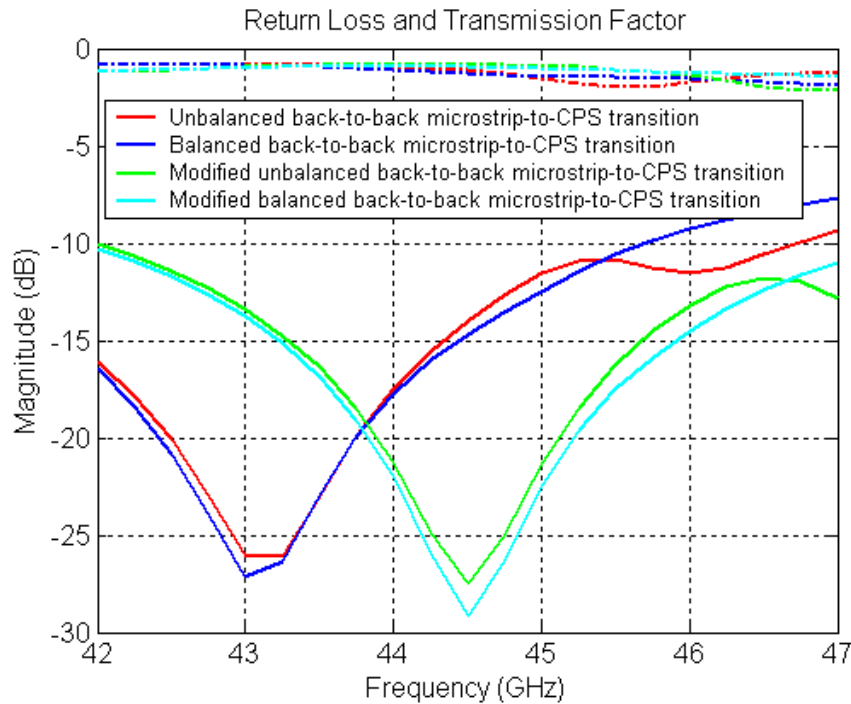


Figure 11. Frequency responses of the balanced and unbalanced back-to-back microstrip-to-CPS transitions

2.5 The radiating element

As a starting point for the design of the radiating element, standard design considerations of a Yagi-Uda antenna are followed for evaluating the dimensions of the Yagi-like antenna [21]. Specifically, the driven element length is usually between 0.45λ to 0.49λ , where λ is the

guided wavelength, and the director length is usually between 0.4λ and 0.45λ . The spacing between the driven element and the director should be 0.3λ to 0.4λ , and the spacing between the reflector and the driven element is about a quarter guided wavelength. For the design, we also consider an antenna fed with the coplanar stripline defined previously, i.e., with a line spacing of 0.15 mm and a line width of 0.116 mm.

A first optimization using IE3D has been carried out on the driven dipole by itself to achieve a good matching to 100 Ω . A dipole length of 1.922 mm (larger than half a wavelength) and a width of 0.116 mm results in a -35 dB reflection coefficient at 44.5 GHz using an input impedance normalized to 100 Ω . The reflection coefficient is below -28 dB over the operating bandwidth (43.5 GHz to 45.5 GHz). The distance between the elements of the Yagi-like antenna (the reflector, director and driven element) have been optimized automatically for obtaining a good matching, starting from the dimensions of a standard Yagi-Uda antenna. A fine tuning has been carried out manually on the antenna elements to lower cross polarisation and back radiation while maintaining a good impedance matching. Finally, the driven dipole is positioned at about a quarter wavelength from the truncated ground plane, which acts as a reflector. The distance between the director and the driven dipole is slightly smaller than the distance between the driven dipole and the reflector. The director length was initially chosen to be about 0.4 times the guided wavelength using conventional Yagi-Uda antenna design rules [21]. A fine tuning was required to preserve a good matching.

2.6 Final design of the antenna with its feeding system

The geometry of the Yagi-like antenna and its feeding system with all the geometrical parameters is shown in Figure 12. The final dimensions of the circuit are:

- $W_{\text{strip}} = 99 \mu\text{m}$,
- $W_{\text{transf}} = 215 \mu\text{m}$, $L_{\text{transf}} = 648 \mu\text{m}$,
- $L_{b1} = 771.5 \mu\text{m}$, $L_{b2} = 250 \mu\text{m}$, $L_{b3} = 655 \mu\text{m}$,
- $L_{\text{cps}_g} = 630 \mu\text{m}$, $W_{\text{cps}_g} = 149 \mu\text{m}$,
- $S_{\text{cps}} = 150 \mu\text{m}$, $L_{\text{cps}} = 630 \mu\text{m}$, $W_{\text{cps}} = 116 \mu\text{m}$,
- $L_{\text{dri}} = 1.922 \text{ mm}$, $L_{\text{dir}} = 1 \text{ mm}$, $S_{\text{dir}} = 0.62 \text{ mm}$.

These dimensions have been obtained after optimisation of the total circuit. As the microstrip to coplanar stripline transition exhibits good characteristics, only the antenna geometry and the coplanar stripline dimensions have been adjusted manually. The following sub-sections reports the characteristics of the optimum antenna in terms of input impedance response and radiation characteristics.

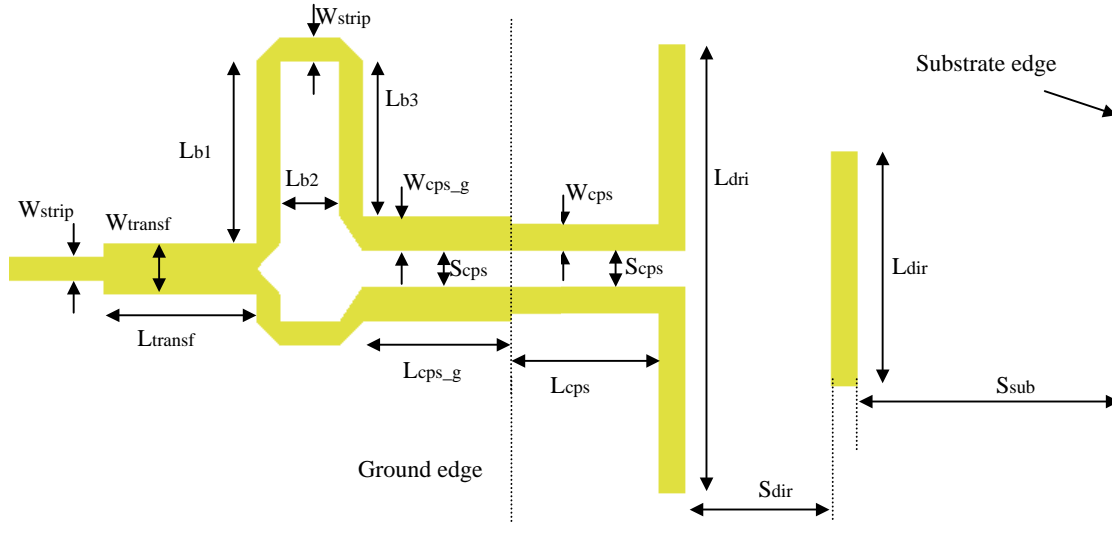


Figure 12. Geometry of the Yagi-like antenna with its feeding system

2.6.1 The input impedance response

The optimized antenna was first simulated on an infinite substrate with the two software packages, Zeland IE3D and Ansoft HFSS. The results of the input impedance on the Smith Chart and the reflection coefficient from both simulations are compared in Figure 13 and Figure 14, respectively. The circle centered on the Smith Chart represents a voltage standing wave ratio (VSWR) of 2. The results are in good agreement, even though a slight frequency shift (1.55%) occurs between the two responses. With an infinite substrate, an impedance bandwidth of 6.7% centered around $F_0 = 44.7$ GHz (43.2 GHz to 46.2 GHz) is obtained using IE3D results, while an impedance bandwidth of 7.1% centered around $F_0 = 45.3$ GHz (43.7 GHz to 46.9 GHz) is achieved using HFSS results. Note that a larger impedance bandwidth could be obtained, if the circuit was matched to centre the loop on the Smith Chart (Figure 13).

As the truncation of the substrate affects the input impedance, another optimization was required to find the best distance between the director and the edge of the substrate. Results from several simulations demonstrated that the input impedance of the Yagi-like antenna is very sensitive to this parameter. The results are given in Appendix 2. A distance of 1.4 mm was found to be optimum in terms of input impedance and impedance bandwidth. The antenna characteristics were also affected by the substrate width, which induces a frequency shift and impedance variation as the substrate edges bounce the propagated wave back to the antenna input. These results are also given in Appendix 2. This effect must be kept in mind when comparing the results from simulation and from measurements of the realized antennas.

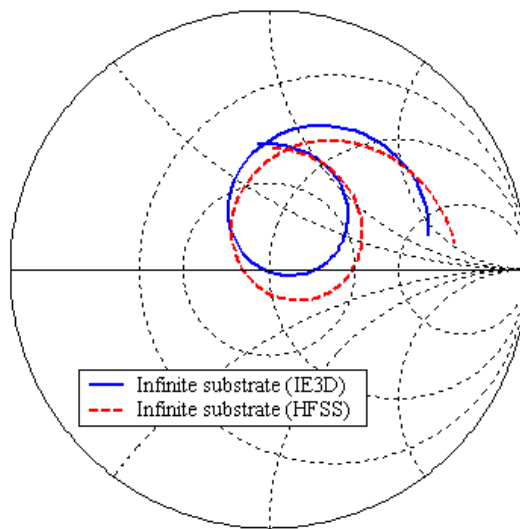


Figure 13. Input impedance of the Yagi-like antenna on infinite substrate

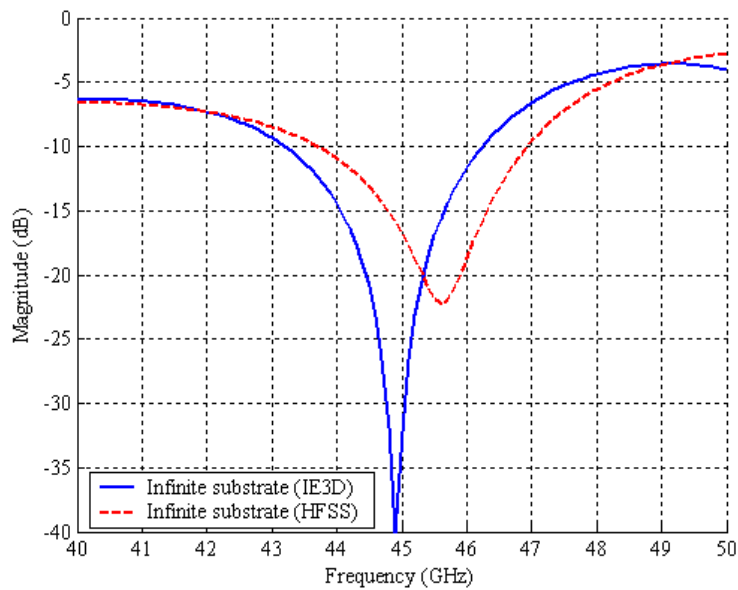


Figure 14. Reflection coefficient of the Yagi-like antenna on infinite substrate

Finally, considering an antenna with a director placed at 1.4 mm from the substrate edge ($0.21\lambda_o$, $0.56\lambda_g$), an impedance bandwidth of 18.2% centered around $F_o = 44$ GHz (40 GHz to 48 GHz) was obtained. This result is achieved with an 8 mm wide substrate ($1.2\lambda_o$, $3.2\lambda_g$)

and with substrate edges 3.04 mm away from dipole extremities ($0.45\lambda_0$, $1.2\lambda_g$). The input impedance and reflection coefficient are presented in Figure 15 and Figure 16, respectively.

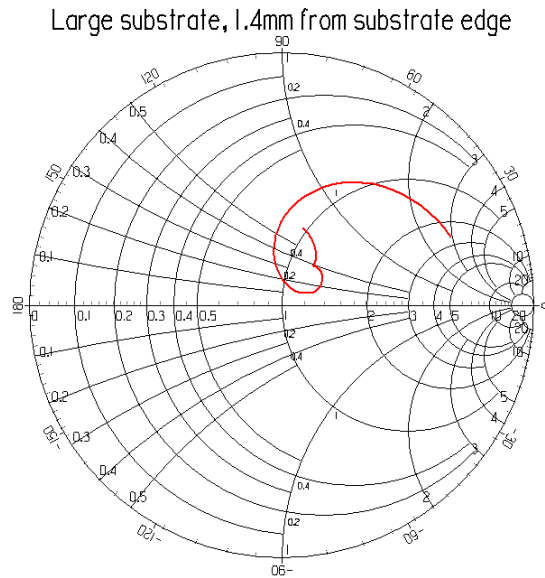


Figure 15. Input impedance of the Yagi-like antenna on an 8 mm wide substrate

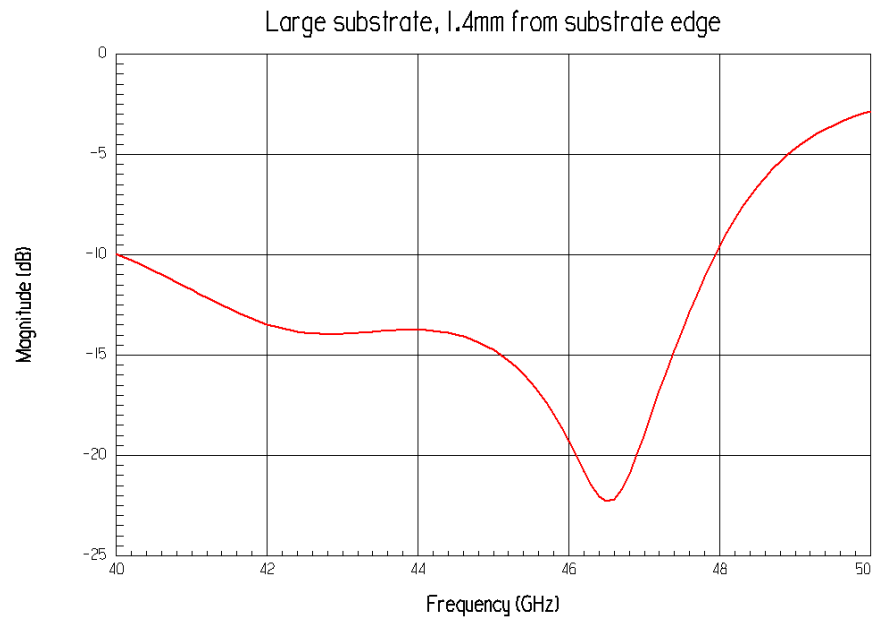


Figure 16. Reflection coefficient of the Yagi-like antenna on an 8 mm wide substrate

2.6.2 The radiation pattern characteristics

The radiation patterns of the optimum circuit are shown in the two main planes for the centre frequency of 44.5 GHz in the $\varphi=0^\circ$ and $\varphi=90^\circ$ planes in Figure 18 and Figure 19, respectively. The larger dashed circle corresponds to the -3 dB level. The $\varphi=0^\circ$ plane corresponds to the H-plane and the $\varphi=90^\circ$ plane corresponds to the E-plane, considering the coordinate system presented in Figure 17.

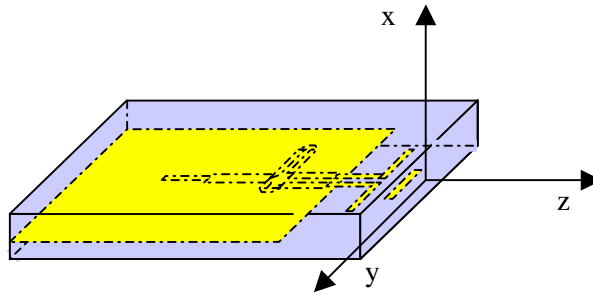


Figure 17. Yagi-like antenna in its coordinate system

The co-polarisation patterns in both planes exhibit similar behaviour in the upper half-space. The half-power beamwidths are 91° and 89° in the E- and H-planes, respectively. The cross-polarisation level is slightly higher in the E-plane, and reaches -24.8 dB in the boresight direction. The front-to-back ratio, reduced by the insertion of the director, drops to -13.6 dB.

Figure 20 and Figure 21 show the radiation patterns in the two main planes for different frequencies. The normalized patterns indicate that the half-power beamwidth is relatively constant within the operating bandwidth.

The variations of the radiation characteristics versus frequency are summarized in Figure 22 and Figure 23. The antenna exhibits a 6.7 dB gain at 44.5 GHz. The gain is varying from 6.2 dB to 6.7 dB over the bandwidth. The efficiency, only accounting for the dielectric and mismatch losses, is higher than 92%, and reached 96% at 44.5 GHz. The cross-polarisation level rises with frequency, but stays below -23 dB in the boresight direction (Figure 23). The front-to-back ratio also increases with frequency, and reaches -12.5 dB at 45.5 GHz. Overall, the radiation characteristics are stable over the frequency range of interest.

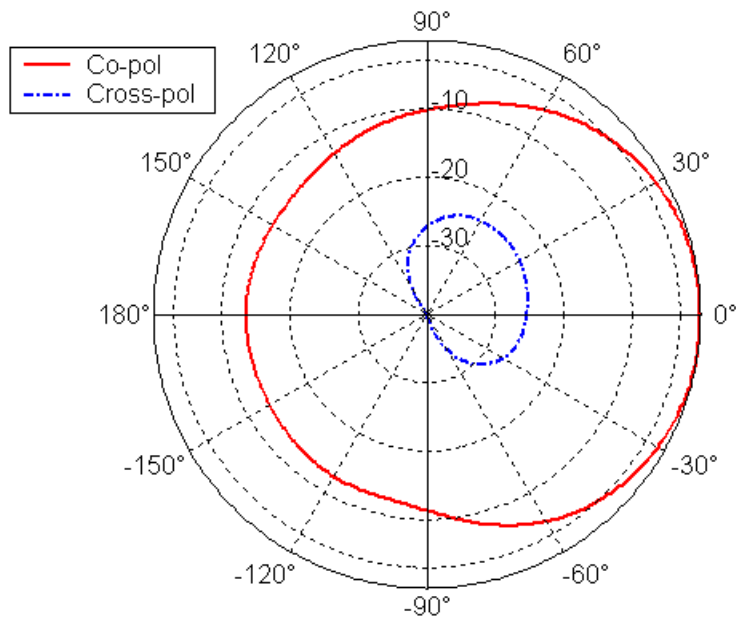


Figure 18. Radiation pattern in the $\varphi=0^\circ$ plane (H-plane)

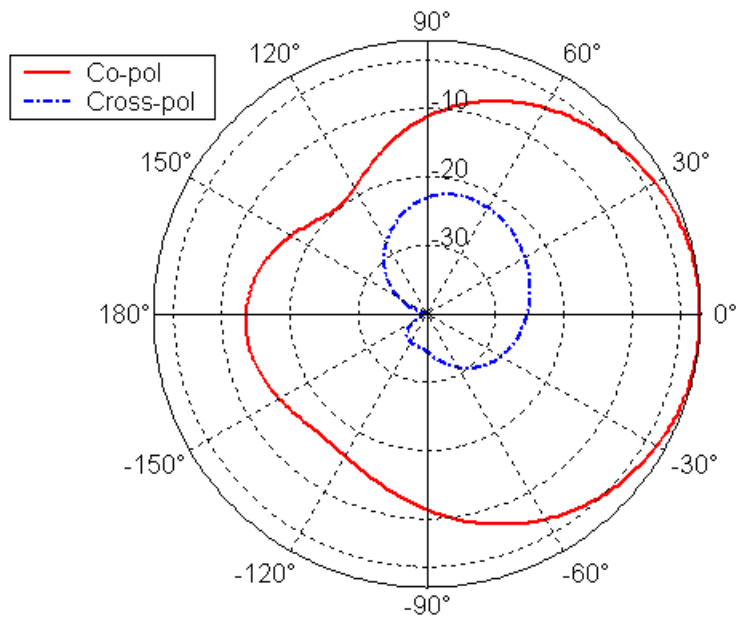


Figure 19. Radiation pattern in the $\varphi=90^\circ$ plane (E-plane)

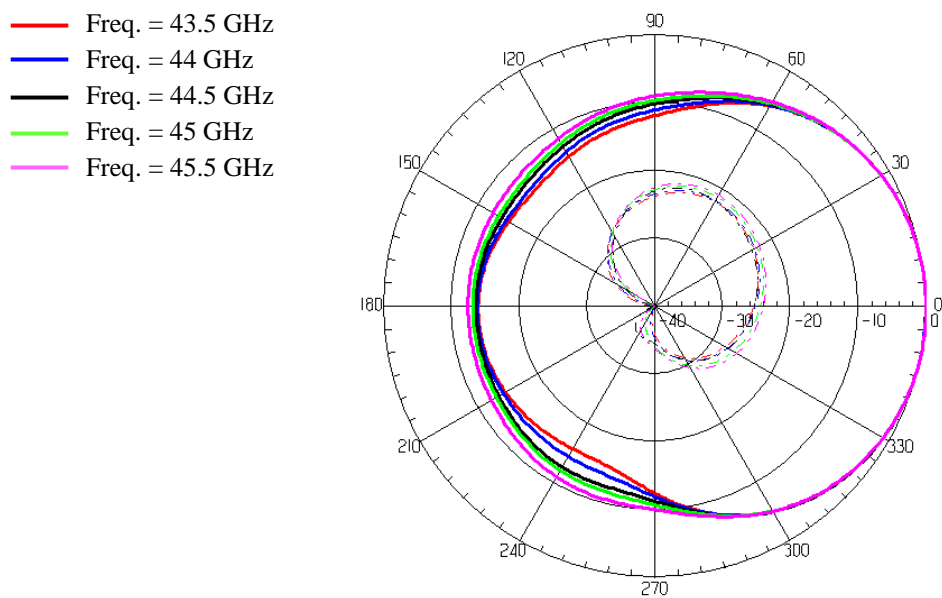


Figure 20. Radiation pattern in the $\varphi=0^\circ$ plane (H-plane) for different frequencies

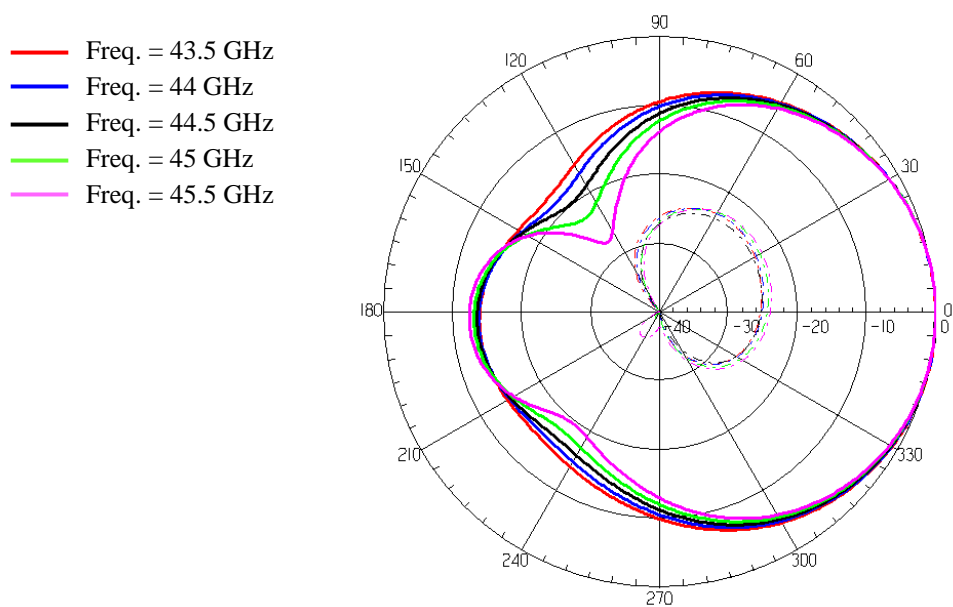


Figure 21. Radiation pattern in the $\varphi=90^\circ$ plane (E-plane) for different frequencies

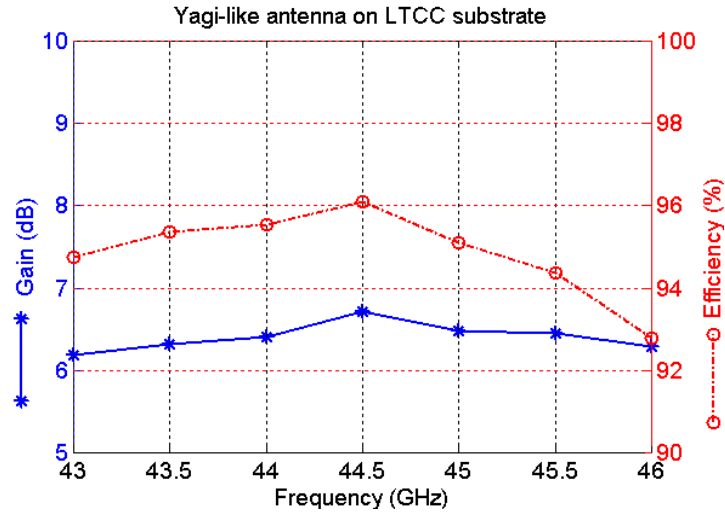


Figure 22. Gain and efficiency of the Yagi-like antenna

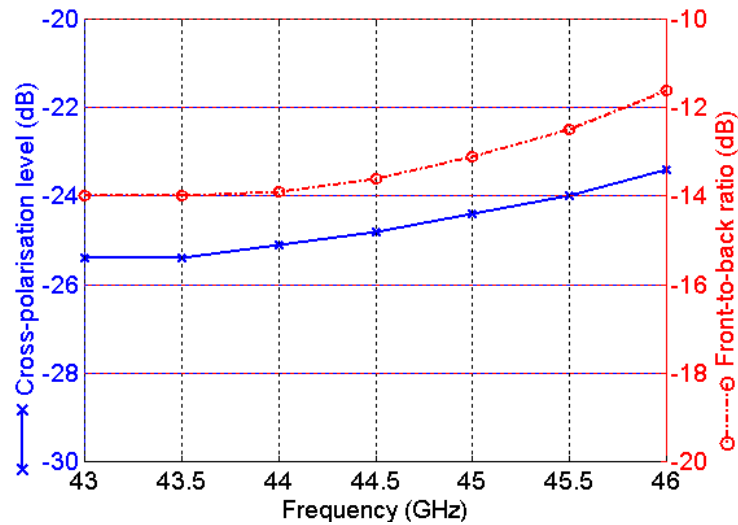


Figure 23. Cross-polarisation level in the broadside direction and front-to-back ratio of the Yagi-like antenna

The antenna and its feeding system were designed and fully characterized by simulation. As it is our first documented fabrication in LTCC technology and with VTT Electronics, additional passive circuits are added on the wafer to characterize the material and to learn about the fabrication process itself. Also, an open and a through line are needed to calibrate the vector network analyzer before measuring the different devices. The steps to design the different additional circuits are described in the next two sections.

3. Design of Microwave Circuits for Extraction of Material Parameters

Several methods for extracting material properties exist, as reported in [22]-[24] for instance. Our interest is focused on methods using printed circuits, since it is the technology that has been chosen for our designs. Two methods based on the resonant behaviour of microstrip circuits were chosen. The first one, which is the preferred method for extracting material properties, is based on the transmission measurement of a ring resonator. The second one is based on the measurement of a straight microstrip line loaded with an open stub, and is also called the T-junction method. With both techniques the material properties are extracted at specific resonant frequencies. The methodology to estimate the dielectric constant and the attenuation factor using the measurement of these circuits are described in this section.

3.1 Design of an embedded ring resonator

3.1.1 Theoretical background

A ring resonator, as shown in Figure 24, was designed to verify the electrical properties of the LTCC material. Both the dielectric permittivity and insertion loss can be extracted for several frequencies from the measurement of the transmission factor of this circuit [22], [23]. The ring resonator is one of the preferred circuit for the extraction of material parameters. Since it has no open ends, unlike a straight line resonator, it is almost free of radiating losses, which are mainly due to end effects [24]. Therefore, no correction factor needs to be introduced in the equations.

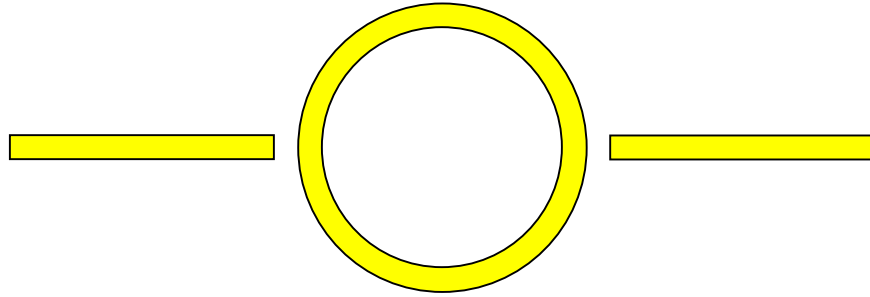


Figure 24. Ring resonator

The resonant frequencies of the ring resonator can be evaluated assuming that the mean circumference L_R of the ring is a multiple of the guided wavelength λ_g ,

$$(1) \quad L_R = 2\pi r_{mean} = n \lambda_g$$

or

$$(2) \quad r_{mean} = \frac{n \lambda_g}{2\pi} = \frac{n c}{2\pi f_R^n \sqrt{\epsilon_{eff}}}$$

where n is an integer, c is the velocity of light, ϵ_{eff} is the effective permittivity, and f_R^n corresponds to the n^{th} resonance frequency.

To avoid errors due to the curvature of the ring, a resonator of several wavelengths needs to be considered at the frequency of interest. On another hand, it will also allow the evaluation of the substrate characteristics at other lower frequencies, but with some errors.

Therefore, at each resonant frequency f_R^n , the dispersive effective dielectric permittivity can be deduced from equation (2):

$$(3) \quad \epsilon_{eff} = \left(\frac{n}{r_{mean}} \frac{c}{2\pi f_R^n} \right)^2$$

The effective dielectric permittivity of a buried microstrip line can be estimated using [25]

$$(4) \quad \epsilon_{eff, buried}(f) = \epsilon_{eff}(f) e^{(-2b/h)} + \epsilon_r [1 - e^{(-2b/h)}]$$

where ϵ_{eff} and $\epsilon_{eff, buried}$ are respectively the dispersive effective dielectric permittivity of a microstrip line and that of an embedded microstrip line, h is the thickness of the substrate between the ground plane and the microstrip line and b is the superstrate thickness.

The attenuation factor of the transmission line can be calculated using the following expression [26]:

$$(5) \quad \alpha_T = \frac{n \pi}{Q_o L_R} = \frac{n}{Q_o 2r_{mean}} \quad (\text{Neper/meter})^1$$

where Q_o is the unloaded quality factor of the ring resonator. Q_o is evaluated experimentally according to the following formula [26]:

$$(6) \quad Q_o = \frac{Q_L}{1 - S_{21}^n}$$

where S_{21}^n is the magnitude in linear scale of the transmission factor at the n^{th} resonance, and Q_L is the loaded quality factor deduced from the measurement:

¹ Multiply α_T by $20 \cdot \text{Log}(e) = 8.686$ to obtain α_T in deciBel per meter

$$(7) \quad Q_L = \frac{f_R^n}{\Delta f_R^n}$$

where Δf_R^n is the half-power bandwidth respective to S_{21}^n around the n^{th} resonance frequency.

The attenuation factor includes dielectric, metallic, radiation and surface wave losses [17]. In most cases, surface wave losses are negligible, as well as radiation losses. Analytical expressions of the dielectric and metallic losses were developped [27]. The corresponding attenuation factors, α_d and α_c respectively are expressed by [24]:

$$(8) \quad \alpha_d = 27.3 \frac{\epsilon_r (\epsilon_{eff} - 1) \tan \delta}{\sqrt{\epsilon_{eff}} (\epsilon_r - 1) \lambda_o} \quad (\text{dB/meter})$$

and

$$(9) \quad \alpha_c = 0.072 \frac{\sqrt{f}}{w Z_c} \frac{\lambda_o}{\sqrt{\epsilon_{eff}}} \quad (\text{dB/meter})$$

where $\tan \delta$ is the loss tangent and ϵ_r is the dielectric permittivity, λ_o is the free-space wavelength, w is the microstrip line width and Z_c is its characteristic impedance.

A more accurate expression of α_c takes into account the surface roughness (Δ) of the metallisation. The conductor loss attenuation factor then becomes:

$$(10) \quad \alpha'_c = \alpha_c \left[1 + \frac{2}{\pi} \arctan \left\{ 1.4 \frac{\Delta}{\delta_s} \right\} \right] \quad (\text{dB/meter})$$

with

$$(11) \quad \delta_s = \frac{1}{R_s \sigma} \quad \text{and} \quad R_s = \sqrt{\frac{\omega \mu}{2 \sigma}}$$

where δ_s is the skin depth, R_s is the surface resistance, σ is the metal conductivity and $\mu = \mu_o \mu_r$ is the permeability of the dielectric.

The expressions of the quality factors corresponding to the radiation losses and the surface wave losses are more complex, containing integral equations. They can be found in [17].

From measurements, and using the above equations, the dielectric permittivity and loss tangent can be estimated, as well as the metallization surface roughness for a given metal conductivity. This can be achieved if the radiation and surface wave losses can be neglected.

3.1.2 Design of the ring resonator

As previously mentioned, a ring resonator buried in the LTCC material is used to evaluate the transmission characteristics of a microstrip line. The gap between the microstrip lines and the ring resonator should be small enough to obtain the desired transmission factor. To avoid problems due to the fabrication tolerance on line spacing, the ring is placed one layer above the microstrip line. The final design is shown in Figure 24. The microstrip line width is 99 μm , which corresponds to a 50 Ω characteristic impedance. The ring width is 202 μm , which also corresponds to a 50 Ω characteristic impedance but for a microstrip line placed two layers above the ground plane (214 μm) with a three-layer superstrate (321 μm). The ring mean radius is 1.634 mm. Its electrical circumference has been evaluated considering the fourth resonance close to the operating frequency (44.5 GHz), assuming a dielectric permittivity of 7.1 and a loss tangent of 0.002. The metal conductivity is $6.17 \cdot 10^7$ S/m, and the metal thickness is set to 10 μm . The gap between the microstrip line ends and the ring is 265 μm wide. The resonant frequencies, deduced from eq. (1) and using eq. (4), are given in Table 1. As the effective permittivity is frequency dependant, frequencies of 11.1 GHz, 22.25 GHz, 33.4 GHz and 44.5 GHz are respectively considered for the evaluation of the effective permittivity. Note that in this particular case, the effective dielectric permittivity varies between 6.990 and 7.003.

Table 1. Resonant frequencies and transmission factors of the ring resonator circuit

Resonant Frequency from eq. (1) (GHz)	11.05	22.10	33.14	44.2
Resonant Frequency from Simulation (GHz)	11.3	22.4	33.3	44.1
Transmission Factor with ring (dB)	-31.9	-24.7	-20.75	-21.0
Transmission Factor without ring (dB)	-65.7	-49.9	-43.4	-30.4

Results of the transmission factors obtained by simulation using Zeland IE3D are shown in Figure 25. In this figure, the transmission factor between the two microstrip lines when the ring is removed is also given to indicate the level of the substrate mode propagation. Note that the transmission factor of the ring resonator at the fourth resonance reaches a maximum of -21 dB, while the transmission factor between the two microstrip lines when the ring is removed approaches -30 dB. The resonant frequencies and the corresponding transmission factors are listed in Table 1.

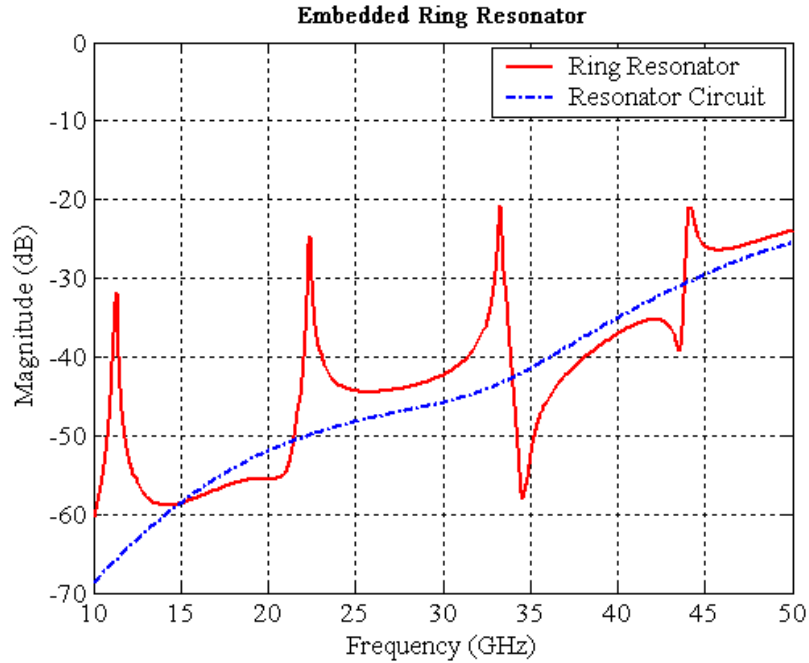


Figure 25. Transmission factor of the ring resonator circuit

The characteristics of the LTCC material can be deduced from the measurement of the fabricated circuits using the equations (3) to (7). The results are presented in section 6.

3.2 Extraction of the material characteristics using a transmission line loaded with an open stub

Another method is used to extract the material characteristics. It is based on the transmission factor measurement of a transmission line loaded with an open stub, as shown in Figure 26. This method is a resonant method called T-junction method [23], [24].

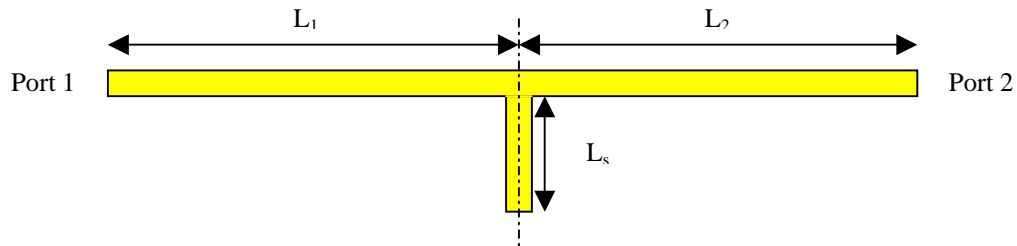


Figure 26. Microstrip transmission line loaded with an open stub

The transmission factor can be deduced analytically from the complete transmission matrix ABCD of this two port circuit. After calculations detailed in Appendix 3. , the S-parameters of this circuits are expressed by

$$(12) \quad S_{11} = -\frac{th\gamma L_s}{2 + th\gamma L_s} e^{-2\gamma L}$$

and

$$(13) \quad S_{21} = \frac{2}{2 + th\gamma L_s} e^{-2\gamma L}$$

where $\gamma = \alpha + j\beta$ is the propagation constant, L_s is the stub length and $L=L_1=L_2$ is half the transmission line length.

If the transmission line is lossless ($\gamma = j\beta$), the reflection coefficient and the transmission factor become

$$(14) \quad S_{11} = -j \frac{\tan(\beta L_s)}{2 + j \tan(\beta L_s)} e^{-2j\beta L}$$

and

$$(15) \quad S_{21} = \frac{2}{2 + \tan(\beta L_s)} e^{-2j\beta L}$$

The extrema of the transmission factor are obtained when

$$(16) \quad \beta L_s = q \frac{\pi}{2} \quad \text{where } q \text{ is an integer.}$$

The case $q=2n$, where n is an integer, corresponds to the maxima of the transmission factor, and the minima of the reflection coefficient ($\Gamma = -20 \text{ Log } |S_{11}|$). Knowing that $\beta = \frac{2\pi f \sqrt{\epsilon_e}}{c}$, where f is the frequency, c the velocity of the light and ϵ_e the effective permittivity, this condition is verified for

$$(17) \quad f_M = \frac{n}{2} \frac{c}{\sqrt{\epsilon_e}} \frac{1}{L_s}$$

The minima of the transmission factor are obtained for $q=2n+1$, or

$$(18) \quad f_m = \frac{2n+1}{4} \frac{c}{\sqrt{\epsilon_e}} \frac{1}{L_s}$$

Considering an operating frequency f_o of 45 GHz and an open stub length of three-quarter of guided wavelength at the operating frequency, the first and second minima are obtained for $n=0$ and $n=1$:

$$f_M = \frac{2}{3} f_o = 30 \text{ GHz} \quad \text{and} \quad \begin{cases} f_{m1} = \frac{1}{3} f_o = 15 \text{ GHz} \\ f_{m2} = f_o = 45 \text{ GHz} \end{cases}$$

Simulations of this circuit have been carried out with Zeland IE3D software package [15]. The simulations have been performed for different metal conductivities, substrate dielectric constants and loss tangents, as shown in Figure 27. The influence of the loss tangent and the metal conductivity is on the magnitude of the S-parameter depths. A frequency shift of the responses could occur only if there was a discrepancy between the specified and measured dielectric permittivity of the material. The results of the simulations are summarized in Table 2.

Table 2. Summary of the characteristics of a 3λ microstrip line loaded with a $3\lambda/4$ open stub

ϵ_r	$tg\delta$	σ (S/m)	f_{m1} (GHz)	$ S_{11} / S_{21} $ (dB)	F_M (GHz)	$ S_{11} / S_{21} $ (dB)	f_{m2} (GHz)	$ S_{11} / S_{21} $ (dB)
7.1	0.002	6.173e7	14.9	-0.35 / -36.0	30.6	-41.3 / -0.45	44.2	-0.95 / -22.7
7.1	0.010	6.173e7	14.9	-0.675 / -32.8	30.6	-36.5 / -1.0	44.2	-2.0 / -20.1
7.1	0.002	1.0e7	14.9	-0.625 / -33.7	30.6	-39.7 / -0.75	44.2	-1.45 / -21.3
6.9	0.002	6.173e7	15.2	-0.35 / -36	31.2	-41.4 / -0.45	44.9	-1.0 / -22.8

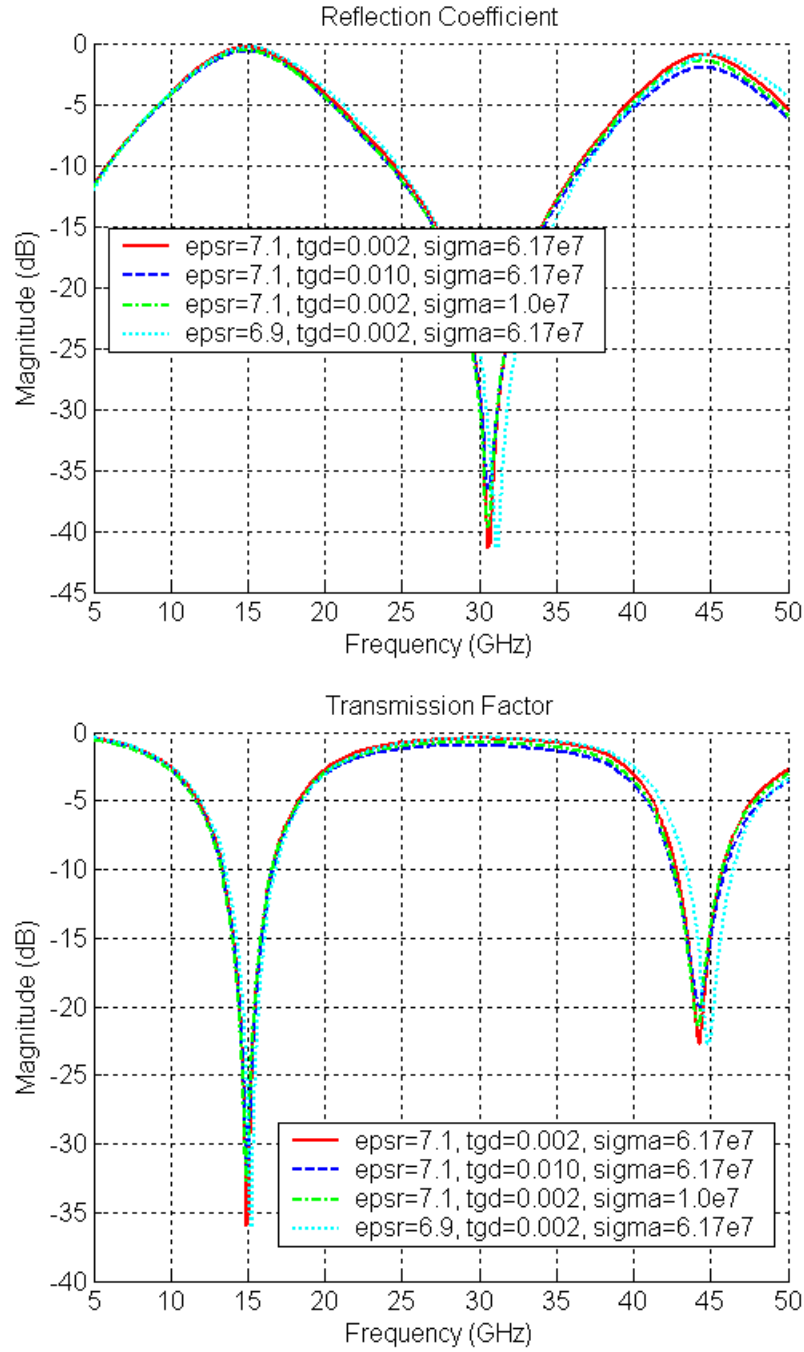


Figure 27. *S-parameters of the 3λ transmission line loaded with an $3\lambda/4$ open stub*

The characteristics of the LTCC material can be deduced by comparison of the simulation and measurement of the fabricated circuits. The results are presented in Section 6.

4. Design of the Calibration Lines for TRL Measurement

Different calibration techniques for measuring printed circuits exist [28], but one of the most popular and reliable is the TRL (Through-Reflect-Line) calibration. The TRL calibration is composed of three steps [28]:

- a “thru” step, where a section of transmission line is connected between the two ports of the network analyzer,
- a “reflect” step, where the section of transmission line is cut in half and the two halves are separated, making an open circuit for each port,
- a “line” step, where a short section of transmission line is connected to both ends of the halves of the previous transmission line. Usually, a quarter wavelength line is considered.

As mentioned in [28], the length of the line is not critical, but its optimal length should correspond to a 90° phase shift at the centre frequency. It is also recommended that the phase remains in the range of 20° to 160° at any frequency of measurement. This constraint fixes the bandwidth over which the calibration is valid.

As all the circuits to be measured are embedded in the LTCC material, the calibration lines are designed with the same configuration. Therefore, the line is printed one layer above the ground plane ($107\ \mu\text{m}$) and covered with a four-layer superstrate ($428\ \mu\text{m}$). Assuming a dielectric constant of 7.1 at 44.5 GHz, the quarter wavelength line is 0.625 mm. A 0.625 mm long microstrip line corresponds to a 20° phase shift for $F_{\min} = 10\ \text{GHz}$, and to a 160° phase shift for $F_{\max} = 80\ \text{GHz}$. The layout of the calibration lines can be found in Appendix 4.

5. Layout of the Circuits for Fabrication

Once all the designs are finalized after optimization using the simulation tools, one needs to layout the circuits for fabrication. A transition needs to be added to each circuit to feed it. Indeed, all our circuits are embedded into the material. A cavity needs to be created for the probe to access the circuit feeding lines, as shown in Figure 28. The cavity size is 3.0 mm by 4.5 mm. The total substrate thickness corresponds to eight LTCC layers.

Changes in the number of layers were made at this point because of the design constraints due to the presence of the cavity. The substrate thickness below the cavity must be at least $380\text{ }\mu\text{m}$, which corresponds to a total of four layers in our case. To keep the radiating antenna in the middle of the substrate thickness, another layer was added on top of the substrate. The total number of layers increased from six (considered in the design stage) to eight. However, the characteristics of the different circuits were not drastically perturbed, and the dimensions were kept as previously defined.

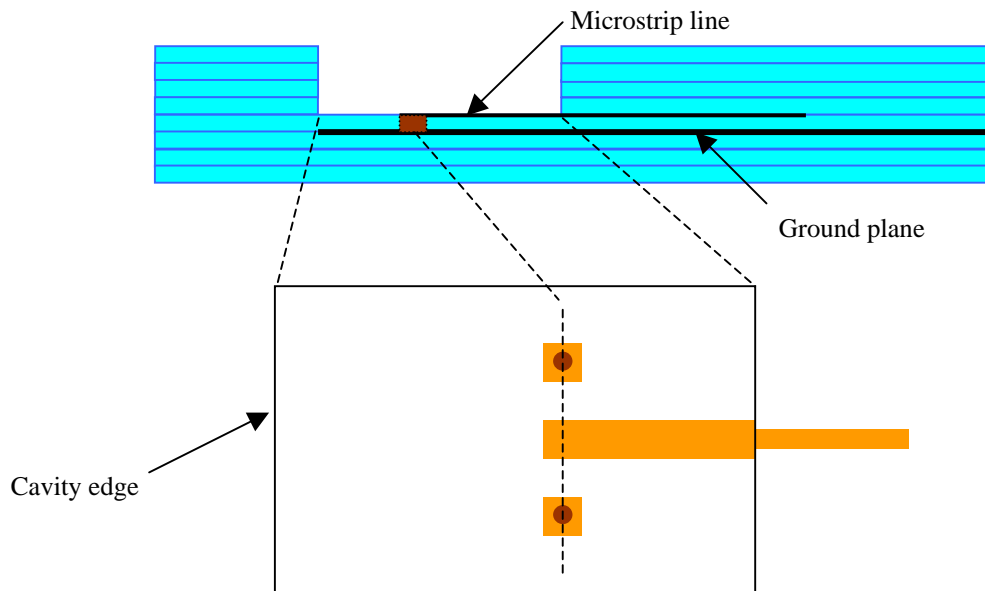


Figure 28. Cavity for probe circuit access

Also, since a CPW probe is used, vias are inserted on both sides of the microstrip line to access the ground plane. The centre-to-centre distance between the via pads and the microstrip line is $500\text{ }\mu\text{m}$, which corresponds to the distance between the probe tips. The via diameter is $150\text{ }\mu\text{m}$, and the square via pads dimension is $250\text{ }\mu\text{m}$. Without superstrate, the $50\text{ }\Omega$ microstrip line is $125\text{ }\mu\text{m}$ wide.

For fabrication purposes, the design must be described using several layers. Each layer represents a separate operation, such as etching the metalization, creating a cavity in the substrate, or filling a via hole. Figure 29 represents the complete layout of the LTCC run. All the layers are superimposed on this graph. Each colour corresponds to one layer. The circuits relative to this study, the Yagi-like antennas, the ring resonator and the calibration lines are shown with a blue ground plane in the upper right corner. The green rectangles are the cavities.

Some transmission lines of different lengths were added to this run to allow for the verification of the quality of the calibration and the extraction of the insertion loss. Three-wavelength lines with and without an open stub placed in the middle were also added to verify the dielectric constant and the microstrip-line insertion loss of the LTCC material. More detailed layouts of the calibration lines, the Yagi-like antenna and the ring resonator circuits, are provided in Appendix 4. Four Yagi-like antennas having exactly the same dimensions were considered for this run. The only difference between the antennas was the distance between the director and the edge of the substrate, as this parameter is critical in terms of the input impedance. Distances of 1.2 mm, 1.3 mm, 1.4 mm and 1.5 mm were chosen.

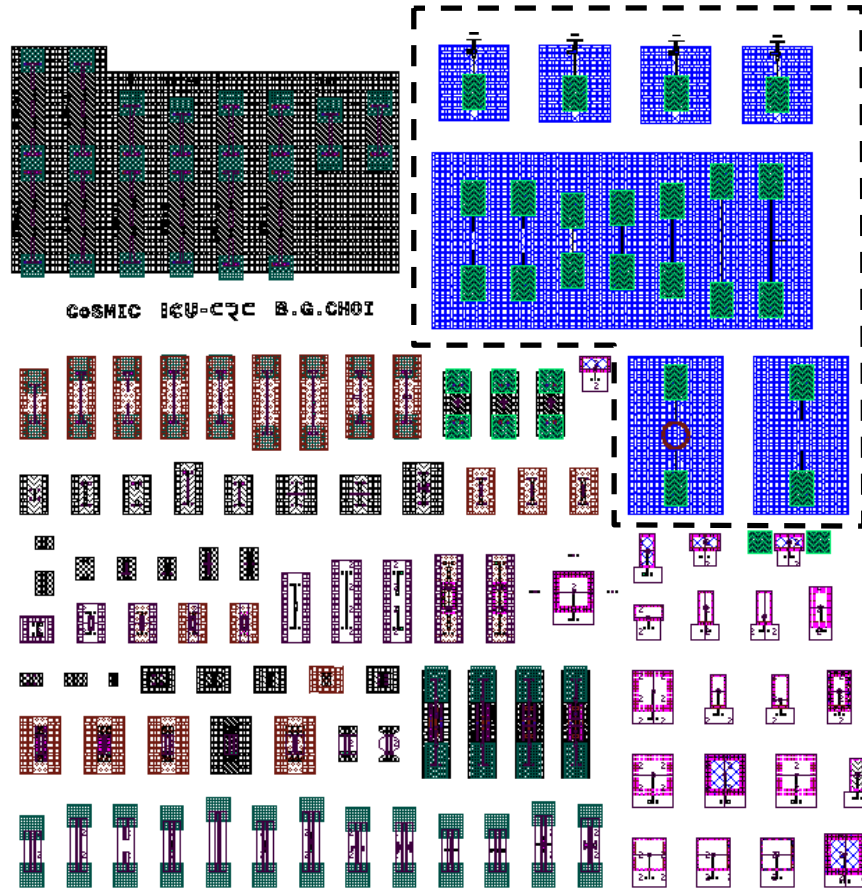


Figure 29. Layout of the complete LTCC run

6. Measurement and Analysis

The complete layout was fabricated at VTT Electronics in Finland. The circuits were realized on three different boards, or wafers, processed at different times. Figure 30a shows a picture of the four antennas placed at different distances from the LTCC substrate edge. Note that only the transitions in the cavities are visible, as the antennas with their feeding circuits are embedded in the material. A closer picture of one cavity is presented in Figure 30b. The via pads and the microstrip line are completely visible. The via pad and the microstrip line have been magnified and the resulting pictures are given in Appendix 5.

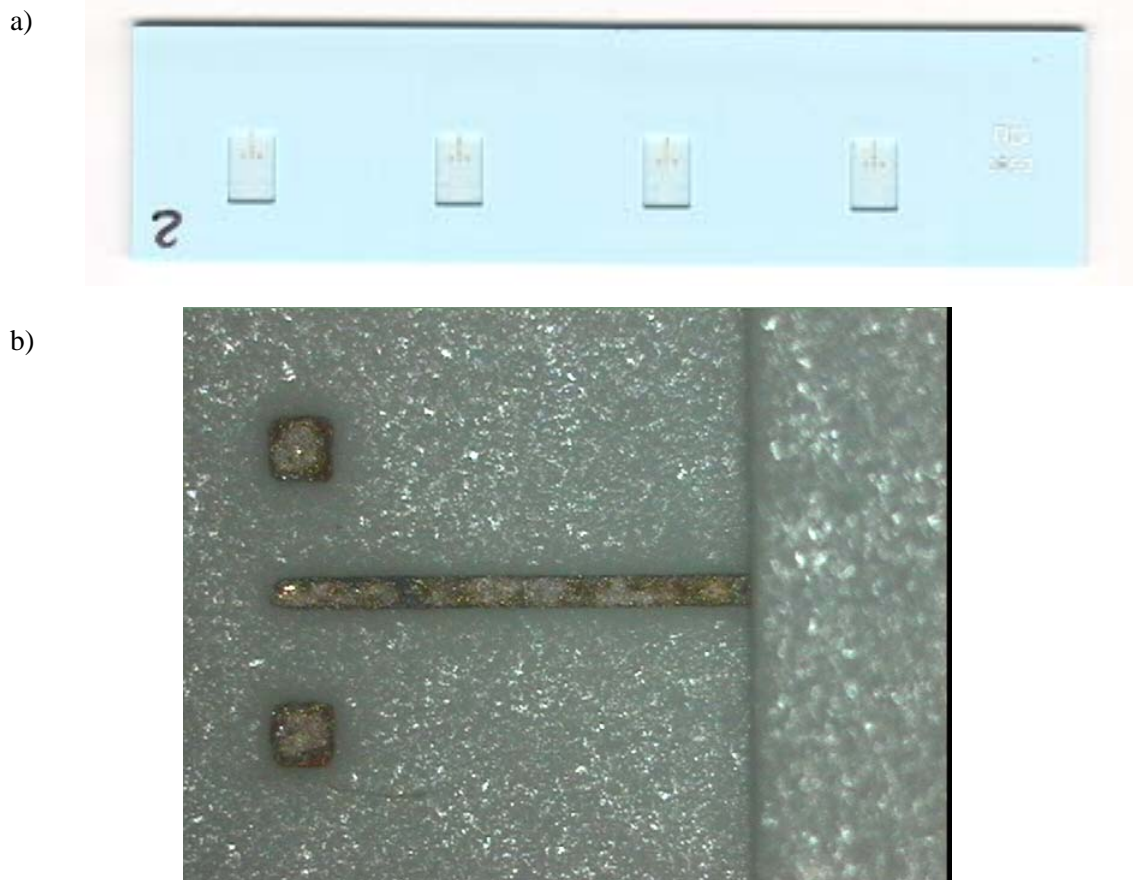


Figure 30. Picture of a) the four different Yagi-like antennas, circuit #2, and b) the launcher part of the Yagi-like antenna #1 circuit #2 (October 2003)

The measurements of the S-parameters were carried out with a probe station at the Integrated Microwave and Millimetre wave Circuits laboratory at CRC. Due to the heavy use of the probe station, three sets of measurements were done at different times. The first set, done in

June 2003, consisted of wideband measurements using both OSL (Open-Short-Load) and TRL calibration methods, and the second and third sets, done in October 2003 and January 2004, respectively, consisted of several narrow band measurements using the TRL calibration method. All the measurements were saved on files, which names are listed in Appendix 6. The pictures, which were taken in October 2003 (see Figure 30 and Appendix 5), show some oxydation of the silver. The oxydation occurred because the circuits were not stored in a controlled environment. This oxydation degraded the contact between the probe and the line, and may significantly affect the measurements. Note that the oxydation appeared after the measurement carried out in June 2003.

Before reporting the measurements of the S-parameters of the different circuits, the dimensions of different circuits fabricated on different wafers, were measured. The analysis is presented in the following sub-section.

6.1 Dimensions measurements

Measurement of different dimensions were carried out to ensure that the conductor dimensions optimized by simulation were correctly reproduced with the LTCC process, and that the material shrinkage was well controlled during the fabrication. The visible microstrip line and the via pad dimensions, as well as spacing, were measured on different wafers with a microscope and a calibrated micrometre ruler. The distance between the ports of the two-port circuits (the ring resonator and the three-wavelength microstrip line loaded with an open stub) and the distance between the microstrip feeding lines of the Yagi-like antennas were also measured for a better estimation of the material shrinkage along the X- and Y-axes. The results are summarized in Table 3 and Table 4.

It was noted that the measured microstrip line and pad dimensions of the launchers of the ring resonator and the loaded three-wavelength microstrip line circuits are smaller than the designed dimensions (Table 3). The dimension variations are different but of the same order from one wafer to another, and from one circuit to another on any given wafer. Specifically, the 125 μm wide microstrip lines became as narrow as 102 μm on wafer #1. The corresponding characteristic impedance is 58 Ω instead of 50 Ω . On wafer #2, the microstrip line width of one of the launcher is 110 μm for both measured circuits (which corresponds to a 56 Ω characteristic impedance). On wafer #3, the line widths are comparable to the expected line width. The measure of the port to port distance and of the centre pad to centre pad distance confirms that the shrinkage is well controlled, as the average dimension variations from the designed model are respectively -0.28% along the X-axis and 0.76% along the Y-axis.

Table 4 reports the measurement of the conductor dimensions of the Yagi-like antenna launchers of wafer #2. The results are comparable to the measurement realized on the visible conductors of the ring resonator and the loaded three-wavelength microstrip line circuits. The measurement of the distance between two adjacent microstrip feeding lines indicates a dimension difference along the X-axis of 0.07% . The average difference between the centre pad to centre pad distances is 1.37% , slightly higher than the value found with the previous two-port circuits.

Table 3. Dimensions of the launchers of the ring resonator and three-lambda microstrip line loaded with an open stub circuits

		Design	Wafer #1		Wafer #2		Wafer #3	
			Line resonator	Ring resonator	Line resonator	Ring resonator	Line resonator	Ring resonator
Microstrip line (microns)	width	125	102	109	110	110	128	120
	length	1725	1715	1725	1722	1695	1714	1719
Top pad (microns)	width	250	222	220	228	223	247	242
	length	250	220	217	224	220	236	229
Bottom pad (microns)	width	250	212	221	224	215	238	231
	length	250	216	220	223	215	238	230
Distance between line and ...	top pad (microns)	312.5	344	338	339	337	318	321
	bottom pad (microns)	312.5	341	338	336	345	321	327
Overall distance (microns)	added dimensions	1250	1221	1226	1237	1230	1252	1241
	measured	1250	1218	1223	1238	1228	1249	1244
Port to port distance (mm)	Line	14.15	14.113	/	14.103	/	14.14	/
	Ring	12.65	/	12.608	/	12.59	/	12.621
Centre pad to centre pad distance (mm)		1	1.004	1.0055	1.011	1.011	1.0095	1.0045
Difference (%)	Port to port distance (along X axis)	0	-0.26	-0.33	-0.33	-0.47	-0.07	-0.23
	Centre pad to centre pad (along Y axis)	0	0.40	0.55	1.10	1.10	0.95	0.45

Overall, the measurement of the dimensions shows that:

- The material shrinkage is globally well controlled,
- The conductor width of the fabricated circuits is smaller than the designed value. The characteristic impedance of the lines is therefore different than the expected one. This undoubtedly creates some discrepancies between the simulation and the measurement of the S-parameters.
- The circuits realized on different wafers have slightly different dimensions.

In addition to the above comments, human factors should also be taken into account in the precision of the measurement. For instance, the microstrip line width fluctuates a bit along its length, and a decision must be made for determining its average width. Also, the dimension measurements concern the accessible conductors. We can only guess, to date, that the buried conductors are following the observations made on the visible conductors.

Table 4. Dimensions of the Yagi-like launchers on wafer #2 (and wafer #3)

		Design	Wafer #2				Average	Difference (%)
			Antenna #1	Antenna #2	Antenna #3	Antenna #4		
Microstrip line (microns)	width	125	114	108	112	110	111.00	11.2
	length	1725	1700	1721	1711	1727	1714.75	0.59
Top pad (microns)	width	250	225	223	222	220	222.50	
	length	250	224	229	229	225	226.75	
Bottom pad (microns)	width	250	220	222	222	224	222.00	
	length	250	220	222	226	226	223.50	
Distance between line and ...	top pad (microns)	312.5	335	343	340	345	340.75	
	bottom pad (microns)	312.5	344	341	338	336	339.75	
Overall distance (microns)	added dimensions	1250	1238	1237	1234	1235	1236.00	1.12
	measured	1250	1239	1237	1234	1230	1235.00	1.20
line to line distance (mm)		13.05	0	13.06	26.12	39.176	13.06	0.07
centre pad to centre pad distance (mm)		1	1.0155	1.0145	1.012	1.013	1.01	1.37
Difference (%)	centre pad to centre pad		1.55	1.45	1.20	1.30	1.37	
	overall distance		0.92	1.04	1.28	1.40	1.16	
			Wafer #3					
line to line distance (mm)		13.05	39.16	26.105	13.051	0	13.05	0.02

The S-parameter measurements and the analysis of the different circuits (the ring resonator, the T-junction circuit, the embedded microstrip transmission lines and the Yagi-like antennas) are presented in the following sub-sections.

6.2 Extraction of the material properties

Two resonant circuits were designed to extract the material properties of the Dupont 943 LTCC substrate, the effective dielectric constant and the attenuation factor. The theory was summarized in Section 3. The results and the data analysis of the ring resonator and the three wavelength transmission line loaded with a three-quarter of wavelength open stub are presented in the following sub-sections. In addition, the S-parameter measurements of the embedded microstrip transmission lines are analyzed to confirm the material properties.

6.2.1 Measurement of the ring resonator

Figure 31 presents the S_{12} transmission factor of all the measurements of the ring resonator of wafer #1. The result of the simulation with IE3D of the ring resonator is also plotted for comparison purpose. The S_{21} transmission factors are not shown, because they are identical to the S_{12} parameters as the ring resonator is a passive circuit. The measurements confirm this fact but only when the calibration has been realized with the TRL method. Some discrepancies occur when the OSL calibration method is used. The ring resonators on wafer #2 and wafer #3 were also measured in January 2004. The graphs corresponding to the S_{12} responses are reported in Appendix 7.

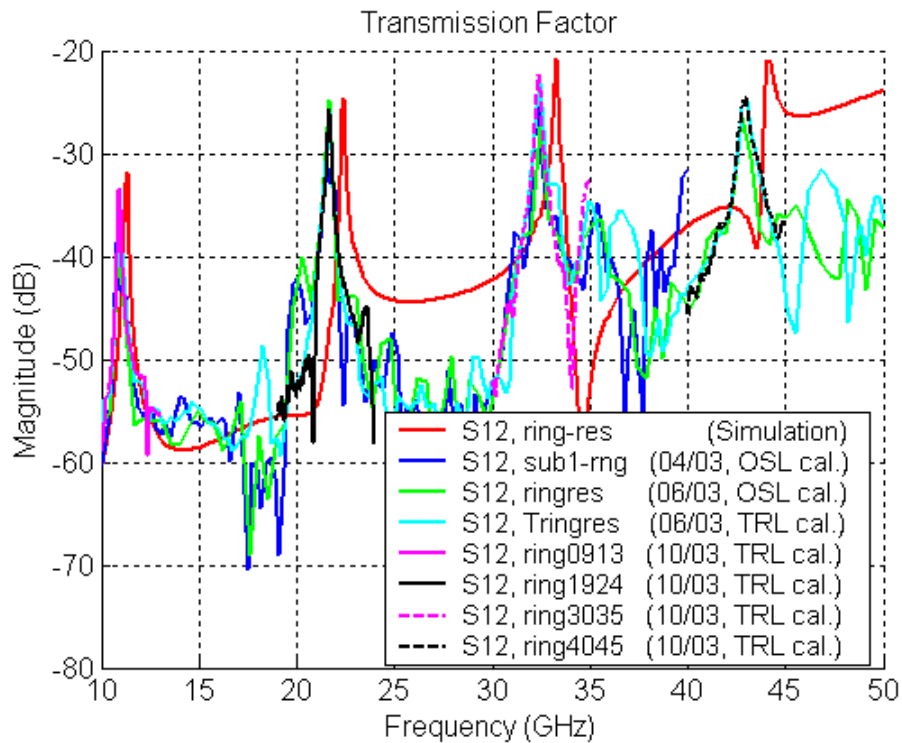


Figure 31. Transmission factor of the ring resonator

A first look at the graph of Figure 31 indicates that a frequency shift occurs between the simulation and the measurements. The resonant frequency discrepancies can be the results of two main factors. First, the dielectric permittivity of the material is not the value considered for simulation. Second, the dimensions of the fabricated ring resonator are not exactly the dimensions determined at the design stage. A combination of the two discrepancies could also occur. Also, some researchers [29] have noticed that the printed lines of the realized circuits were not exactly on top of the LTCC layers, but buried somewhere between the layers, as shown in Figure 32. This effect can modify the gap length between the ring and the microstrip lines, and therefore the S-parameter responses. In effect, the narrow gap between these two entities introduces a capacitive loading to the resonator circuit, which modifies the resonant frequencies [26], [30]. However, the difference between the measured resonant frequencies with and without considering the capacitive loading effect is small, considering the results reported in [31] (the ring resonator was printed on top of a 943 LTCC substrate). The frequency shift is only 0.4% on average, which introduces an average error of 0.8% for the effective permittivity. The correction for taking into account the capacitive loading is therefore not applied for this study.

A close look at the graph in Figure 31 shows that a frequency shift appears between the measurements done in April and June is that the frequency steps are relatively large. One of the reasons is related to the wideband measurement setup. The frequency steps are 232 MHz, 450 MHz, 20-25 MHz and 20-25 MHz for the measurements done in April 2003, June 2003, October 2003 and January 2004 respectively (20 MHz steps for the 9 to 13 GHz measurement, and 25 MHz for the other measurements). For more accuracy, only the measurements obtained with a TRL calibration and using a narrow bandwidth (20-25MHz steps) are considered for analysis.

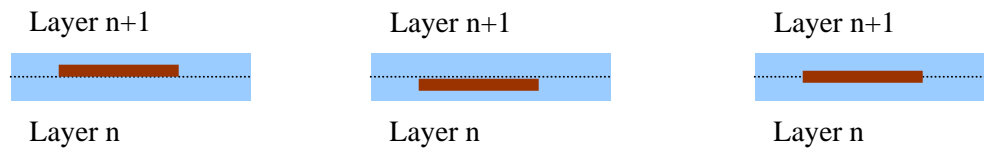


Figure 32. Possible conductor configurations in a multi-layer LTCC substrate

Table 5 summarizes the results of the ring resonator measurements on wafer #1 to wafer #3. They also contain the deduced effective permittivity, the loaded and unloaded quality factor and the attenuation factor at the different measured resonant frequencies. Table 6 presents for comparison the same data but from the simulation of the ring resonator. The simulation was realized with IE3D (see paragraph 3.1.2). The results of the measurement of the ring resonator measurement are given for each wafer in Table 10 to Table 12 in Appendix 7.

The resonant frequencies measured on all the wafers are similar. The discrepancy between their average is less than 0.3%. Therefore, the effective permittivities calculated using equation (3) with the data coming from the three different wafers are close, within 0.5% from their average. The relative permittivity, deduced from equation (4), varies from 7.2 at 11 GHz to 7.5 at 43 GHz. The material characteristics of the DuPont 943 Green Tape have been previously measured using different methods [31]-[35]. Note that References [32] to [35] are

publications of scientists working for DuPont. Figure 33 shows the dispersive relative permittivity obtained from our measurements and from previous studies. Our results with the ring resonator (7.2 to 7.5) are in between the results of previous studies. The ring resonator method used in [31] is showing higher permittivity (about 7.5 in average) than the “*open resonator measurement technique on unmetallized samples*” used in [33] ($\epsilon_{\text{eff}} = 7.05$). Compared to the previous studies, our measurements show that the dielectric permittivity is quite dispersive, exhibiting a frequency variation of 4%.

Table 5. Averaged results of the ring resonator measurements performed with TRL calibrations

Frequency (GHz)	10.973	21.713	32.383	42.983
Transmission Factor (dB)	-31.717	-24.625	-21.800	-24.300
3dB bandwidth (GHz)	0.122	0.200	0.285	0.573
Effective permittivity	7.091	7.245	7.328	7.395
Deduced relative permittivity	7.202	7.355	7.435	7.498
Loaded Quality Factor	92.813	109.172	114.681	76.144
Unloaded Quality factor	95.353	115.980	124.876	81.100
Attenuation Factor (dB/m)	28.722	46.036	64.488	133.133

Table 6. Results from simulation of the ring resonator (ring_res_embedded_20dB file)

Resonant Frequency (GHz)	11.3	22.4	33.3	44.1
Transmission Factor (dB)	-31.9	-24.7	-20.75	-21
3dB bandwidth (GHz)	11.175 / 11.34	22.27 / 22.455	33.185 / 33.385	43.985 / 44.505
	0.165	0.185	0.2	0.52
Effective permittivity	6.687	6.807	6.930	7.025
Loaded Quality Factor	68.485	121.081	166.500	84.808
Unloaded Quality Factor	70.270	128.565	183.315	93.106
Attenuation Factor (dB/m)	37.824	41.347	43.497	114.188

The transmission factors measured on all wafers are within 3.35dB for the first resonance, 2.25 dB for the second resonance, 1 dB for the third resonance and less than 0.5 dB for the fourth resonance. The half-power bandwidths measured around each resonant frequency are quite different from one wafer to another. The difference between the measured half-power bandwidth and their average respective to the resonant frequency is about 15% for the first resonance, 7.5%, 8% and 12% for the second, third and fourth resonance respectively. The unloaded quality factors are deduced from measurement using equations (6) and (7). The average attenuation factor calculated using equation (5) is indicated in Table 5. The average attenuation factor varies from 28.7 dB/m at 11 GHz to 133 dB/m at 43 GHz. The attenuation at 43 GHz is twice the value obtained at 32 GHz. This increase is due to the contribution of the the surface wave propagation, which becomes more important at high frequency.

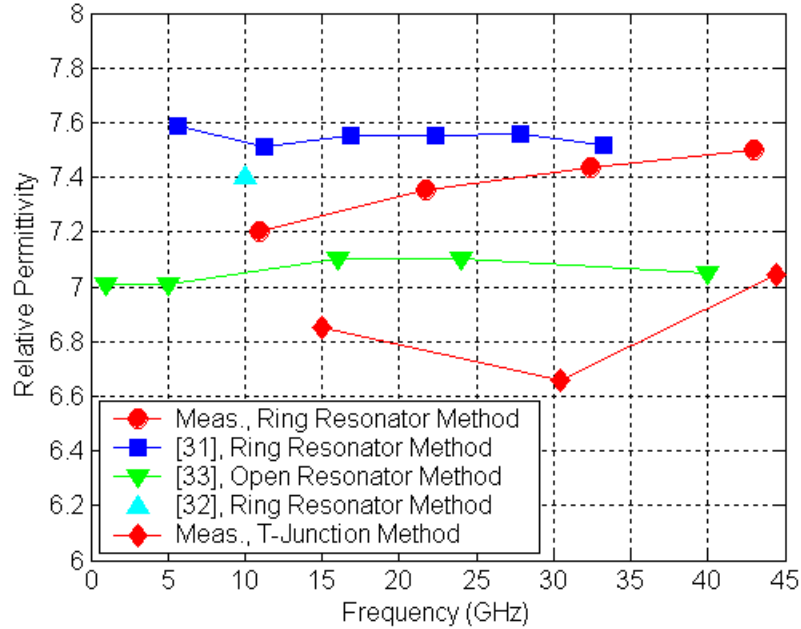


Figure 33. Relative permittivity deduced from various measurements

Our results are compared to those reported in [31], [33] and [35] in Figure 34. The ring resonator method is used in [31] and [35] whereas the T-junction method is used in [33]. It was observed that our measurement led to a higher attenuation factor than the results reported in the cited papers, regardless of the measurement method. Scientists from Dupont ([33], [35]) indicate the lowest attenuation factor. According to their measurement, the 943 LTCC green tape exhibits an attenuation factor of only 12 dB/m at 20 GHz, and reaches about 20 dB/m at 26 GHz [32]. As mentioned previously, our ring resonator is embedded in a substrate of a total of 5 layers above ground (two layers between the ring and the ground and a three-layer superstrate). This material is very thick in terms of wavelengths at high frequencies. Therefore, unwanted propagation, like surface wave propagation, appear to be non-negligible and even important. This mostly explains the high attenuation factor of the embedded microstrip transmission line.

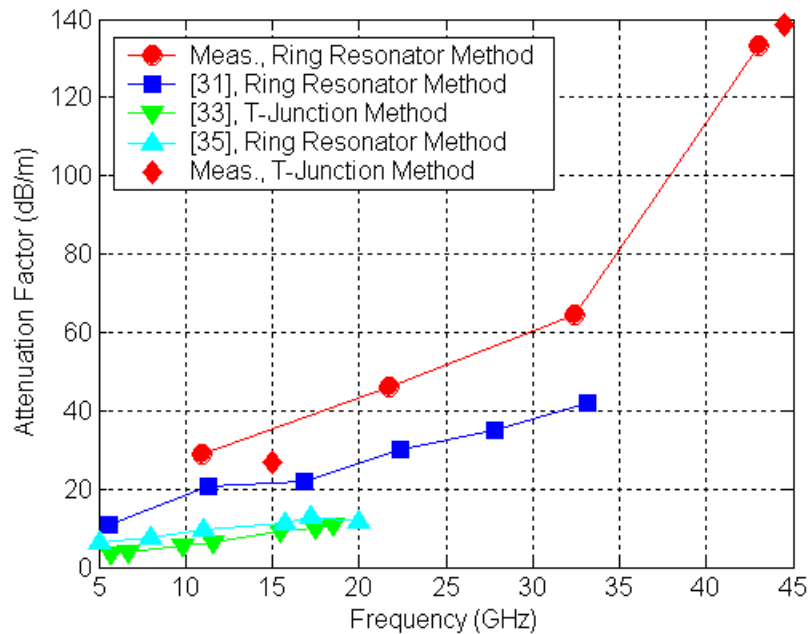


Figure 34. Comparison of various attenuation factor measurements

The next paragraph describes the analysis of the measurement of the transmission line loaded with an open stub. This circuit is also used for extracting the dielectric permittivity and the attenuation factor of a microstrip line. This method is called the T-junction, or T-pattern, method.

6.2.2 Measurement of the transmission line loaded with an open stub (“T-junction”)

The T-junction method described theoretically in section 3.2 has been used to extract the material properties of the LTCC green tape in terms of dielectric and attenuation constants. The measured data for each wafer, and the deduced constants, are given in Table 13 to Table 15 in Appendix 7. Table 7 presents the averaged results. The graphs representing the S-parameter responses are reported in Figure 51 (also in Appendix 7.) for the three wafers. The resonant frequencies obtained for each wafer are close, and agree quite well with the resonant frequencies given by theory and simulation. The effective dielectric permittivity deduced from equations (17) and (18) fluctuates between 6.66 and 7.04. The relative permittivity, obtained with equation (4)², is not much different from the effective permittivity because the microstrip transmission line is covered with four LTCC layers, which confine the near field within the substrate. The values are plotted versus frequency in Figure 33 along with data coming from different measurements. These results are lower, especially when compared to results obtained with the ring resonator method, and at 30 GHz. However, the value of the dielectric

² The equivalent stub length taking into account the microstrip line open-ended effect is used instead of the physical stub length L_s .

permittivity estimated at 45 GHz agrees quite well with the results reported in [33]. The reason for the difference could come from several factors. One of them is that the mismatch between our circuit and the Vector Network Analyser's (VNA) input impedance was not taken into account. This can shift the measured resonant frequencies. The reflection coefficient measurements of the circuits on wafer #1 and #3 are good examples; the responses of ports 1 and 2 do not exhibit the same resonant frequencies.

Table 7. Averaged results of the “T-junction” measurements realized with TRL calibrations

Frequency (GHz)	15.023	30.475	44.450
Transmission Factor (dB)	-35.85		-20.85
3dB bandwidth (GHz)	0.153		0.852
Effective permittivity	6.851	6.659	7.042
Deduced relative permittivity	6.85	6.66	7.043
Loaded Quality Factor	98.072		53.684
Unloaded Quality Factor	99.679		58.971
Attenuation Factor (dB/m)	26.693		138.753

The transmission factors measured on all wafers are within 0.5 dB for the first resonance and 2 dB for the third resonance. The half-power bandwidths measured around each resonant frequency are similar for the first resonant frequency, but are quite different for the third resonance from wafer #1 and wafers #2 and #3. The unloaded and loaded quality factors (deduced from measurement using equations (6) and (7)) are similar for the first resonance, but different for the third resonance measured on wafer #1. The average attenuation factor calculated using equation (5) is indicated in Table 7. The average attenuation factor equals 26.7 dB/m at 15 GHz to 139 dB/m at 44.5 GHz. The data are plotted in Figure 34 along with the measured attenuation factors reported by others. The attenuation factor deduced from the measurement of the T-junction circuits are in good agreement with the attenuation factor results deduced from the measurement of the ring resonators.

Other methods for extracting the attenuation factor exist. Two methods based on the measurement of the insertion loss of a simple microstrip transmission line are applied to verify the results found with the resonator circuits, as the measured data were available. This is described in the next sub-section.

6.2.3 Extraction of the attenuation factor using transmission line measurement

Two methods can be used for evaluating the attenuation coefficient from the measurement of straight microstrip lines. The first method is called the “Absolute Magnitude” method, and the second one is called the “Line Comparison” method. With the absolute magnitude method, which is a rudimentary method, the attenuation factor is estimated from the transmission factor measurement of a transmission line of length l . With the line comparison method, the attenuation factor is extracted from the difference of the transmission factor of two lines of different lengths. Both methods have been used in [31] for evaluating the attenuation factor of

a microstrip transmission line realized on LTCC material. The results are compared to a direct extraction of the attenuation factor for the measured transmission factors.

As stated in [31], ideally, the measured magnitude of the transmission factor S_{21} is directly related to the attenuation factor α through the relation:

$$(19) \quad |S_{21}| = e^{-\alpha l} \quad \text{where } l \text{ is the transmission line length.}$$

However, the microstrip transmission lines are not directly measurable because a CPW-to-microstrip line transition is required to access the device under test with the VNA. The transition is not perfect and has its own response, which introduces a mismatch. In addition, a reflection due to the mismatch between the VNA internal impedance and the circuit exists, corrupting the measurement. The mismatch due to the transition is de-embedded with the help of the TRL calibration. The mismatch due to the impedance difference between the VNA and the line can be calibrated out from the measurement. The method to extract the transmission factor of the line from the measured S-parameters is described in [31]. The measured reflection and transmission coefficients (R and T , respectively) are expressed by [31]:

$$(20) \quad R = \frac{\Gamma_1(1 - e^{-2\gamma l})}{1 - \Gamma_1^2 e^{-2\gamma l}}$$

$$(21) \quad T = \frac{(1 - \Gamma_1^2)e^{-\gamma l}}{1 - \Gamma_1^2 e^{-2\gamma l}}$$

where Γ_1 is the reflection coefficient due to the mismatch between the impedances of the VNA and the circuits under test. This system of two equations and two unknowns is re-formulated as a polynomial equation of order 6:

$$(22) \quad TX^6 - (1 + T^2 - R^2)X^5 - TX^4 + 2(1 + T^2 - R^2)X^3 - TX^2 - (1 + T^2 - R^2)X + T = 0$$

where $X = e^{-\gamma l}$ is the parameter. A Matlab program was written to extract the roots of this equation and to select the one that corresponds to the attenuation factor.

Several transmission lines are considered for this study. The line lengths are a quarter of a wavelength, a full wavelength and three wavelengths, respectively (the wavelength corresponds to the 44 GHz centre frequency). The measured S-parameters are plotted in Figure 35, along with the simulation results for three-wavelength and one-wavelength transmission lines. The graph showing the reflection coefficients indicates that the circuits are not ideally matched, particularly for the longest transmission line. The multiple reflections between the two ports due to the mismatch between the impedances of the VNA and the circuits under test are clearly visible, generating periodic maxima and minima.

Figure 35a

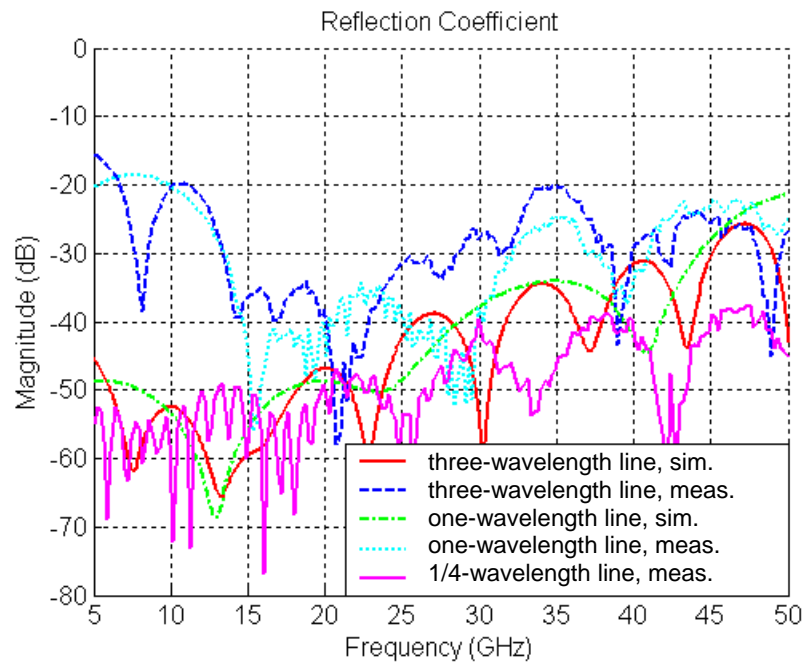


Figure 35b

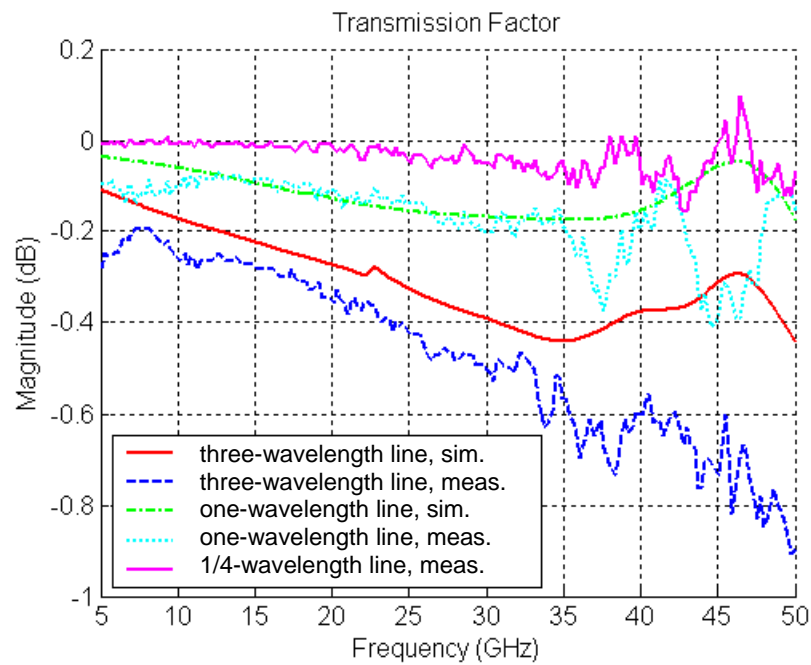


Figure 35. Measured and simulated *S*-parameters of transmission lines of various lengths

The transmission factors plotted in Figure 35b show the increase of the insertion loss with frequency and line length. One can notice that a calibration problem existed when measuring the quarter wavelength line, as the transmission factor is positive around 38 GHz and 46 GHz.

Also, the simulated and measured results for the one-wavelength line overlaps between 10 GHz and 35 GHz, whereas the measured insertion loss for the three-wavelength line is higher than the simulation indicates.

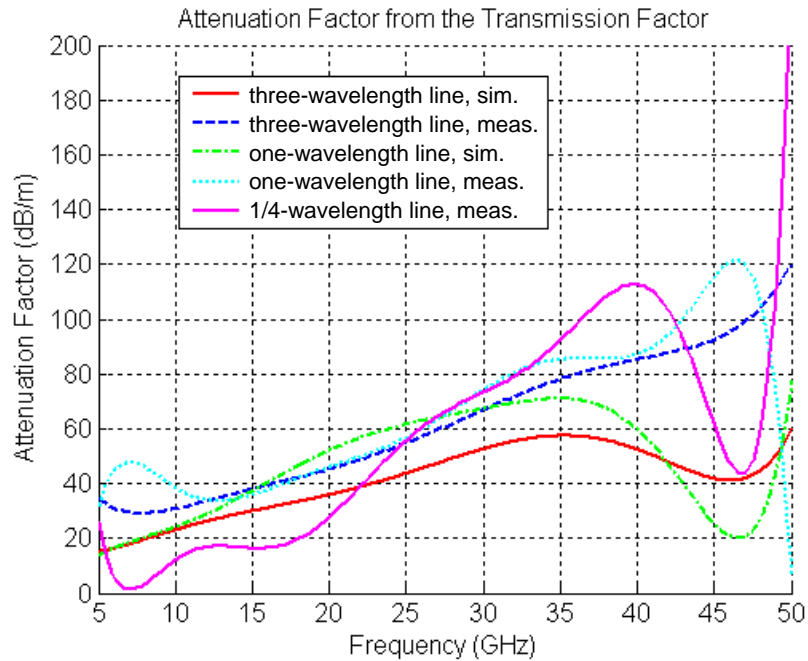


Figure 36. Attenuation factor obtained from transmission factor measurement

The attenuation factor is first extracted directly from the transmission factor measurement without correcting the data for the mismatch. The result is shown in Figure 36 for the three measured lines and the two simulated lines. In this graph, a curve-fitting technique with a polynomial function of order 8 has been used for smoothing the data before extracting the attenuation coefficients. The longer line exhibits a smoother variation with frequency. The measured one-wavelength line shows similar variation. However, the results obtained with the shortest line do not seem reliable, probably because the line is too short [31]. The attenuation rises faster with frequency than the other lines, and an unexpected drop occurs around 47 GHz. Note that a similar drop is noticeable with the simulation results, but it is less pronounced with the three-wavelength transmission line.

Figure 37 presents the attenuation factor estimated using the absolute magnitude method as a function of frequency. The results obtained for all the frequency points are plotted along with the corresponding curve-fitted responses. The results from the quarter-wavelength line show large fluctuations, particularly at high frequency. The average curve exhibits a lower attenuation factor at low frequency compared to the attenuation factor obtained with the other lines, and rises faster afterward. The measured results for the one wavelength line have large fluctuations at high frequency. However, the average attenuation agrees quite well with the corresponding simulation results from 5 GHz to 35 GHz. Note that this was also the case for the attenuation factor deduced directly from the transmission factor

(see Figure 36). The attenuation factor obtained with the measurement of the three-wavelength line presents little fluctuation. The corresponding curve-fitted curve is superimposed with the attenuation factor deduced directly from the measured transmission without mismatch correction. Note that the difference between the attenuation factors calculated directly from the transmission factor (Figure 36), and the attenuation factor obtained with the absolute magnitude method (Figure 37) is not important, particularly at low frequency.

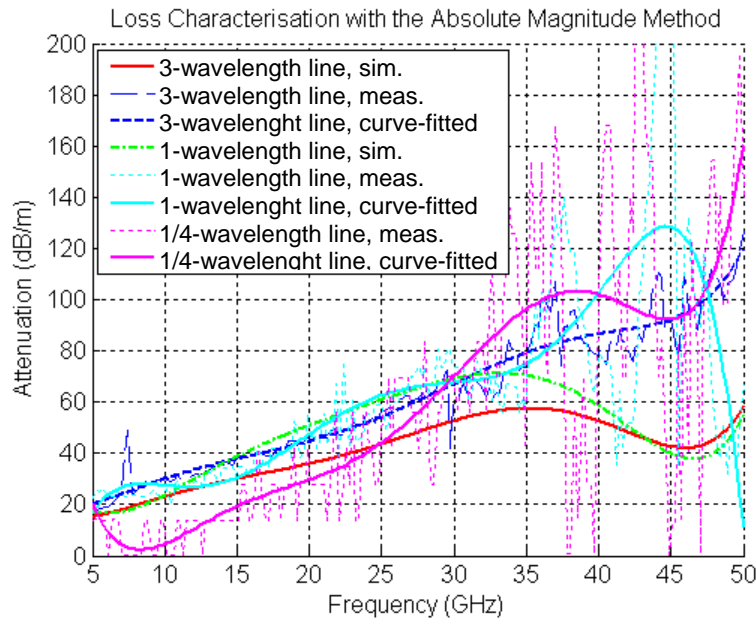


Figure 37. Attenuation factor obtained with the absolute magnitude method

The attenuation factor obtained with the line comparison method from measured and simulated data are shown in Figure 38. The mismatch correction is applied on the transmission factors before extracting the attenuation factor from the difference between the insertion losses of two transmission lines of different lengths. Two curves obtained with measured data are plotted, corresponding to line length differences of 2.0 wavelengths (at 44.5 GHz) and 2.75 wavelengths. The response obtained with the simulated data corresponds to a line length difference of 2.0 wavelengths. As seen previously, the attenuation deduced from the measurement is on the order of the attenuation deduced from the simulated data at 10 GHz, and is larger for higher frequencies. The two curves obtained from measured data are superimposed. Their fluctuations are small below 30 GHz, and increase slightly above this frequency. These two comments indicate that the line comparison method is more reliable than the previous methods based on the measurement of straight transmission lines. The variation of the curve-fitted responses is very linear: A straight line going through the point (10 GHz, 30 dB/m) and (45 GHz, 100 dB/m) would be a good representation of the attenuation as a function of frequency. The attenuation factor obtained with the ring resonator method is also indicated in Figure 38 for comparison. The results obtained with these two methods match almost perfectly, except for the attenuation factor obtained at 43 GHz. Our measurements seem reliable from 10 GHz to 40 GHz only.

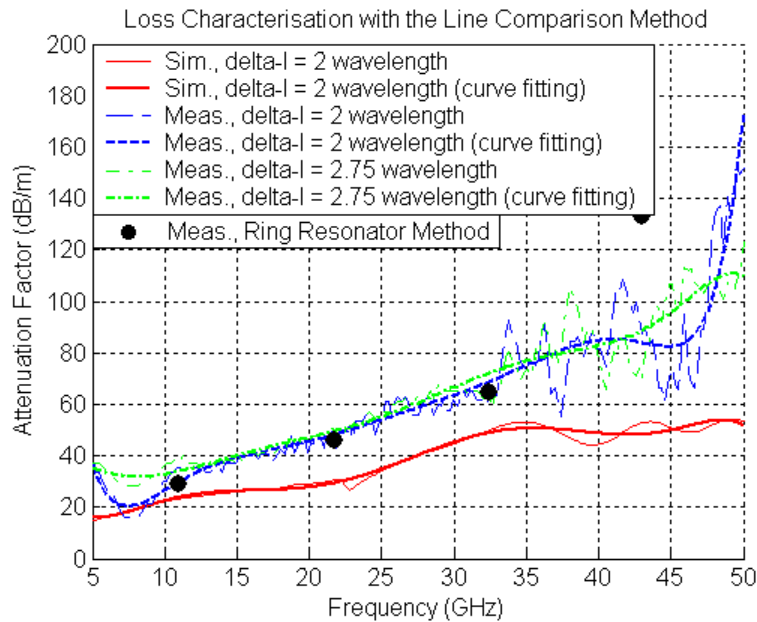


Figure 38. Attenuation factor obtained with the line comparison method

6.2.4 Conclusions

The dielectric constant of the LTCC material and the attenuation factor of a buried microstrip transmission line have been characterized experimentally using different methods. The dielectric constant obtained with the ring resonator method varies from 7.2 to 7.5 in the 10 to 45 GHz frequency range. This value is slightly higher than the value indicated by DuPont (7.1), but smaller than the measured result provided by J. Bray [31] (7.55). The attenuation factor of the microstrip transmission line buried in the LTCC substrate have been satisfactorily characterized with the ring resonator method and the line comparison method. The results are higher than those obtained by other researchers. However, in our case, the attenuation factor contains losses due to surface wave propagation, which starts to be non-negligible above 10 GHz, according to [17].

6.3 Input impedance of the Yagi-like antennas

This section reports the input impedance measurements of the four Yagi-like antennas realized on three different wafers. Each wafer contains four antennas located at different distances from the substrate edge. Antenna #1 is the antenna whose director is the closest to the substrate edge (1.2 mm) and antenna #4 is the antenna whose director is the farthest for the substrate edge (1.5 mm). For the measurements on wafer #1, the antennas have been physically separated from each other to remove the uncertainty of inter-element interaction effects that can perturb the measurement (direct coupling measurement can not be performed with the measurement system). The results for antenna #1 for all the wafers are presented in Figure 39. Figure 40 shows the measurement of the input impedance of the four antennas realized on wafer #1. And finally, the simulated input impedances of the four antennas are

given in Figure 41 for comparison purposes. All the measurement results for antennas #2, #3 and #4 are reported in Appendix 9. The characteristics are summarized in terms of operating frequency and bandwidth in Table 16 to Table 19 in Appendix 9.

All the measured input impedance performed with Yagi-like antenna #1 realized on different wafers and at different periods are given in Figure 39. The measurements were done with the TRL calibration. The measurements carried out in June 2003 are wideband measurement with a 450 MHz step while the other measurements are narrow band measurements with a 50 MHz step. We can notice that the results are different, but similar. Considering all of the data, the minimum reflexion coefficient (RC) varies from -11.35 dB to -8.6 dB and the frequency where the minimum RC occurs varies from 45 GHz to 46.4 GHz. Looking only at the measurement of antenna #1 on wafer #1, the minimum RC fluctuates between -10.4 dB and -8.6 dB, and the frequency where the minimum RC occurs fluctuates from 45.05 GHz to 46.4 GHz. If we consider only the measurement obtained in October 2003, the minimum RC difference is only 0.1 dB and the frequency difference is 1.3 GHz. The same kind of comments can be made about the measurements of the other antennas (see Appendix 9). As these measurements illustrate, it is not easy to perform reliable measurement at 45 GHz. The discrepancies come from various factors. As mentioned previously, several months separate the different measurement campaigns, and as the circuits were not stored in an hermetic environment, oxydation appeared on the microstrip line. Therefore, the contact of the probe on the circuits is not perfect and this can alter the measurements. Also, the contact between the probe tips and the microstrip line and pads can not be made exactly at the same location for all the circuits. Neither can the TRL calibration be the same from one measurement to another. So, these measurements give a general trend of the input impedance, but no accurate values can really be extracted. Nevertheless, correct comparison between the results of the four antennas realized on the same wafer and using the same calibration setup can be made.

Figure 40 presents the input impedances of antenna #1 to antenna #4 realized on wafer #2 and measured in October 2003. Differences between the antenna responses are noticeable. Looking at the input impedance on the Smith chart (SC), antenna #1's response exhibits the largest loop around the SC centre while antennas #3 and #4 exhibit the smallest loops. Antenna #3, located 1.4 mm from the substrate edge shows the best match and antenna #4 shows the widest -10 dB-RC bandwidth (43.8 GHz to 46.9 GHz).

The measured results can be compared to the simulated results shown in Figure 41. Antenna #2 located 1.3 mm away from the substrate edge exhibits the best matching and the widest impedance bandwidth (35.8 GHz to 46.95 GHz). The difference between the antenna responses is also visible. However, the simulated results do not agree with the measurements. In the Smith chart representation, antenna #1 (placed 1.2 mm away from the substrate edge) generates the smallest loop, and the loop increases in size when the antenna moves away from the substrate edge. The effect of moving the antenna away from the substrate edge observed by simulation is the opposite to the effect observed with the measurements. This could be due to an incorrect distance between the director of the Yagi-like antenna and the substrate edge (L_{sub}). As a matter of fact, as reported in Appendix 2, the size of the loop decreases when the antenna moves closer to the substrate edge. The loop reaches a minimum size for a specific distance and then increases in size when the antenna gets closer. However, the distance between the cavity's edge and the substrate edge was measured, and the deduced distance L_{sub} is exactly the distance considered for the design. The same phenomena is observed with the antennas measured on wafer #2 and wafer #3. This could be due to the fact that the measured

microstrip line widths are different than the ones specified for the design. As a result the characteristic impedances of the lines are not the expected ones. This can produce a significant input impedance variation, particularly with these circuits where several quarter-wavelength transformers are used.

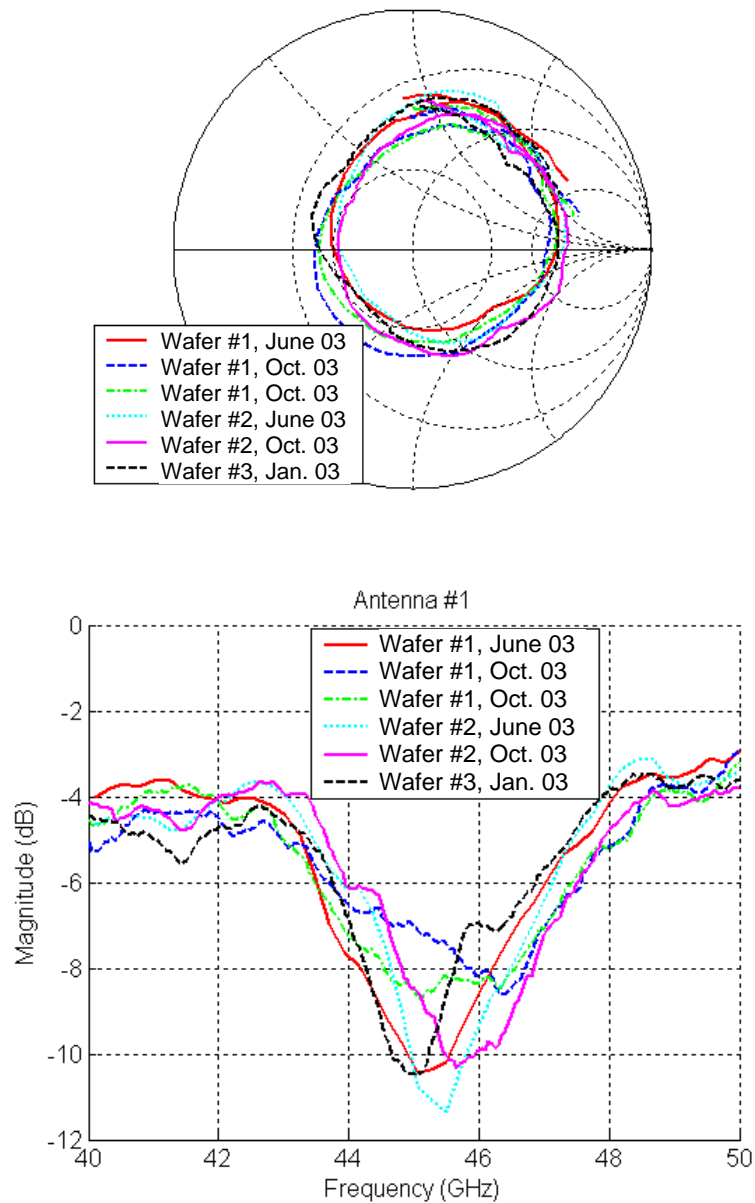


Figure 39. Input impedance of antenna #1 measured on all wafers with different TRL calibrations

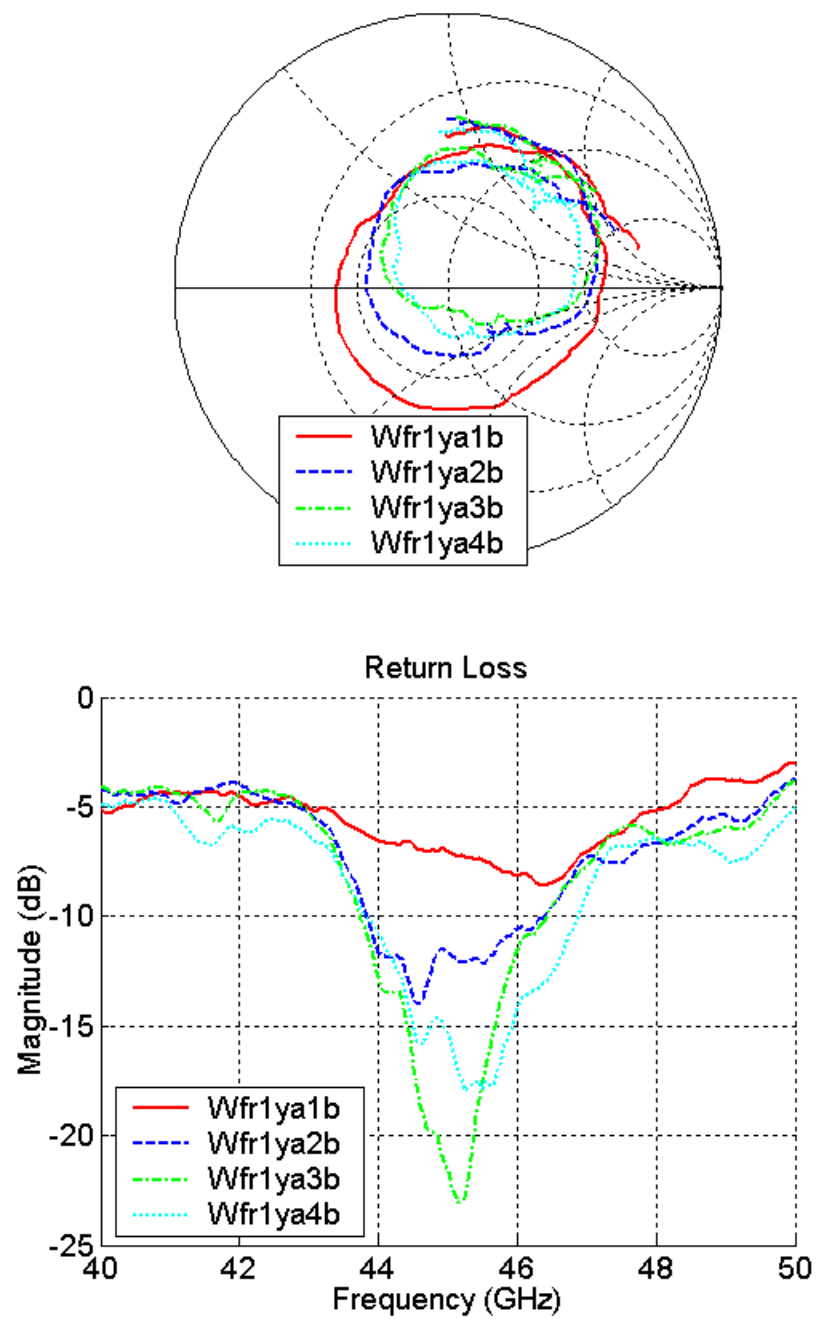


Figure 40. Measured input impedance of all antennas on Wafer #1

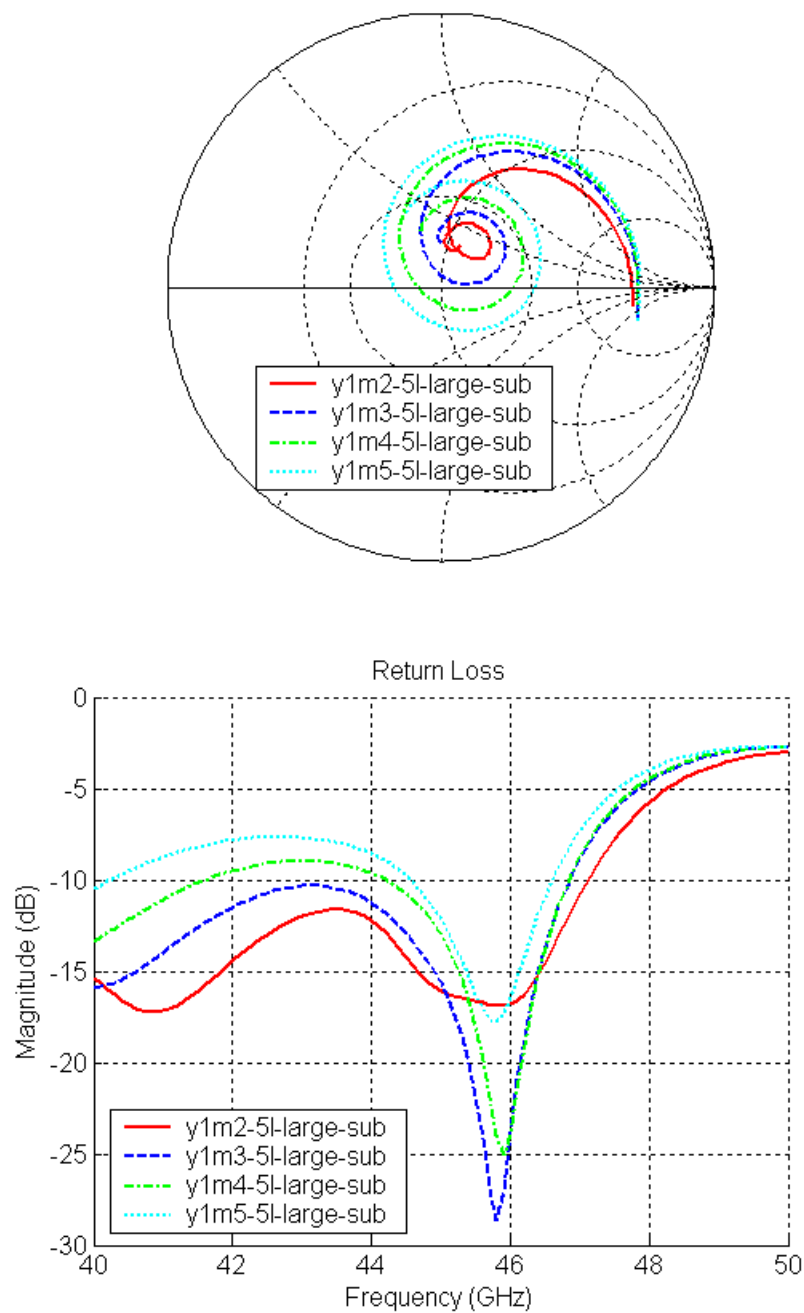


Figure 41. Simulated input impedance of the Yagi-like antennas

However, overall, the centre frequency of the measured antennas are close to the centre frequency predicted by simulation, and the impedance bandwidths are comparable.

7. Summary

A Yagi-like antenna element buried in LTCC material has been design for AEHF communication systems. This endfire antenna is suitable as a radiating element for an array using a brick architecture. The different components of the antenna have been fully characterized using a full-wave simulation tool based on the finite element method. The antenna has been optimized for operation in the upper frequency band of the AEHF communication spectrum (43.5-45.5 GHz), taking into account the constraints introduced by the LTCC process. Several prototypes were fabricated. The measurements agree relatively well with the simulation results in terms of resonant frequency and impedance bandwidth. The prototype having the best design exhibits a 5 GHz impedance bandwidth. The next step is to study the behaviour of this particular radiating element in an array configuration, leading to the realization of a compact and low cost phased array with a brick architecture in LTCC technology.

Some circuits were also designed for extracting the properties of the LTCC material, as no information exists for frequencies above 40 GHz. Two resonant circuits, a ring resonator and a T-junction, were used to estimate the dielectric constant and the attenuation factor of the LTCC material as well as microstrip transmission lines. The dielectric constant obtained using the ring resonator method varies from 7.2 to 7.5 in the 10-45 GHz frequency range. This value is slightly higher than the value indicated by DuPont (7.1), but smaller than the measured result provided by J. Bray [31] (7.55). The attenuation factor of the microstrip transmission line buried in the LTCC substrate has been satisfactorily characterized with the ring resonator method and the line comparison method. The results are higher than the results obtained by other researchers. However, in our case, the attenuation factor contains additional losses due to surface wave propagation becoming non-negligible from 10 GHz.

As part of this project, the LTCC fabrication process has also been evaluated. Going through all the different steps provides us with very useful information for designing other circuits in the future with the LTCC technology.

8. References

- [1] J. A. Kinzel, B. J. Edward and D. Rees, "V-band, Spaced-Based Phased Arrays", Microwave Journal, Jan. 1987, pp 89-102.
- [2] B. Geller, B. Thaller, A. Fathy, M. J. Liberatore, H. D. Chen, G. Ayers, V. Pendrick and Y. Narayan, "LTCC-M: an Enabling Technology for High Performance Multilayer RF Systems", Microwave Journal, Vol. 42, No. 7, July 1999, pp 64-72.
- [3] D. Sturzebecher, J. Leen, R. Cadotte, J. DeMarco, T-D. Ni, T. Higgins, M. Popick, M. Cummings, B. VanMeerbeke, T. Provencher, B. Kimble, K. Shalkhauser, R. Simons, "20 GHz LTCC Phased Array Module", IEEE MTT International Symposium, 1996, Vol. 2, pp 991-994.
- [4] DuPont Microcircuit Materials, "DuPont Green Tape Design and Layout Guideline, 1998, www.DuPont.com/mcm.
- [5] Ferro Electronic Materials, <http://www.ferro.com>.
- [6] Heraeus, Circuit Material Division, <http://www.4cmd.com/circuitmaterials>.
- [7] Northrop Grumman, Advanced Ceramics Facility, <http://sensor.northgrum.com/esss/lccc/lccc.htm>
- [8] Electro-Science Laboratories, <http://electroscience.com>.
- [9] VTT Electronics, Finland, <http://www.vtt.fi>
- [10] J. Litzenberger, M. Clénet, G. A. Morin and Y. M. M. Antar, "Study of a Waveguide Antenna Implemented in Laminated Material", Technical Report DRDC Ottawa TR2002-132, Dec. 2002.
- [11] R. J. Mailloux, "Phased Array Antenna Handbook", Artech House, 1994.
- [12] H. Yagi, "Beam Transmission of the Ultra Short Waves", Proceedings of IRE, Vol. 16, June 1928, pp 715-741.
- [13] N. Kaneda, Y. Qian, T. Itoh, "A Broad-band Microstrip-to-Waveguide Transition Using Quasi-Yagi Antenna", IEEE transactions on Microwave Theory and Techniques, Vol. 47, No. 12, December 1999, pp 2562-2567.
- [14] W. R. Deal, N. Kaneda, J. Sor, Y. Qian, T. Itoh, "A New Quasi-Yagi Antenna for Planar Active Antenna Arrays", IEEE Trans. on Microwave Theory and Techniques, Vol. 48, No 6, June 2000, pp 910-918.
- [15] IE3D, version 8, Zeland Software Inc., Fremond, California, USA, <http://www.zeland.com>
- [16] HFSS version 7 and version 8, Ansoft Corporation, Pittsburg, PA, <http://www.ansoft.com>.
- [17] R. Garg, P. Bhartia, I. Bahl and A. Ittipiboon, "Microstrip Antenna Design Handbook", Artech House, 2001.

- [18] S. S. Zhong, G. Liu and G. Qasim, "Closed Form Expressions for Resonant Frequency of Rectangular Patch Antennas with Multidielectric Layers", IEEE Antennas and Propagation, Vol AP-42, No 9, Sept. 1994, pp 1360-1363.
- [19] D. M. Pozar, "Microwave engineering", Addison-Wesley Publishing, 1990.
- [20] Y. Qian, T. Itoh, "A Broadband Uniplanar Microstrip-to-CPS Transition", 1997 Asia-Pacific Conference, pp 609-612.
- [21] C. A. Balanis: "Antenna Theory: Analysis and Design", Chap. 10, Wiley, 2nd edition, 1997.
- [22] K. C. Gupta, R. Garg and I. J. Bahl, "Microstrip Lines and Slotlines", Artech House, 1979.
- [23] J. R. James and P. S. Hall, editors, "The Handbook of Microstrip Antennas", Peter Peregrinus, 1989.
- [24] T. C. Edwards, "Foundations for Microstrip Circuit Design", John Wiley and Sons, 1985.
- [25] B. C. Wadell, "Transmission Line Design Handbook", Artech House, 1991.
- [26] J. R. Bray and L. Roy, "Microwave Characterization of a Microstrip Line Using a Two-Port Ring Resonator with an Improved Lumped-Element Model", IEEE Trans. on Microwave Theory and Techniques, Vol. 51, No. 5, May 2003, pp 1540-1547.
- [27] R. A. Pucel, D. J. Massé and C. P. Hartwig, "Losses in Microstrip", IEEE Trans. on Microwave Theory and Techniques, Vol. MTT-16, June 1968, pp 342-350. See also 'Correction to "Losses in Microstrip"' in IEEE MTT-16, December 1968, p 1064.
- [28] J. F. Zücher and F. E. Gardiol, "Broadband Patch Antennas", Artech House, 1995.
- [29] R. Kulke, W. Simon, A. Lauer, M. Rittweger, P. Waldow, S. Stringfellow, R. Powell, M. Harrison and J-P. Bertinet: "Investigation of Ring Resonators on Multilayer LTCC, presented at the IEEE MTT Int. Microwave Symposium Workshop, Phoenix, AZ, 20-25 May 2001.
- [30] C-C. Yu and K. Chang: "Transmission-Line Analysis of a Capacitively Coupled Microstrip-Ring Resonator", IEEE Microwave Theory and Techniques, Vol. 45, No 11, November 1997, pp 2018-2024.
- [31] J. R. Bray, "Millimetre-Wave Ferrite-Loaded Laminated Waveguide Phase Shifters Embedded in Low Temperature Cofired Ceramic", PhD. Dissertation, Ottawa-Carleton Institute For Electrical Engineering, Ottawa, Ontario, September 2003.
- [32] D. I. Amey, M. Y. Keating, M. A. Smith, S. J. Horowitz, P. C. Donahue, C. R. Needes, "Low Loss Tape Materials System for 10 to 40 GHz Application", 2000 Int. Symp. On Microelectronics (IMAPS 2000).
- [33] D. I. Amey, S. J. Horowitz, "Characterization of Low Loss Materials at 40 GHz", 1999 Int. Symp. On Microelectronics (IMAPS 1999).
- [34] DuPont Microcircuit Materials, "Characterization of Low Loss LTCC Materials at 40GHz", Microwave Journal, Vol. 44, No 2, February 2001, pp 186-190.
- [35] P. C. Donohue, B. E. Taylor, D. I. Amey, R. R. Draudt, M. A. Smith, S. J. Horowitz and J. R. Larry, "A New Low Loss Lead Free LTCC System for Wireless and RF

Applications”, 1998 International Conference on Multichip Modules and High Density Packaging, Denver, CO, 15-17 April 1998, pp 196-199.

Appendices

Appendix 1. LTCC technology.....	55
Appendix 2. Parametric study of the Yagi-like antenna	56
Appendix 3. Calculation of the scattering matrix coefficients of a microstrip transmission line loaded with an open stub	58
Appendix 4. Drawings of the different circuits	61
Appendix 5. Pictures of the launcher	64
Appendix 6. List of the measurement files.....	65
Appendix 7. Graphs of the S12 response of the two-ports circuits realized on the three different wafers	68
Appendix 8. Loss characterisation using transmission line measurement.....	75
Appendix 9. Input impedance of the Yagi-like antennas.....	77

Appendix 1. LTCC technology

Table 8. LTCC manufacturers and processes

Manufacturers	Nationality	Processes					
		DuPont 951	DuPont 943	Ferro A6	Heraeus CT700	Heraeus CT2000	Sarnoff
VTT Electronics	FI	X	X	x			
IMST	DE	X					
Thales Microwave	FR	X	x	X	x	x	
Via-Electronic	DE	X					
National Semiconductor	USA	X	X	X			
C-MAC - Scrantom	CA-USA ¹	X	X	X	X	X	
Dielectric Laboratories	USA						X*

X: manufacturing, x: prototyping, X*: LTCC-M

¹ LTCC facilities belong to Scrantom, a company based in California. Scrantom is owned by C-Mac, whose headquarter is in Montreal (data collected in 2001).

Table 9. LTCC Process characteristics

	VTT Electronics	IMST	National Semiconductor	C-MAC Scantom	Via-Electronic	Thales
Line width/spacing	200 (100 for prototyping)	130	50	75	100 /50	125
Width tolerance				+/- 12.5		+/- 25
Via diameter	150	150	90	100	100	125
Via pad	250	150-300	132	150	150	150
Min. thickness	4 layers	2-4 layers	2-4 layers	3 layers	100	
Max thickness		unlimited			2.3 mm	24 layers
Max. part size	4.5"x4.5"	3.5"x3.5"	5"x5"	6"x6"	6.8"x6.8"	4.5"x4.5"
Resistor tolerances (on Top/buried)	N/A	?	+/- 30% (1% trimmed) / +/- 30%	10% to 50% (buried)	1% trimmed (on top)	+/- 30% (5% trimmed)/ +/- 50%
Capacitor tolerance	N/A		(+/-) 20% special tape	10% special tape	A	
Inductor	N/A			A		
Ball Grid Array			A		A	A

Dimensions are in microns unless specified. A: Available, N/A: Non-Available, ?: missing information.

Appendix 2. Parametric study of the Yagi-like antenna

The parametric study is carried out with the antenna dimensions given in section 2.6. For this study, the antenna considered is realized on a 6-layer substrate (3 layers below and above the antenna).

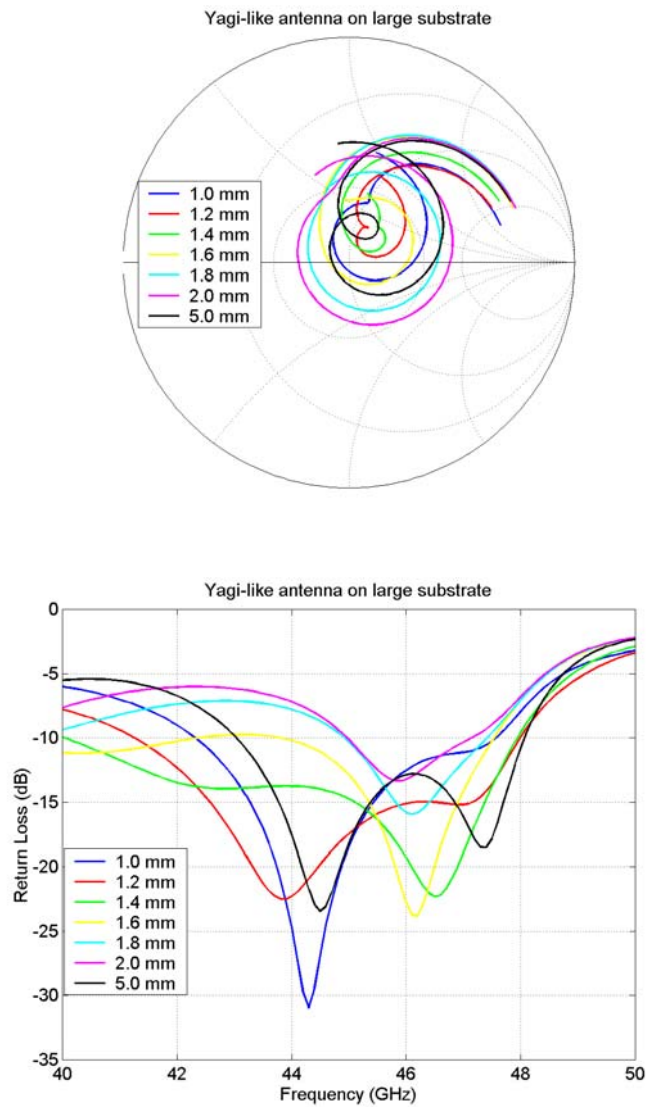


Figure 42. Input impedance response of the Yagi-like antenna as a function of the distance between the director and the substrate's edge

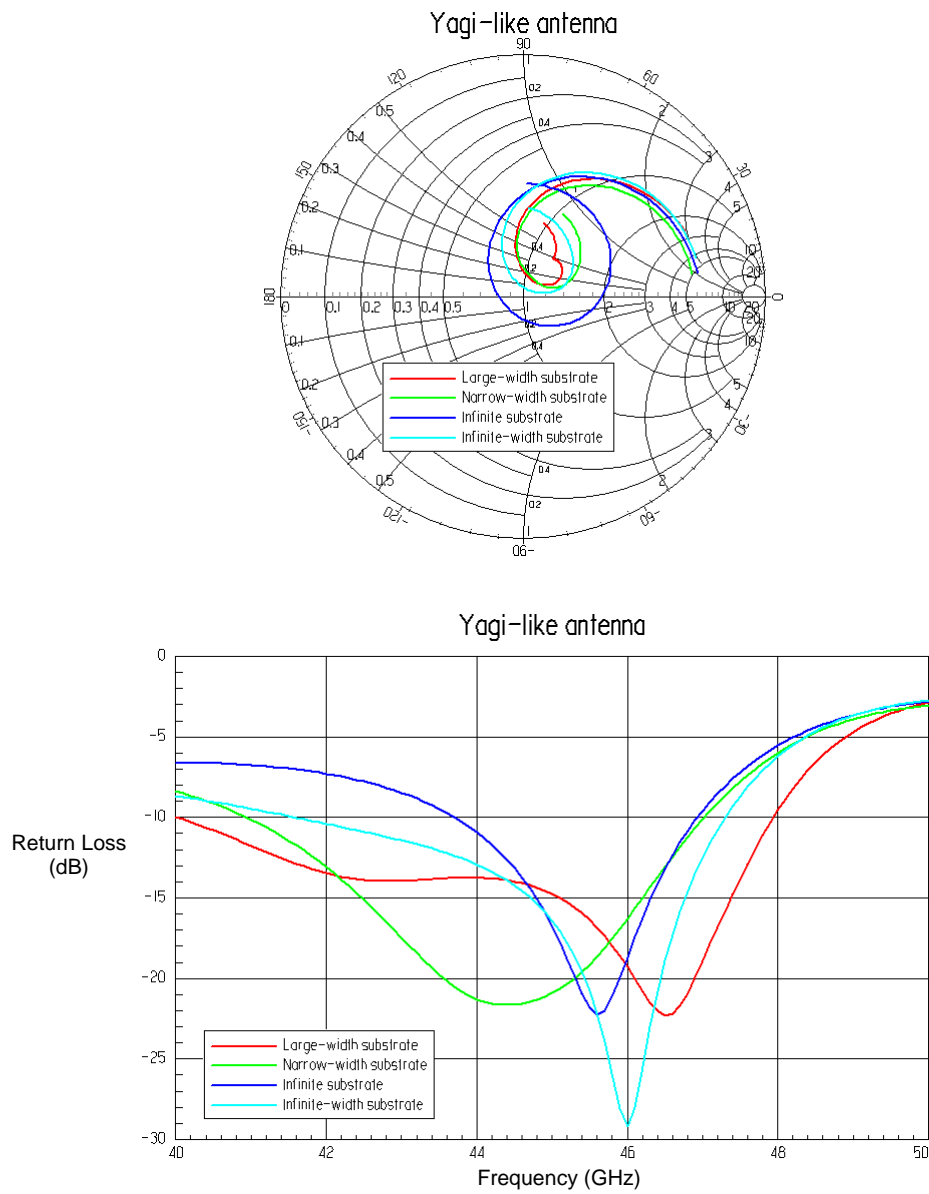


Figure 43. Input impedance of the Yagi-like antenna on substrates of different dimensions

Appendix 3. Calculation of the scattering matrix coefficients of a microstrip transmission line loaded with an open stub

The microstrip transmission line loaded with an open stub circuit can be represented by the schematic shown in Figure 44.

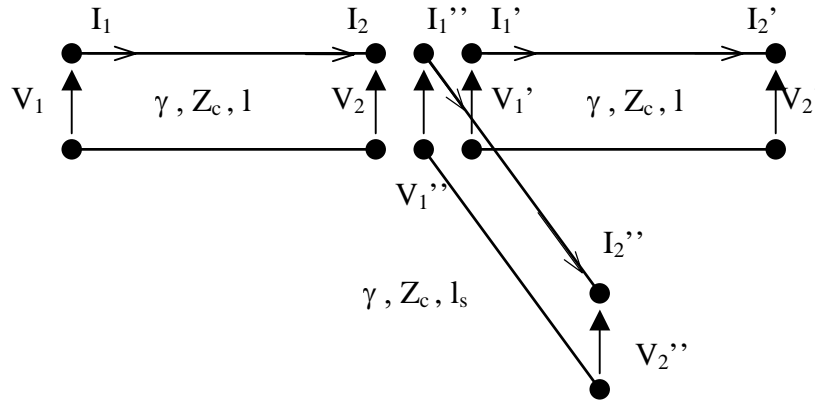


Figure 44. Representation of a microstrip transmission line loaded with an open stub

The transmission matrix for a transmission line is

$$(23) \quad \begin{bmatrix} V_1 \\ I_1 \end{bmatrix} = \begin{bmatrix} A & B \\ C & D \end{bmatrix} \begin{bmatrix} V_2 \\ I_2 \end{bmatrix} = \begin{bmatrix} ch\gamma l & Z_c sh\gamma l \\ \frac{1}{Z_c} sh\gamma l & ch\gamma l \end{bmatrix} \begin{bmatrix} V_2 \\ I_2 \end{bmatrix}.$$

As the length of the line on both side of the open stub are the same, we also have

$$(24) \quad \begin{bmatrix} V_1' \\ I_1' \end{bmatrix} = \begin{bmatrix} A & B \\ C & D \end{bmatrix} \begin{bmatrix} V_2' \\ I_2' \end{bmatrix} = \begin{bmatrix} ch\gamma l & Z_c sh\gamma l \\ \frac{1}{Z_c} sh\gamma l & ch\gamma l \end{bmatrix} \begin{bmatrix} V_2' \\ I_2' \end{bmatrix},$$

and, for the open stub,

$$(25) \quad \begin{bmatrix} V_1'' \\ I_1'' \end{bmatrix} = \begin{bmatrix} As & Bs \\ Cs & Ds \end{bmatrix} \begin{bmatrix} V_2'' \\ I_2'' \end{bmatrix} = \begin{bmatrix} ch\gamma_s & Z_c sh\gamma_s \\ \frac{1}{Z_c} sh\gamma_s & ch\gamma_s \end{bmatrix} \begin{bmatrix} V_2'' \\ I_2'' \end{bmatrix}.$$

We also have the following relationships between the currents and the voltages:

$$(26) \quad \begin{cases} V_2 = V_1' = V_1'' \\ I_2 = I_1' + I_1'' \end{cases}.$$

Knowing that $I_2''=0$, from equation (25) it comes $\begin{cases} V_1'' = As V_2'' \\ I_1'' = Cs V_2'' \end{cases}$, resulting in

$$(27) \quad I_1'' = \frac{Cs}{As} V_1'' = \frac{Cs}{As} V_1' = \frac{Cs}{As} (AV_2' + BI_2').$$

Using the current relationship, equation (23) becomes

$$(28) \quad \begin{cases} V_1 = AV_1' + B(I_1' + I_1'') \\ I_1 = CV_1' + D(I_1' + I_1'') \end{cases}.$$

Thus, inserting equations (24) and (27) in (28), we obtain

$$(29) \quad \begin{cases} V_1 = A(AV_2' + BI_2') + B \left[CV_2' + DI_2' + \frac{Cs}{As} (AV_2' + BI_2') \right] \\ I_1 = C(AV_2' + BI_2') + D \left[CV_2' + DI_2' + \frac{Cs}{As} (AV_2' + BI_2') \right] \end{cases}.$$

Finally, the transmission matrix of the complete circuit is

$$(30) \quad \begin{bmatrix} V_1 \\ I_1 \end{bmatrix} = \begin{bmatrix} A^2 + BC + AB \frac{Cs}{As} & B(A + D) + B^2 \frac{Cs}{As} \\ C(A + D) + AD \frac{Cs}{As} & BC + D^2 + BD \frac{Cs}{As} \end{bmatrix} \begin{bmatrix} V_2' \\ I_2' \end{bmatrix} = \begin{bmatrix} A_T & B_T \\ C_T & D_T \end{bmatrix} \begin{bmatrix} V_2' \\ I_2' \end{bmatrix}$$

Knowing that $A = D$ and $A^2 - BC = 1$, the final transmission matrix implies to

$$(31) \quad \begin{bmatrix} A_T & B_T \\ C_T & D_T \end{bmatrix} = \begin{bmatrix} A^2 + BC + AB \frac{Cs}{As} & 2AB + B^2 \frac{Cs}{As} \\ 2AC + AD \frac{Cs}{As} & A^2 + BC + AB \frac{Cs}{As} \end{bmatrix}$$

The relationships between the S_{11} and S_{21} coefficients of the scattering matrix and the transmission matrix coefficients are [19]

$$(32) \quad S_{11} = \frac{A_T + B_T/Z_c - C_T Z_c - D_T}{A_T + B_T/Z_c + C_T Z_c + D_T}, \text{ and}$$

$$(33) \quad S_{21} = \frac{2}{A_T + B_T/Z_c + C_T Z_c + D_T}.$$

Inserting equation (31) in equations (32) and (33), it comes

$$(34) \quad S_{11} = -\frac{th\gamma_s}{2 + th\gamma_s} e^{-2\gamma} \text{ and}$$

$$(35) \quad S_{21} = \frac{2}{2 + th\gamma_s} e^{-2\gamma}.$$

Appendix 4. Drawings of the different circuits

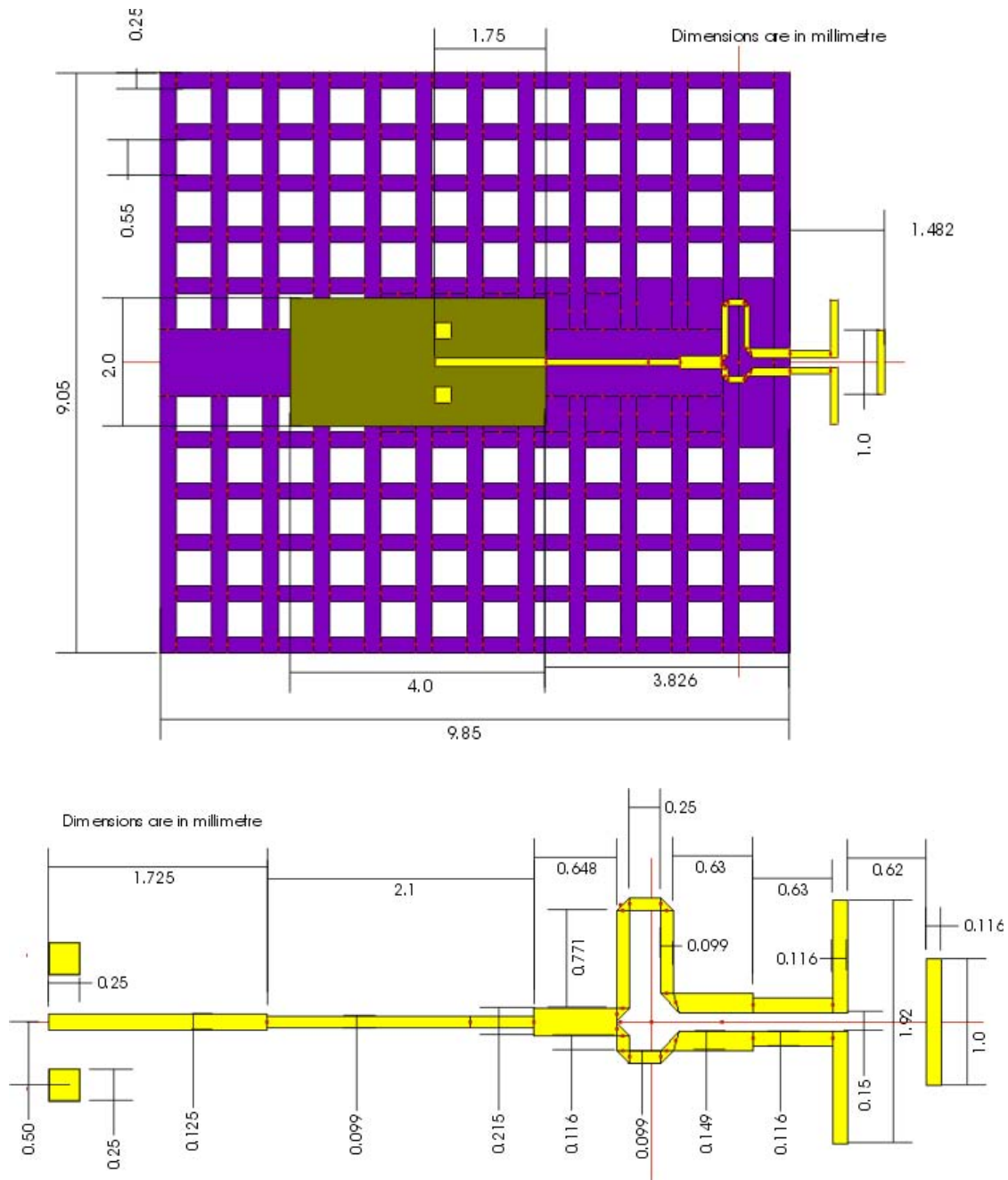


Figure 45. Drawing of the Yagi-like antenna

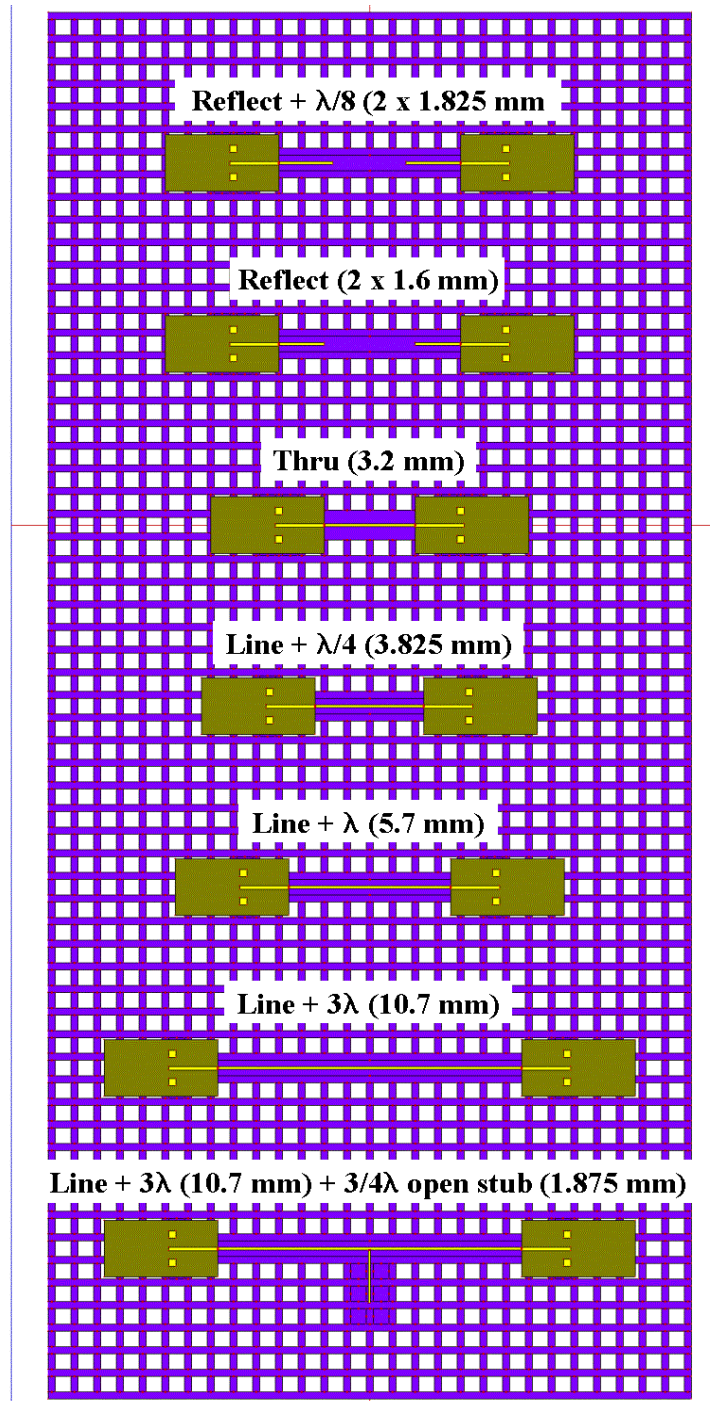


Figure 46. Drawing of the calibration lines and the open stub resonator

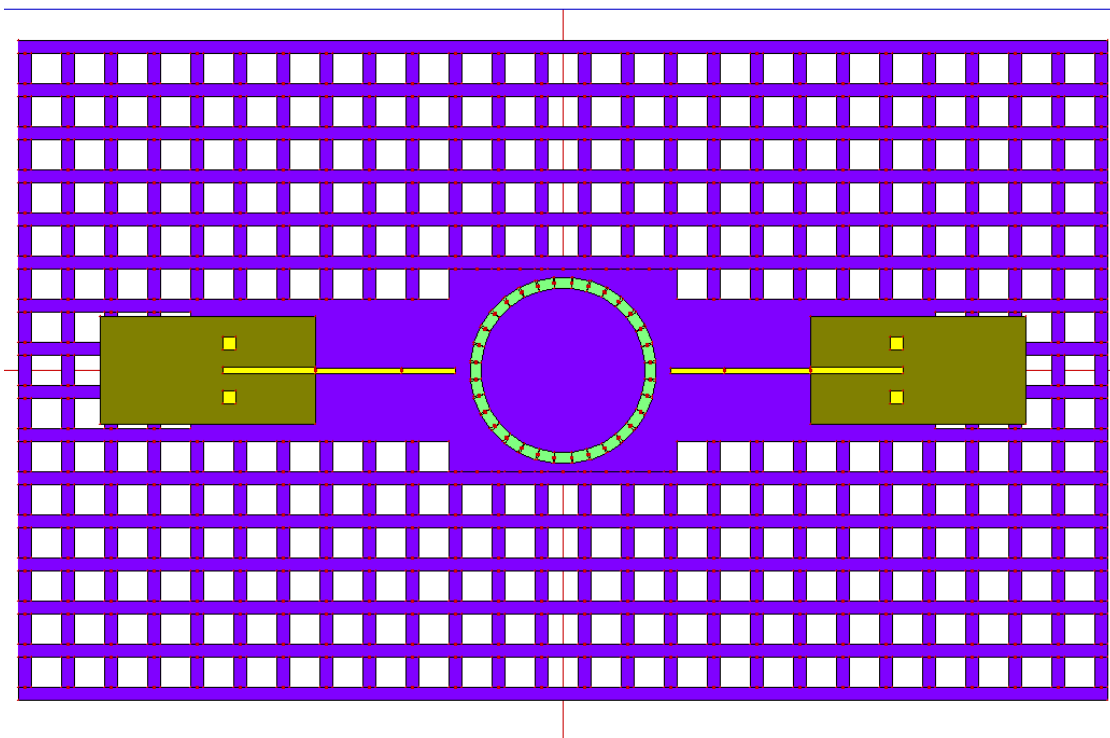


Figure 47. *Layout of the ring resonator*

Appendix 5. Pictures of the launcher



Figure 48. *Picture of the microstrip line (October 2003)*

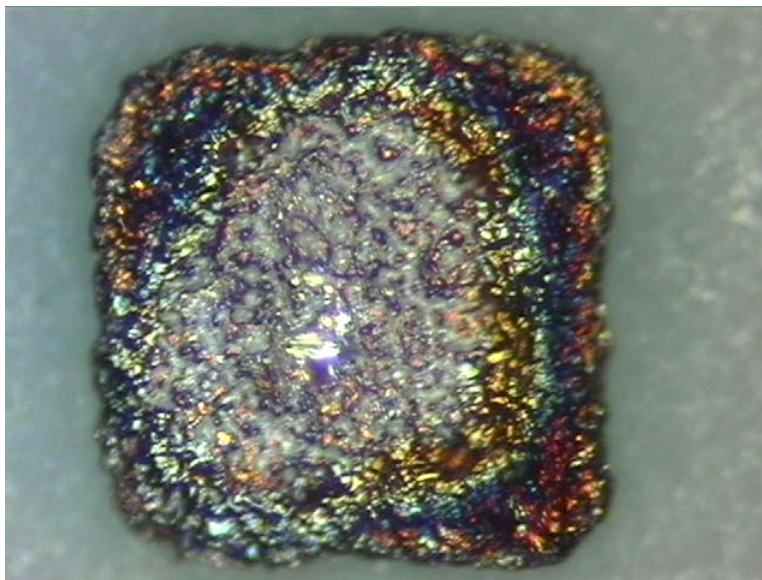


Figure 49. *Picture of a via pad connected to the ground (October 2003)*

Appendix 6. List of the measurement files

<i>Date</i>	<i>Filenames</i>	<i>Description (see Annex 4 for the drawings)</i>	<i>Calibration</i>
April 2003	Sub1_rng.s2p	Ring resonator, wafer #1	OSL (1-40 GHz)
June 2003	3LAMBDA.S2P	3λ long microstrip line (Line + 3λ), wafer #1	OSL (5-50 GHz)
June 2003	3LAMOPEN.S2P	3λ long microstrip line loaded with a $3/4\lambda$ long open stub (Line + 3λ + $3/4\lambda$ open stub), wafer #1	OSL (5-50 GHz)
June 2003	DELAY.S2P	$\lambda/4$ long delay line (Line + $\lambda/4$), wafer #1	OSL (5-50 GHz)
June 2003	LAMBDA.S2P	λ long delay line (Line + λ), wafer #1	OSL (5-50 GHz)
June 2003	OPEN.S2P	Open microstrip line wafer #1 (Reflect)	OSL (5-50 GHz)
June 2003	OPEN1_8.S2P	Open microstrip line with $\lambda/8$ long microstrip line, wafer #1 (Reflect + $\lambda/8$)	OSL (5-50 GHz)
June 2003	RESONCKT.S2P	Ring resonator feeding circuit, wafer #1	OSL (5-50 GHz)
June 2003	RINGRES.S2P	Ring resonator, wafer #1	OSL (5-50 GHz)
June 2003	THRU.S2P	Thru line, wafer #1 (Thru)	OSL (5-50 GHz)
June 2003	TR3LMDOP.S2P	3λ long microstrip line loaded with a $3/4\lambda$ long open stub (Line + 3λ + $3/4\lambda$ open stub), wafer #1	TRL (5-50 GHz)
June 2003	TRESNCKT.S2P	Ring resonator feeding circuit, wafer #1	TRL (5-50 GHz)
June 2003	TRINGRES.S2P	Ring resonator, wafer #1	TRL (5-50 GHz)
June 2003	TRL3LMDA.S2P	3λ long microstrip line (Line + 3λ), wafer #1	TRL (5-50 GHz)
June 2003	TRLAMBDA.S2P	λ long delay line (Line + λ), wafer #1	TRL (5-50 GHz)
June 2003	TRLDELAY.S2P	$\lambda/4$ long delay line (Line + $\lambda/4$), wafer #1	TRL (5-50 GHz)
June 2003	TRLOPEN.S2P	Open microstrip line wafer #1 (Reflect)	TRL (5-50 GHz)
June 2003	TRLTHRU.S2P	Thru line, wafer #1 (Thru)	TRL (5-50 GHz)
June 2003	TROPN1_8.S2P	Open microstrip line with $\lambda/8$ long microstrip line, wafer #1 (Reflect + $\lambda/8$)	TRL (5-50 GHz)
June 2003	WFR1ANT1.S2P	Antenna 1, wafer #1	TRL (5-50 GHz)
June 2003	WFR1ANT2.S2P	Antenna 2, wafer #1	TRL (5-50 GHz)
June 2003	WFR1ANT3.S2P	Antenna 3, wafer #1	TRL (5-50 GHz)
June 2003	WFR1ANT4.S2P	Antenna 4, wafer #1	TRL (5-50 GHz)
June 2003	WFR2ANT1.S2P	Antenna 1, wafer #2	TRL (5-50 GHz)
June 2003	WFR2ANT2.S2P	Antenna 2, wafer #2	TRL (5-50 GHz)
June 2003	WFR2ANT3.S2P	Antenna 3, wafer #2	TRL (5-50 GHz)
June 2003	WFR2ANT4.S2P	Antenna 4, wafer #2	TRL (5-50 GHz)

Date	Filenames	Description (see Annex 4 for the drawings)	Calibration
October 2003	3LBDA10.S2P	3 λ long microstrip line (Line + 3 λ), wafer #1	TRL (10-20 GHz)
October 2003	3LBDA30.S2P		TRL (30-40 GHz)
October 2003	3LBDA30B.S2P		TRL (30-35 GHz)
October 2003	3LBDA40.S2P		TRL (40-50 GHz)
October 2003	3LBDA40B.S2P		TRL (40-45 GHz)
October 2003	3LBDAO10.S2P	3 λ long microstrip line loaded with a 3/4 λ long open stub (Line + 3 λ + 3/4 λ open stub), wafer #1	TRL (10-20 GHz)
October 2003	3LBDAO30.S2P		TRL (30-40 GHz)
October 2003	3LBDAO3B.S2P		TRL (30-35 GHz)
October 2003	3LBDAO40.S2P		TRL (40-50 GHz)
October 2003	3LBDAO4B.S2P		TRL (40-45 GHz)
January 2004	2_3lo10.S2P	3 λ long microstrip line loaded with a 3/4 λ long open stub (Line + 3 λ + 3/4 λ open stub), wafer #2	TRL (10-20 GHz)
January 2004	2_3lo25.S2P		TRL (25-35 GHz)
January 2004	2_3lo40.S2P		TRL (40-50 GHz)
January 2004	3_3lo10.S2P	3 λ long microstrip line loaded with a 3/4 λ long open stub (Line + 3 λ + 3/4 λ open stub), wafer #3	TRL (10-20 GHz)
January 2004	3_3lo25.S2P		TRL (25-35 GHz)
January 2004	3_3lo40.S2P		TRL (40-50 GHz)
October 2003	RCKT0913.S2P	Ring resonator feeding circuit, wafer #1	TRL (9-13 GHz)
October 2003	RCKT1924.S2P		TRL (19-24 GHz)
October 2003	RCKT3035.S2P		TRL (30-35 GHz)
October 2003	RCKT4045.S2P		TRL (40-45 GHz)
October 2003	RING0913.S2P	Ring resonator, wafer #1	TRL (9-13 GHz)
October 2003	RING1924.S2P		TRL (19-24 GHz)
October 2003	RING3035.S2P		TRL (30-35 GHz)
October 2003	RING4045.S2P		TRL (40-45 GHz)
January 2004	2RNG0913.S2P	Ring resonator, wafer #2	TRL (9-13 GHz)
January 2004	2RNG1924.S2P		TRL (30-35 GHz) **
January 2004	2RNG3035.S2P		TRL (30-35 GHz)
January 2004	2RNG4045.S2P		TRL (40-45 GHz)
January 2004	3RNG0913.S2P	Ring resonator, wafer #3	TRL (9-13 GHz)
January 2004	3RNG1924.S2P		TRL (19-24 GHz)
January 2004	3RNG3035.S2P		TRL (30-35 GHz)
January 2004	3RNG4045.S2P		TRL (40-45 GHz)

** Data saved with the wrong filename

Date	Filenames	Description (see Annex 4 for the drawings)	Calibration
October 2003	WFR1YA1A.S2P	Antenna 1, wafer #1	TRL (30-40 GHz)
October 2003	WFR1YA1B.S2P	Antenna 1, wafer #1	TRL (40-50 GHz)
October 2003	WFR1YA1C.S2P	Antenna 1, wafer #1	TRL (40-50 GHz)*
October 2003	WFR1YA2A.S2P	Antenna 2, wafer #1	TRL (30-40 GHz)
October 2003	WFR1YA2B.S2P	Antenna 2, wafer #1	TRL (40-50 GHz)
October 2003	WFR1YA2C.S2P	Antenna 2, wafer #1	TRL (40-50 GHz)*
October 2003	WFR1YA3A.S2P	Antenna 3, wafer #1	TRL (30-40 GHz)
October 2003	WFR1YA3B.S2P	Antenna 3, wafer #1	TRL (30-40 GHz)**
October 2003	WFR1YA3BB.S2P	Antenna 3, wafer #1	TRL (40-50 GHz)
October 2003	WFR1YA3C.S2P	Antenna 3, wafer #1	TRL (40-50 GHz)*
October 2003	WFR1YA4A.S2P	Antenna 4, wafer #1	TRL (30-40 GHz)
October 2003	WFR1YA4B.S2P	Antenna 4, wafer #1	TRL (40-50 GHz)
October 2003	WFR1YA4C.S2P	Antenna 4, wafer #1	TRL (40-50 GHz)*
October 2003	WFR2YA1A.S2P	Antenna 1, wafer #2	TRL (30-40 GHz)
October 2003	WFR2YA1B.S2P	Antenna 1, wafer #2	TRL (40-50 GHz)
October 2003	WFR2YA2A.S2P	Antenna 2, wafer #2	TRL (30-40 GHz)
October 2003	WFR2YA2B.S2P	Antenna 2, wafer #2	TRL (40-50 GHz)
October 2003	WFR2YA3A.S2P	Antenna 3, wafer #2	TRL (30-40 GHz)
October 2003	WFR2YA3B.S2P	Antenna 3, wafer #2	TRL (40-50 GHz)
October 2003	WFR2YA4A.S2P	Antenna 4, wafer #2	TRL (30-40 GHz)
October 2003	WFR2YA4B.S2P	Antenna 4, wafer #2	TRL (40-50 GHz)
January 2004	WFR3YAG1.S2P	Antenna 1, wafer #3	TRL (40-50 GHz)
January 2004	WFR3YAG2.S2P	Antenna 2, wafer #3	TRL (40-50 GHz)
January 2004	WFR3YAG3.S2P	Antenna 3, wafer #3	TRL (40-50 GHz)
January 2004	WFR3YAG4.S2P	Antenna 4, wafer #3	TRL (40-50 GHz)

* Measurement realized with a second TRL calibration

** Data saved with the wrong filename

Appendix 7. Graphs of the S_{12} response of the two-ports circuits realized on the three different wafers

Appendix 7.1. The ring resonator

Only the measurement of the ring resonator circuits realized with TRL calibration are plotted in the following graphs in Figure 50. The results are summarized in Table 10 to Table 12. These tables also contain the LTCC material characteristics in terms of relative dielectric permittivity and attenuation constants. The values were obtained using equations (3) to (7).

Figure 50a: *First resonance*

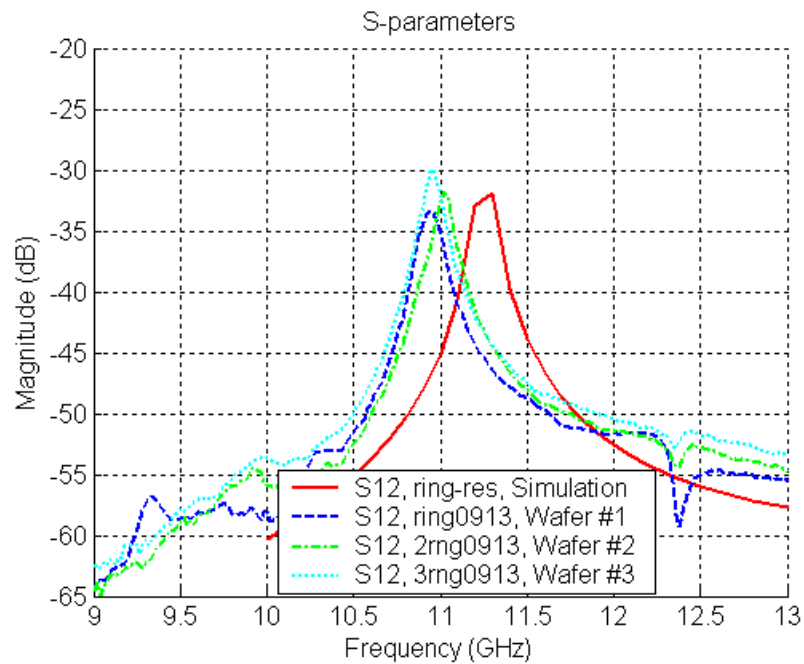


Figure 50b: *Second resonance*

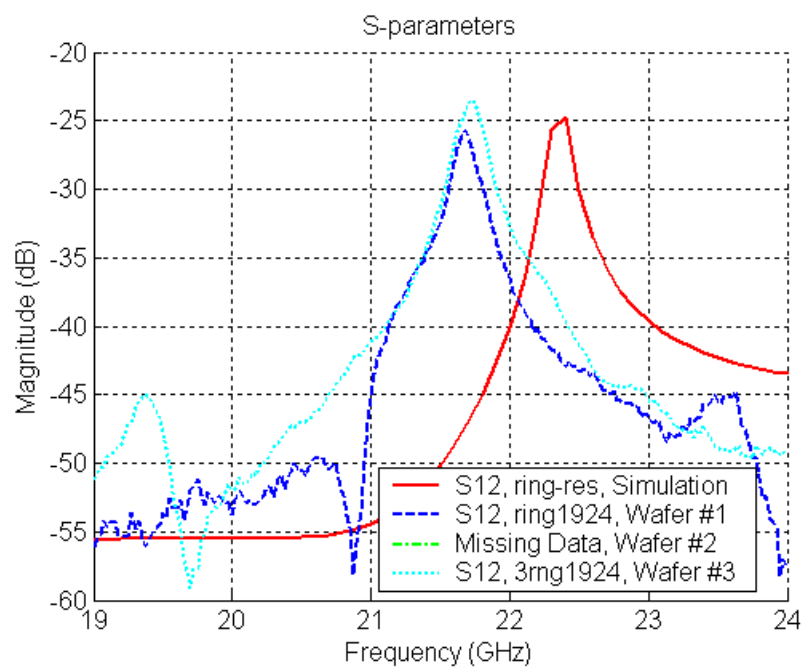


Figure 50c: *Third resonance*

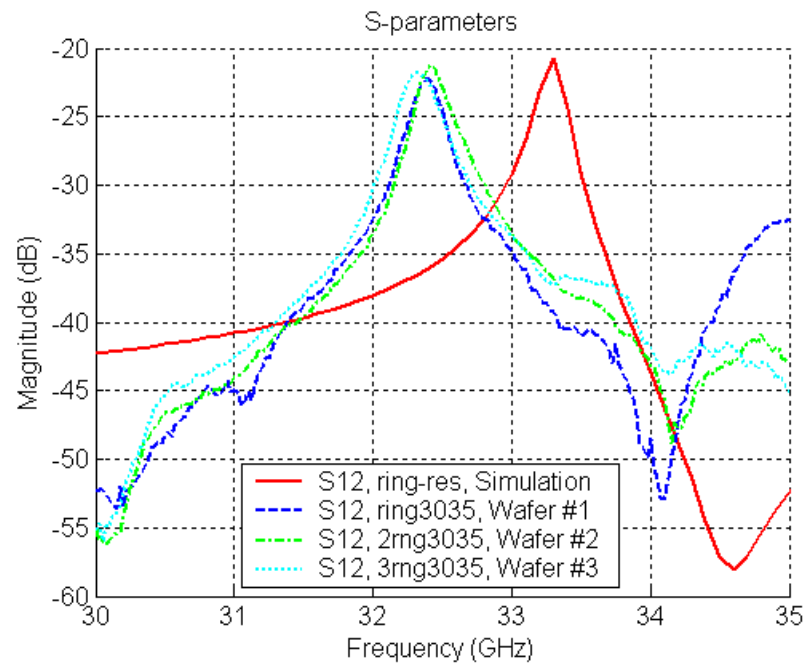


Figure 50d: *Fourth resonance*

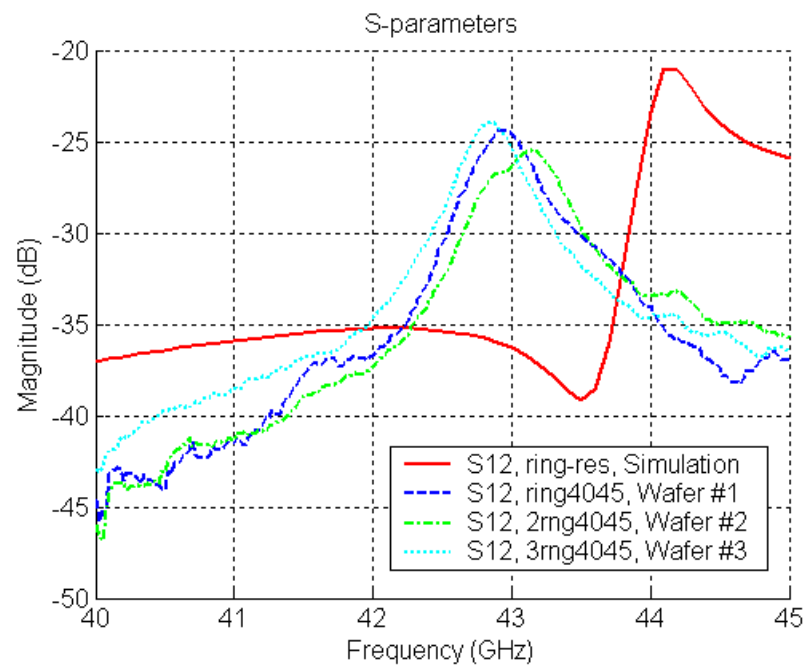


Figure 50. *Transmission Factor of the Ring Resonator Circuits*

Table 10. Measurement of the ring resonator on wafer # 1 with TRL calibration (October 2003)

Resonant Frequency (GHz)	10.94	21.7	32.4	42.95
Transmission Factor (dB)	-33.35	-25.75	-22.3	-24.45
3dB bandwidth (GHz)	10.865 / 11.015	21.585 / 21.77	32.225 / 32.515	42.665 / 43.21
	0.15	0.185	0.29	0.545
Effective permittivity	7.134	7.253	7.320	7.406
Loaded Quality Factor	72.933	117.297	111.724	78.807
Unloaded Quality Factor	74.536	123.677	121.010	83.830
Attenuation Factor (dB/m)	35.659	42.981	65.893	126.824

Table 11. Measurement of the ring resonator on wafer # 2 with TRL calibration (January 2004)

Resonant Frequency (GHz)	11.02	-/-	32.425	43.15
Transmission Factor (dB)	-31.8	-/-	-21.3	-24.45
3dB bandwidth (GHz)	10.97 / 11.07	-/-	32.30 / 32.55	42.74 / 43.415
	0.1	-/-	0.25	0.675
Effective permittivity	7.031	-/-	7.309	7.337
Loaded Quality Factor	110.200	-/-	129.700	63.926
Unloaded Quality Factor	113.107	-/-	141.919	68.000
Attenuation Factor (dB/m)	23.499	-/-	56.185	156.347

Table 12. Measurement of the ring resonator on wafer # 3 with TRL calibration (January 2004)

Resonant Frequency (GHz)	10.96	21.725	32.325	42.85
Transmission Factor (dB)	-30	-23.5	-21.8	-24
3dB bandwidth (GHz)	10.895 / 11.01	21.605 / 21.82	32.175 / 32.49	42.6 / 43.1
	0.115	0.215	0.315	0.5
Effective permittivity	7.108	7.236	7.354	7.440
Loaded Quality Factor	95.304	101.047	102.619	85.700
Unloaded Quality Factor	98.417	108.284	111.698	91.471
Attenuation Factor (dB/m)	27.007	49.091	71.386	116.228

Appendix 7.2. The 3-wavelength-long microstrip line loaded with a 3/4-wavelength-long open stub

Figure 51a: *Reflection coefficient around the second resonance*

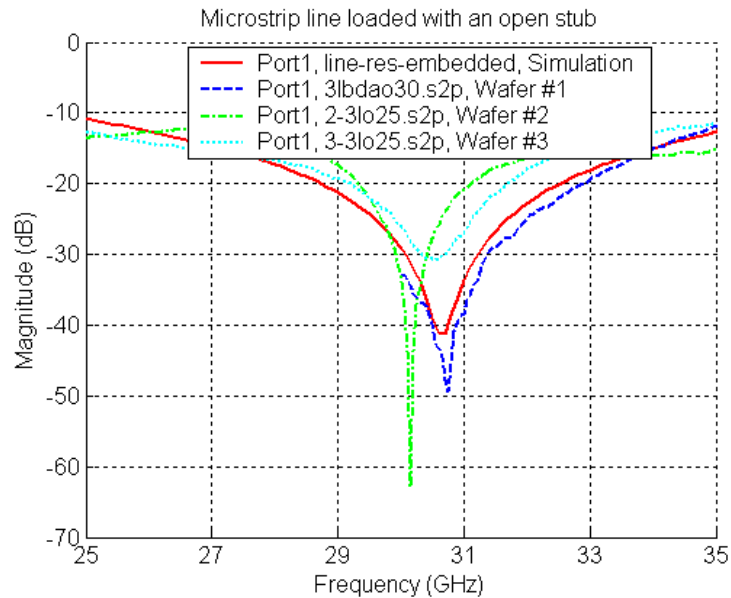


Figure 51b: *Transmission factor around the first resonance*

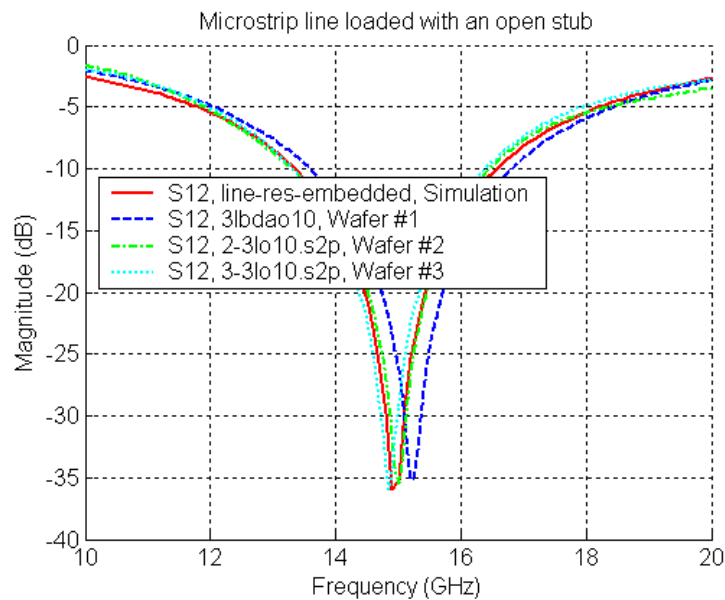


Figure 51c: *Transmission factor around the third resonance*

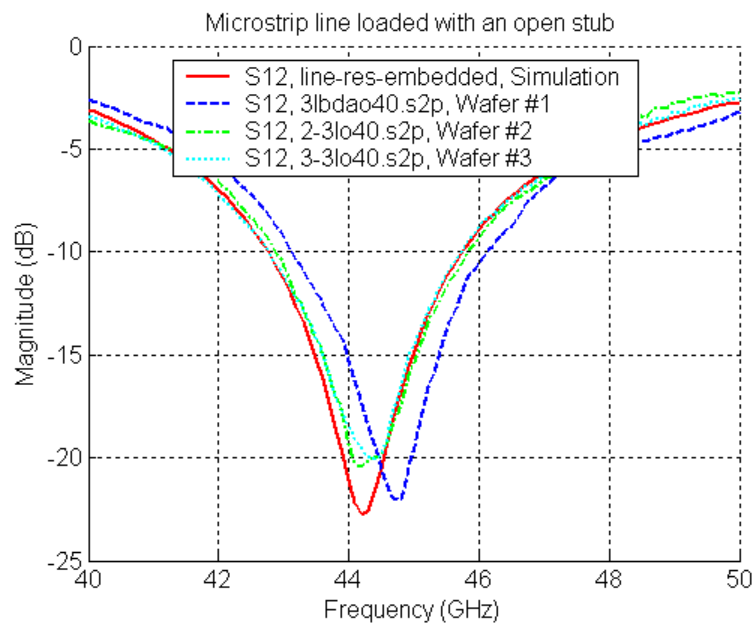


Figure 51. *S-parameters of the three wavelength microstrip line loaded with a three-quarter of wavelength open stub*

Table 13. Measurement of the “T-junction” circuit on wafer #1 (October 2003)

		Port 1	Port 2	
Resonant Frequency (GHz)	15.22	30.75	30.8	44.75
Reflection coefficient (dB)	-0.45	-49.5	-33	-1.3
Transmission Factor (dB)	-36	-0.56	-0.57	-22.05
3dB bandwidth (GHz)	15.15 / 15.30			44.365 / 45.03
	0.15			0.665
Effective permittivity	6.673	6.539	6.518	6.947
Loaded Quality Factor	101.467			67.293
Unloaded Quality Factor	103.101			73.064
Attenuation Factor (dB/m)	25.780			109.134

Table 14. Measurement of the “T-junction” circuit on wafer #2 (January 2004)

		Port 1	Port 2	
Resonant Frequency (GHz)	15	30.15	30.15	44.2
Reflection coefficient (dB)	-0.43	-63.00	-29.50	-1.60
Transmission Factor (dB)	-35.55			-20.4
3dB bandwidth (GHz)	14.92 / 15.08			43.85 / 44.79
	0.16			0.94
Effective permittivity	6.870	6.802	6.802	7.121
Loaded Quality Factor	93.750			47.021
Unloaded Quality Factor	95.341			51.986
Attenuation Factor (dB/m)	27.878			153.382

Table 15. Measurement of the “T-junction” circuit on wafer #1 (October 2003)

		Port 1	Port 2	
Resonant Frequency (GHz)	14.85	30.55	30.45	44.4
Reflection coefficient (dB)	-0.39	-30.7	-24.85	-1.5
Transmission Factor (dB)	-36			-20.1
3dB bandwidth (GHz)	14.78 / 14.93			43.80 / 44.75
	0.15			0.95
Effective permittivity	7.010	6.625	6.669	7.057
Loaded Quality Factor	99.000			46.737
Unloaded Quality Factor	100.594			51.864
Attenuation Factor (dB/m)	26.422			153.743

Appendix 8. Loss characterisation using transmission line measurement

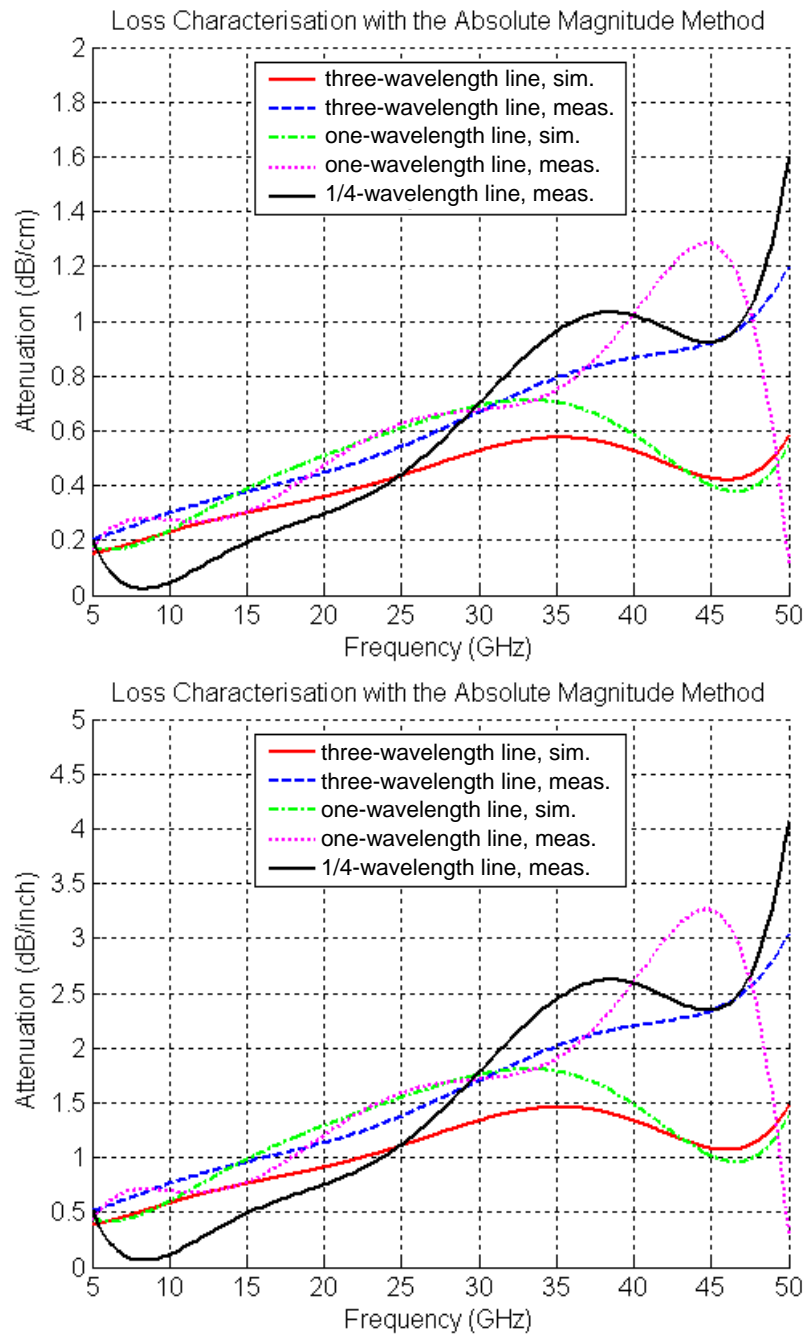


Figure 52. Attenuation factor estimated using the absolute magnitude method, in dB/cm and dB/inch

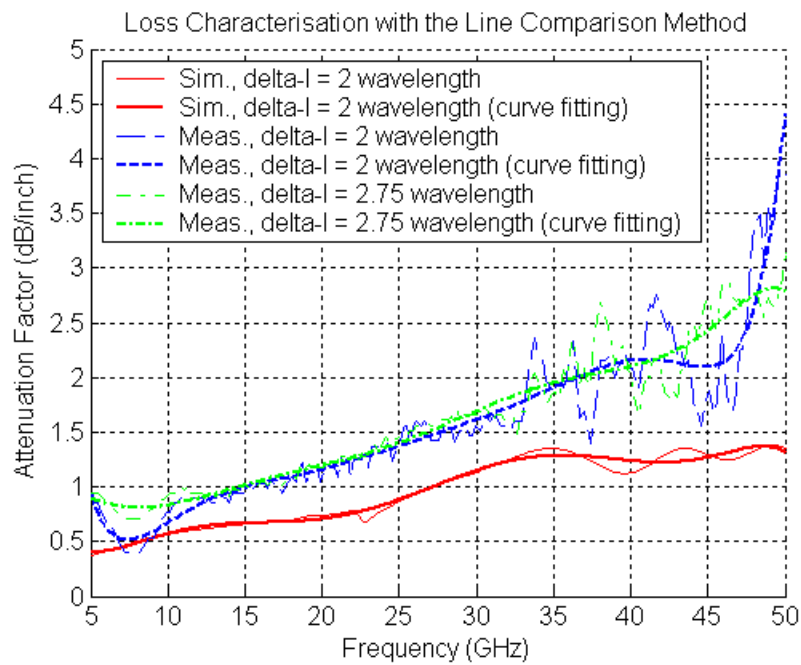
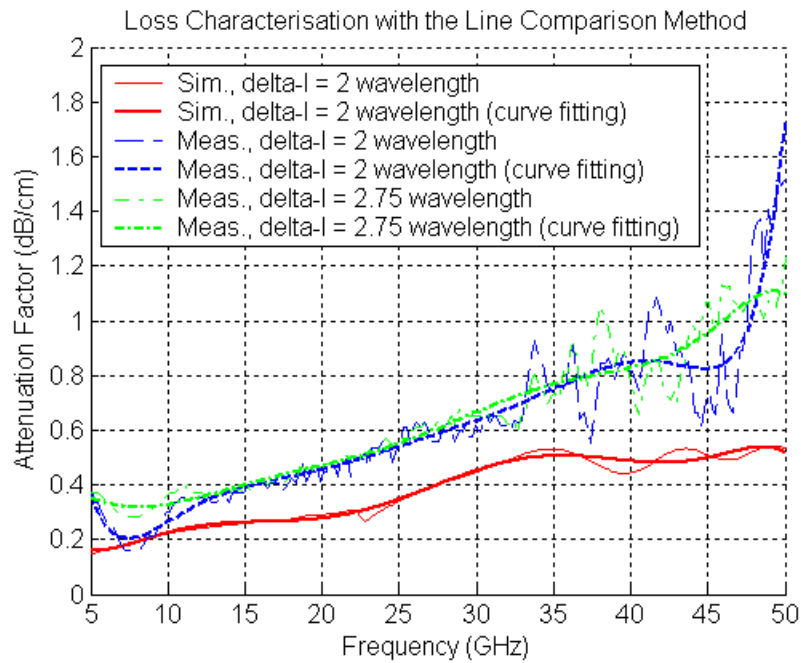


Figure 53. Attenuation factor estimated using the line comparison method, in dB/cm and dB/inch

Appendix 9. Input impedance of the Yagi-like antennas

Appendix 9.1. Characteristics of the different antennas

The following tables summarize the antenna characteristics in terms of resonant frequency and bandwidth. They are based on the measurement shown in Figure 39, Figure 55, Figure 57 and Figure 58. The results obtained by simulation are also reported. They are based on the antenna responses given in Figure 41.

Table 16. Characteristics of antenna #1 obtained from measurement and simulation

Filename	Date of Measurement	Calibration Number	Minimum Reflection coefficient (RC) (dB)	Frequency at min. RC (GHz)	"-10 dB RC" Bandwidth (GHz)	
					Fmin	Fmax
WFR1ANT1	June-03	1	-10.4	45.05	44.9	45.6
WFR1YA1B	October-03	2	-8.6	46.4	Null	Null
WFR1YA1C	October-03	3	-8.7	45.1	Null	Null
WFR2ANT1	June-03	1	-11.35	45.5	44.95	45.8
WFR2YA1B	October-03	2	-10.35	45.65	45.5	46
WFR3YAG1	January-04	4	-10.5	45	44.7	45.2
Simulation			-16.9	45.8	37.3	47.1

Table 17. Characteristics of antenna #2 obtained from measurement and simulation

Filename	Date of Measurement	Calibration Number	Minimum Reflection coefficient (RC) (dB)	Frequency at min. RC (GHz)	"-10 dB RC" Bandwidth (GHz)	
					Fmin	Fmax
WFR1ANT2	June-03	1	-23.3	44.25	43.85	46.35
WFR1YA2B	October-03	2	-14	44.55	43.8	46.4
WFR1YA2C	October-03	3	-15.45	44.5	43.75	46.5
WFR2ANT2	June-03	1	-15.9	45.5	44.5	46.3
WFR2YA2B	October-03	2	-15.5	45.55	44.7	46.95
WFR3YAG2	January-04	4	-13.3	45.2	44.45	45.9
Simulation			-28.6	45.8	35.8	46.95

Table 18. Characteristics of antenna #3 obtained from measurement and simulation

Filename	Date of Measurement	Calibration Number	Minimum Reflection coefficient (RC) (dB)	Frequency at min. RC (GHz)	"-10 dB RC" Bandwidth (GHz)	
					Fmin	Fmax
WFR1ANT3	June-03	1	-37.5	44.8	43.6	46.35
WFR1YA3B	October-03	2	-23.1	45.2	43.75	46.4
WFR1YA3C	October-03	3	-27.5	45.25	43.6	46.5
WFR2ANT3	June-03	1	-22.3	45.05	44.2	46.4
WFR2YA3B	October-03	2	-18.1	45.8	44.3	47.7
WFR3YAG3	January-04	4	-13.3	44.85	43.9	46
Simulation			-25.1	45.9	44.2	46.85

Table 19. Characteristics of antenna #4 obtained from measurement and simulation

Filename	Date of Measurement	Calibration Number	Minimum Reflection coefficient (RC) (dB)	Frequency at min. RC (GHz)	"-10 dB RC" Bandwidth (GHz)	
					Fmin	Fmax
WFR1ANT3	June-03	1	-29.3	45.05	43.7	46.6
WFR1YA3B	October-03	2	-17.9	45.25	43.8	46.9
WFR1YA3C	October-03	3	-22.6	45.25	43.65	47
WFR2ANT3	June-03	1	-25.4	45.05	43.8	47.7
WFR2YA3B	October-03	2	-17.9	45.85	43.5	48.4
WFR3YAG3	January-04	4	-16.9	45.55	43.45	47.55
Simulation			-17.8	45.75	44.5	46.6

Appendix 9.2. Input impedance responses of the Yagi-like antennas

Several graphs of the input impedance responses of the four Yagi-like antennas are presented in this sub-appendix. First, the responses of each antenna design realized on different wafers and measured after different calibrations are shown. The second set of graphs show the responses of the four antennas realized on the same wafer, and measured after the same calibration.

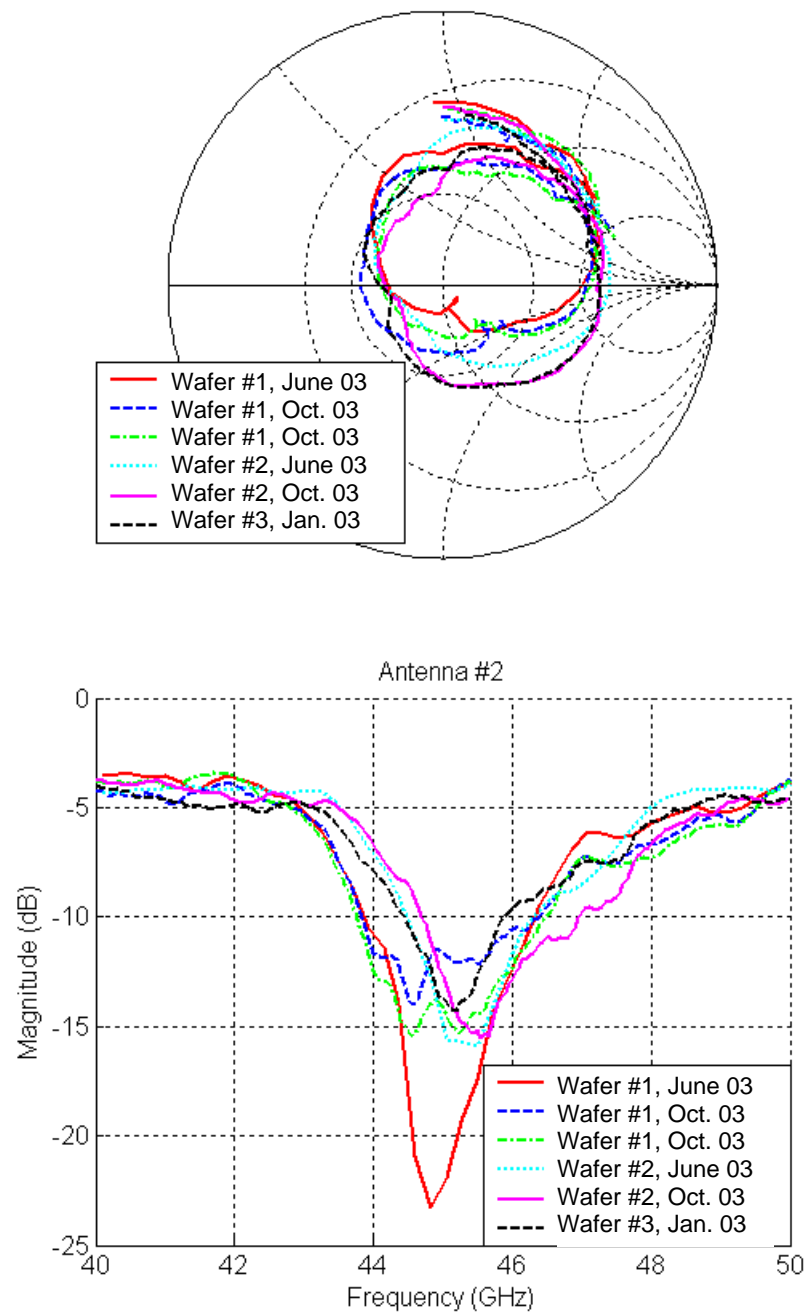


Figure 54. Input impedance of antenna #2 on all wafers measured with different TRL calibrations

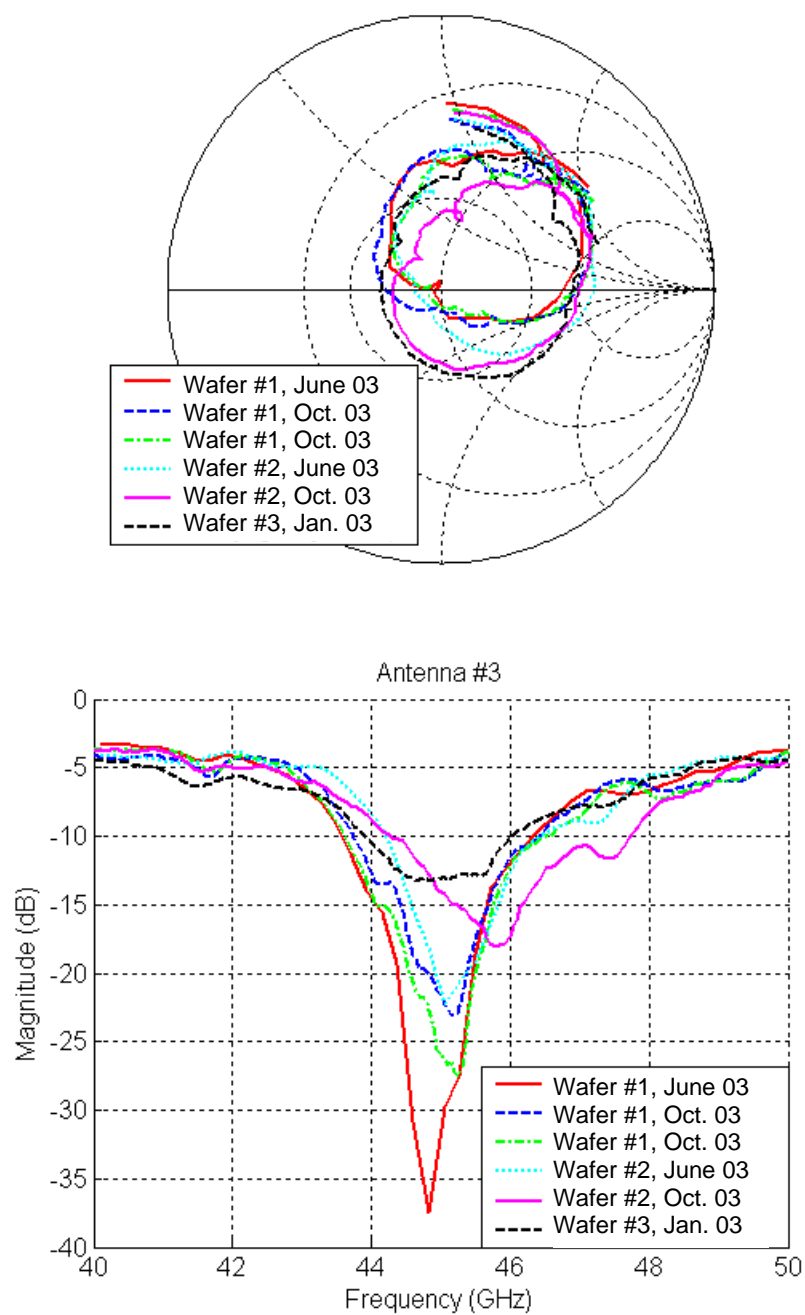


Figure 55. Input impedance of antenna #3 measured on all wafers with different TRL calibrations

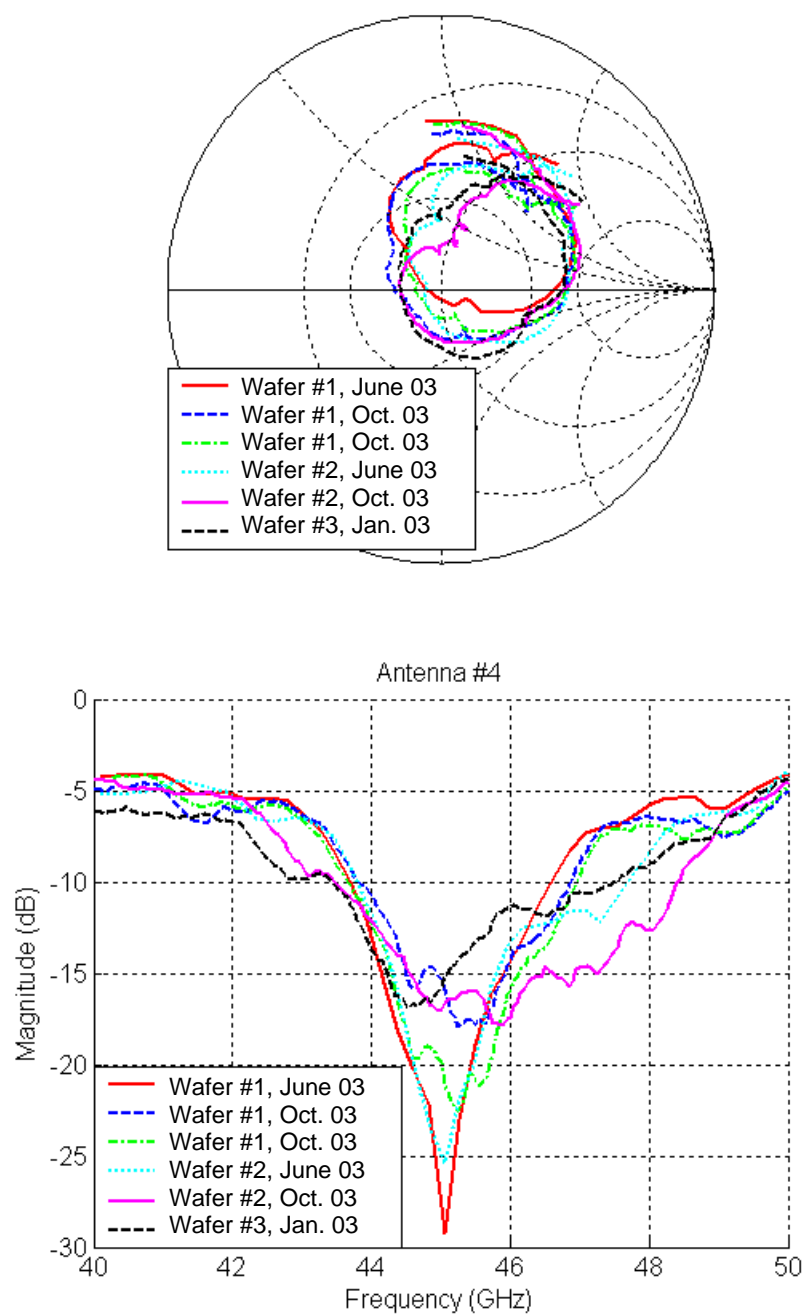


Figure 56. Input impedance of antenna #4 on all wafers measured with different TRL calibrations

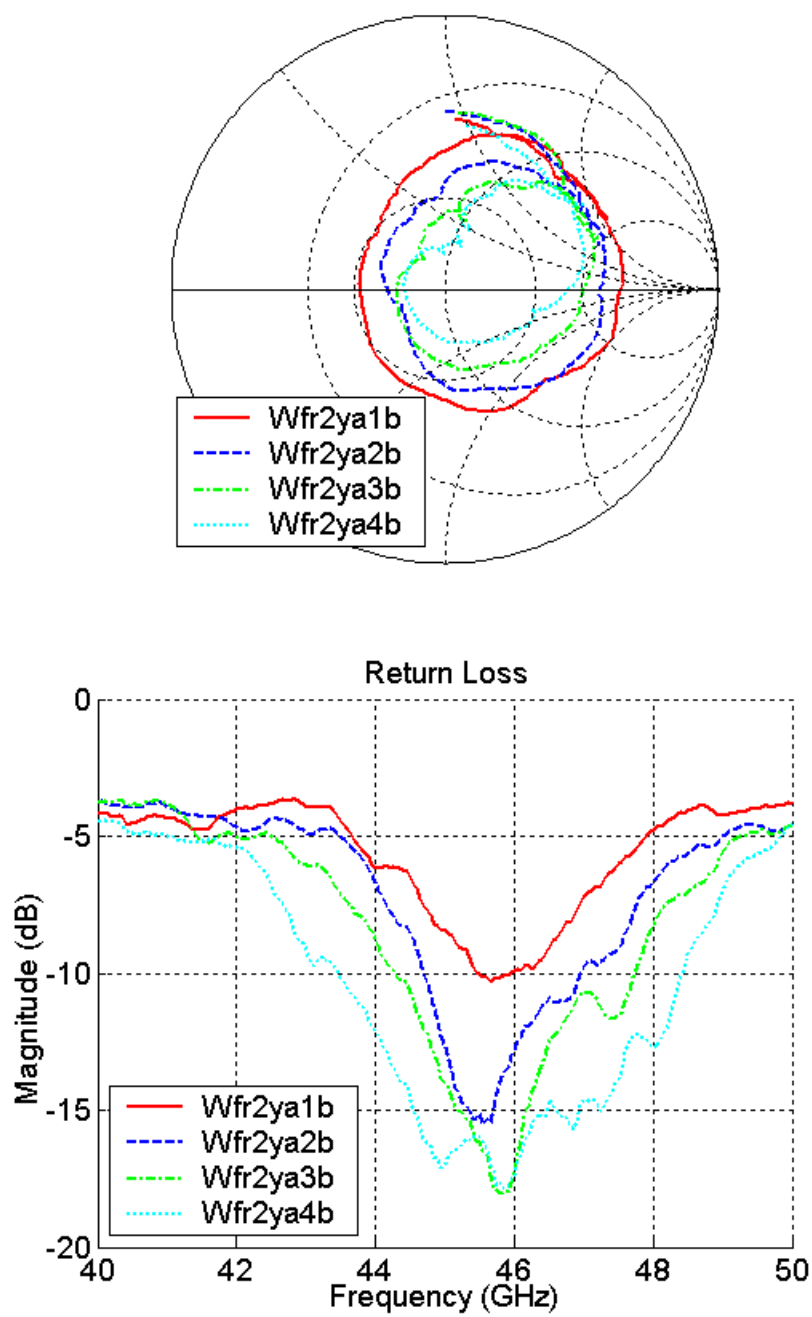


Figure 57. Input impedance of all antennas measured on wafer #2 in October 2003

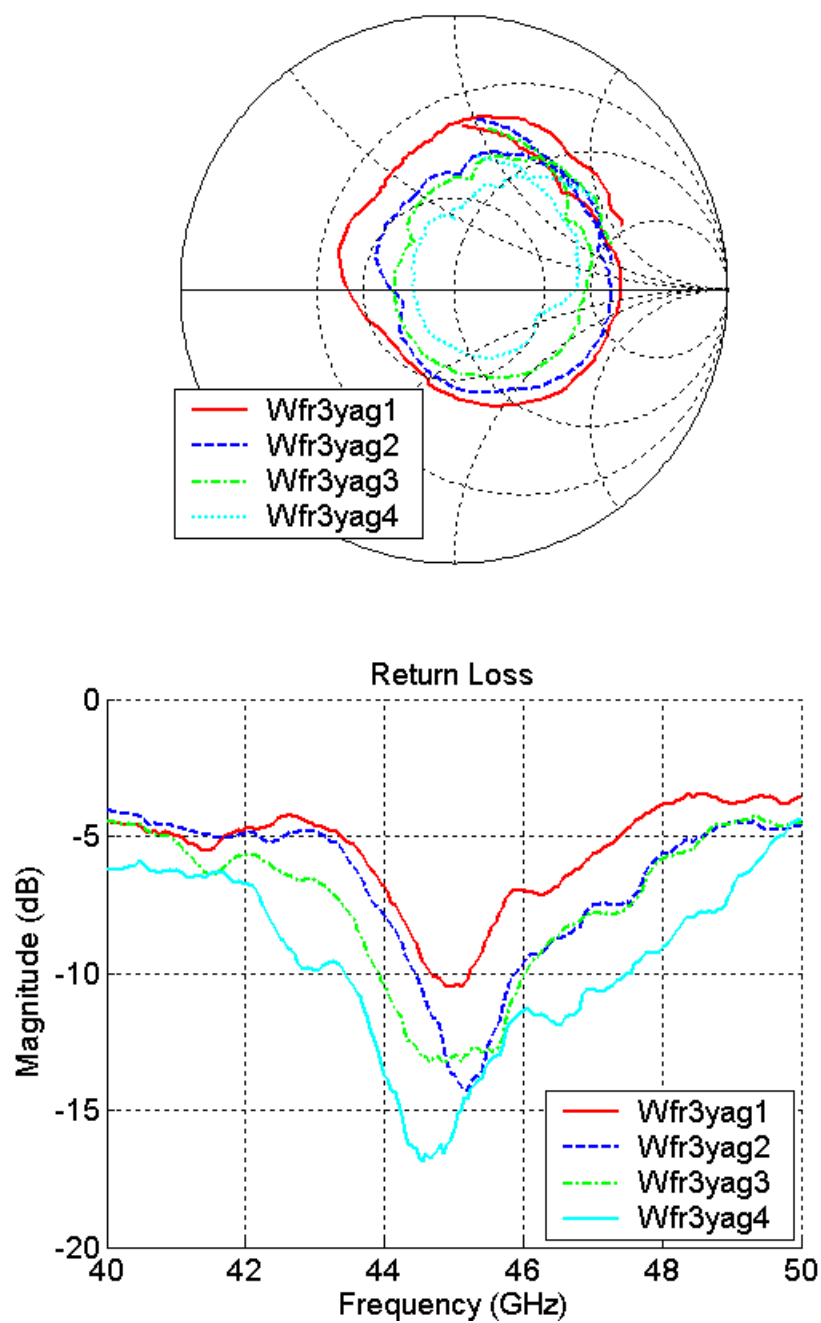


Figure 58. Input impedance of all antennas measured on wafer #3 in January 2004

List of symbols/abbreviations/acronyms/initialisms

AEHF	Advanced Extremely High Frequency
DND	Department of National Defence
DRDC Ottawa	Defence Research & Development Canada - Ottawa
EHF	Extremely High Frequency

Glossary

Technical term	Explanation of term
BGA	Ball Grid Array
BW	Bandwidth
CPS	Coplanar Strip
CPW	Coplanar Waveguide
LTCC	Low Temperature Co-fired Ceramic
MMIC	Monolithic Microwave Integrated Circuit
Np	Neper unit, $1Np = 20 \cdot \text{Log}(e) = 8.686 \text{ dB}$
OSL	Open-Short-Load (calibration method)
RC	Reflexion Coefficient
SC	Smith Chart
TRL	Thru-Reflect-Line (calibration method)
VNA	Vector Network Analyser
VSWR	Voltage Standing Wave Ratio
VTT	Valtion Teknillinen Tutkimuskeskus

This page is intentionally left blank

UNCLASSIFIED

SECURITY CLASSIFICATION OF FORM
(highest classification of Title, Abstract, Keywords)

DOCUMENT CONTROL DATA

(Security classification of title, body of abstract and indexing annotation must be entered when the overall document is classified)

1. ORIGINATOR (the name and address of the organization preparing the document. Organizations for whom the document was prepared, e.g. Establishment sponsoring a contractor's report, or tasking agency, are entered in section 8.) Defence R&D Canada – Ottawa Ottawa, On, K1A 0Z4		2. SECURITY CLASSIFICATION (overall security classification of the document, including special warning terms if applicable) UNCLASSIFIED	
3. TITLE (the complete document title as indicated on the title page. Its classification should be indicated by the appropriate abbreviation (S,C or U) in parentheses after the title.) DESIGN AND ANALYSIS OF A YAGI-LIKE ANTENNA ELEMENT BURIED IN LTCC MATERIAL FOR AEHF COMMUNICATION SYSTEMS (U)			
4. AUTHORS (Last name, first name, middle initial) Clénet, Michel			
5. DATE OF PUBLICATION (month and year of publication of document) April 2005		6a. NO. OF PAGES (total containing information. Include Annexes, Appendices, etc.) 85	
		6b. NO. OF REFS (total cited in document) 35	
7. DESCRIPTIVE NOTES (the category of the document, e.g. technical report, technical note or memorandum. If appropriate, enter the type of report, e.g. interim, progress, summary, annual or final. Give the inclusive dates when a specific reporting period is covered.) Technical Memorandum			
8. SPONSORING ACTIVITY (the name of the department project office or laboratory sponsoring the research and development. Include the address.)			
9a. PROJECT OR GRANT NO. (if appropriate, the applicable research and development project or grant number under which the document was written. Please specify whether project or grant) 15ck18		9b. CONTRACT NO. (if appropriate, the applicable number under which the document was written)	
10a. ORIGINATOR'S DOCUMENT NUMBER (the official document number by which the document is identified by the originating activity. This number must be unique to this document.) DRDC Ottawa TM 2005-055		10b. OTHER DOCUMENT NOS. (Any other numbers which may be assigned this document either by the originator or by the sponsor)	
11. DOCUMENT AVAILABILITY (any limitations on further dissemination of the document, other than those imposed by security classification) <input checked="" type="checkbox"/> (X) Unlimited distribution <input type="checkbox"/> () Distribution limited to defence departments and defence contractors; further distribution only as approved <input type="checkbox"/> () Distribution limited to defence departments and Canadian defence contractors; further distribution only as approved <input type="checkbox"/> () Distribution limited to government departments and agencies; further distribution only as approved <input type="checkbox"/> () Distribution limited to defence departments; further distribution only as approved <input type="checkbox"/> () Other (please specify):			
12. DOCUMENT ANNOUNCEMENT (any limitation to the bibliographic announcement of this document. This will normally correspond to the Document Availability (11). However, where further distribution (beyond the audience specified in 11) is possible, a wider announcement audience may be selected.)			

UNCLASSIFIED

SECURITY CLASSIFICATION OF FORM

DCD03 2/06/87

13. ABSTRACT (a brief and factual summary of the document. It may also appear elsewhere in the body of the document itself. It is highly desirable that the abstract of classified documents be unclassified. Each paragraph of the abstract shall begin with an indication of the security classification of the information in the paragraph (unless the document itself is unclassified) represented as (S), (C), or (U). It is not necessary to include here abstracts in both official languages unless the text is bilingual).

This document presents the investigation of an end-fire antenna implemented in a laminated material named LTCC (Low Temperature Co-fired Ceramic). This study is related to the development of a phased array for the AEHF Military Satellite Communication Systems. This work includes the design, the analysis, fabrication and the measurement of antenna prototypes at 44.5 GHz. The radiating element consists of a Yagi-like antenna fed by a microstrip transmission line and buried into the dielectric material. Relatively good agreement between simulated results and measurement is obtained. The results shows that this radiating element could be used for AEHF Communication systems. The next step is to study its electromagnetic behaviour in an array configuration. As the LTCC material has not previously been characterized up to 45 GHz, a study to extract the electrical properties of the LTCC material has been carried out, and is also reported in this document.

14. KEYWORDS, DESCRIPTORS or IDENTIFIERS (technically meaningful terms or short phrases that characterize a document and could be helpful in cataloguing the document. They should be selected so that no security classification is required. Identifiers such as equipment model designation, trade name, military project code name, geographic location may also be included. If possible keywords should be selected from a published thesaurus. e.g. Thesaurus of Engineering and Scientific Terms (TEST) and that thesaurus-identified. If it is not possible to select indexing terms which are Unclassified, the classification of each should be indicated as with the title.)

Yagi-like Antenna
LTCC Technology
Ring Resonator
Material Measurement

Defence R&D Canada

Canada's leader in Defence
and National Security
Science and Technology

R & D pour la défense Canada

Chef de file au Canada en matière
de science et de technologie pour
la défense et la sécurité nationale



www.drdc-rddc.gc.ca